

Alma Mater Studiorum
University of Bologna

Dissertation for the degree of
DOCTOR OF PHILOSOPHY IN PHYSICS

SC: 02/B1; SSD: FIS/03

**SCALED DOWN
PHYSICAL PROPERTIES
OF SEMICONDUCTOR NANOWIRES FOR
NANO-ELECTRONICS SCALING UP**

Thesis Advisor:

Prof. Anna Cavallini

Presented By:

Stefania Carapezzi

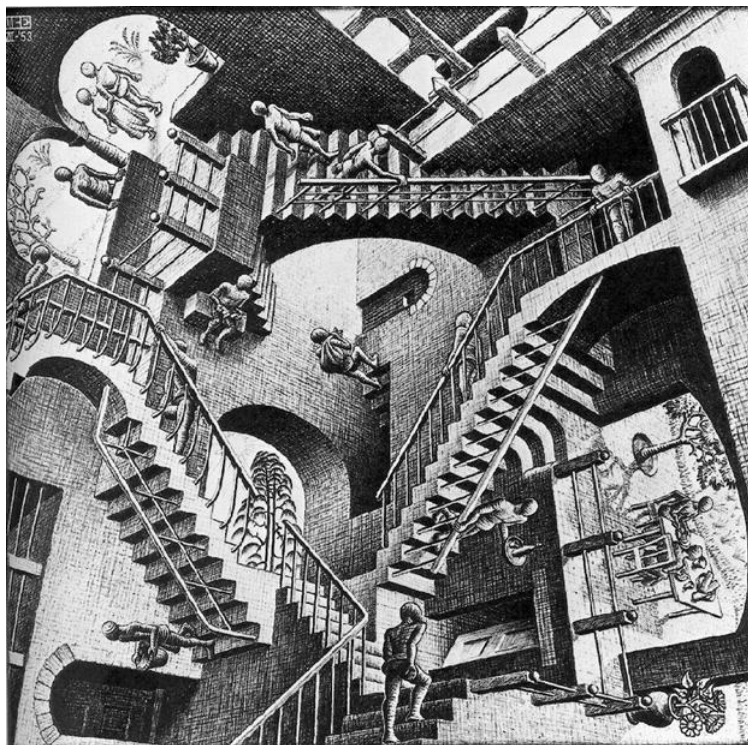
PhD Coordinator:

Prof. Fabio Ortolani

XXVI CYCLE – MARCH 2014

There are more things in heaven and earth, Horatio,
Than are dreamt of in your philosophy.

William Shakespeare, "Hamlet", Act 1 scene



After Relativity (M. C. Escher)

ABSTRACT

Semiconductor nanowires (NWs) are one- or quasi one-dimensional systems whose physical properties are unique as compared to bulk materials because of their nanoscaled sizes. They bring together quantum world and semiconductor devices. NWs-based technologies may achieve an impact comparable to that of current microelectronic devices if new challenges will be faced. This thesis primarily focuses on two different, cutting-edge aspects of research over semiconductor NW arrays as pivotal components of NW-based devices.

The first part deals with the characterization of electrically active defects in NWs. It has been elaborated the set-up of a general procedure which enables to employ Deep Level Transient Spectroscopy (DLTS) to probe NW arrays' defects. This procedure has been applied to perform the characterization of a specific system, i.e. Reactive Ion Etched (RIE) silicon NW arrays-based Schottky barrier diodes. This study has allowed to shed light over how and if growth conditions introduce defects in RIE processed silicon NWs.

The second part of this thesis concerns the bowing induced by electron beam and the subsequent clustering of gallium arsenide NWs. After a justified rejection of the mechanisms previously reported in literature, an original interpretation of the electron beam induced bending has been illustrated. Moreover, this thesis has successfully interpreted the formation of NW clusters in the framework of the lateral collapse of fibrillar structures. These latter are both idealized models and actual artificial structures used to study and to mimic the adhesion properties of natural surfaces in lizards and insects (Gecko effect). Our conclusion are that mechanical and surface properties of the NWs, together with the geometry of the NW arrays, play a key role in their post-growth alignment. The same parameters open, then, to the benign possibility of locally engineering NW arrays in micro- and macro-templates.

TABLE OF CONTENTS

ABSTRACT.....	ii
TABLE OF CONTENTS.....	iii
CHAPTER 1 – Semiconductor Nanowires: Assets and Challenges in Nanotechnology.....	1
1.1 Semiconductor Nanowires: Weaving Together Nanophysics and Nanoelectronics	1
1.2 Si Grass-Based Schottky-Barrier Diodes.....	2
1.2.1 Top-Down Fabricated Silicon NW Arrays: the Si Grass Case.....	2
1.2.2 Schottky Contacts Over NW arrays	3
1.2.3 Defect Characterization of NW Array-Based SBDS.....	3
1.3 Misalignment and Bundles Formation of Gallium Arsenide NWs	7
A Preliminary Lexicon Note to the Interested Reader.....	7
1.3.1 Pre-Growth and During Growth Engineering of Vertical Orientation in NWs.....	7
1.3.2 Vertical Aligned Gallium Arsenide NWs in Nanophotonics.....	9
1.3.3 Post-Growth Vertical Misalignment: Bending of NWs Under an Electron Beam	10
1.3.4 Lateral Collapse and Bundling in Semiconductor NWs.....	10
1.3.5 Self-Assembly of NWs: a Way to NWs Patterning	10
1.4 Objectives and Structure of This Thesis	13
BIBLIOGRAPHY.....	15
PART I – ELECTRICAL AND DEFECT LEVEL CHARACTERIZATION OF SI GRASS-BASED SBDS	20

CHAPTER 2 – Si Grass Growth and Si Grass-Based SBDs Fabrication.	21
2.1 Reactive Ion Etching (RIE) and the Bosch Process	21
2.1.1 Inductively Coupled Plasma Reactive Ion Etching (ICP RIE)	21
Plasma Generation for RIE.....	21
Plasma Etching Mechanism.....	23
Etch Chemistry of silicon	24
2.1.2 Bosch Process and Si Grass Growth	25
Etching Profiles.....	25
Bosch Process	26
Si Grass as a Self-Organized Nanostructure	28
2.1.3 Si Grass Samples	29
2.2 Si Grass-Based SBDs: the Fabrication Process	31
2.2.1 NW Array Encapsulation into a Filler Material.....	31
SU8 Photoresist as Filler for Si Grass-Based SBDs	32
Si Grass NWs Encapsulation: Procedure Recipe	33
2.2.2 Contact Deposition Over the Encapsulated NW Array	35
BIBLIOGRAPHY.....	36
CHAPTER 3 – Current Transport in Si Grass-Based SBDs.....	38
3. 1 The Schottky Barrier Formation	38
3.1.1 The Work Function of a Solid	38
3.1.2 Ideal Schottky Barrier: the Schottky-Mott Theory	38
Forward and Reverse Bias	41
3.1.3 Real Schottky Barriers	41
3.2 Current Transport in Schottky Junctions.....	42
3.2.1 Thermionic Emission Model	42
Image Force Lowering of the Barrier	43

Effect of the Image Force Lowering of the Barrier Over the Thermionic Emission Model	46
Ideality Factor	47
3.2.2 Tunneling Current.....	47
3.2.3 The Richardson Plot of the Saturation Current.....	47
3.3 Si Grass-Based SBDs: the Electrical Characterization.....	48
3.3.1 Review of Results of Current Transport Models in NW-Based SBDs.....	50
Nano-Schottky Junctions.....	50
Single Semiconductor NW-based SBDs	50
Array NW-Based SBDs	50
3.3.2 Alternative Current Transport Models for SBDs	51
The Parasitic Effects	52
Space Charge Limited Current (SCLC) Transport	53
Poole–Frenkel Current Transport.....	54
3.3.3 Si Grass-Based SBDs I-Vs: Identification of the Current Transport Mechanism in the High Bias $V \geq 2$ Region	54
Comparing Current Transport Models by Akaike’s Information Criterion	56
BIBLIOGRAPHY	58
CHAPTER 4 – Defect Level Characterization of Si Grass-based SBDs	60
4.1 Deep Levels and Their Electrical Characterization.....	60
4.1.1 Deep States.....	60
Transient Response	62
The Trap Signature	63
Electron Trap and Hole Trap.....	65
Majority and Minority Carrier Traps	65
4.1.2 Basis of Transient Depletion Experiment for a Majority Carrier Trap.....	67
4.1.3 Deep Level Transient Spectroscopy (DLTS)	69

C-DLTS: Principle of Operation	70
The Two-Point Subtraction Rate Window Principle	71
4.2 Damages Induced by the RIE Mechanism	73
4.2.1 Survey on the RIE Damage	74
Energetic Particle flux.....	74
Beam-Solid Interaction Processes	74
Surface Residues	75
Heavy Metal Contamination	75
4.3 DLTS Characterization of Si Grass-Based SBDs	75
4.3.1 Challenges of DLTS Characterization of Semiconductor NWs	75
4.3.2 C- DLTS Measurements of Si Grass-Based SBDs.....	76
C- DLTS Measurements of Samples from Set I	78
C- DLTS Measurements of Samples from Set II	79
C- DLTS Measurements of Samples from Set III	80
Preliminary Discussion on the DLTS Results and Future Work Plan	81
BIBLIOGRAPHY	83

PART II - ELECTRON BEAM INDUCED BENDING AND ADHESION DRIVEN BUNDLING FOR NANOSCALED PATTERNING 84

CHAPTER 5 – Electron Beam Induced Bending of MBE Au-Catalyzed Wurtzite GaAs NWS	85
5.1 The Vapor-Solid-Liquid (VLS) Mechanism and Molecular Beam Epitaxy Method for NWs Growing.....	85
5.1.1 The VLS Mechanism	85
5.1.2 NW Growth by MBE	86
5.1.3 Au-Catalyzed WZ GaAs NWs: Details of the Samples Growth	87
5.2 Electron Beam Induced GaAs NWs Bending: Experimental Observations	88
5.3 Review of Models for Semiconductor NWs Bending.....	90

5.3.1 Self-Attraction Among Aligned Au/ZnO Nanorods Under Electron Beam.....	90
5.3.2 Bending and Bundling of Metal-Free Vertically Aligned ZnO NWs Due to Electrostatic Interaction	93
5.3.3 Tailoring the VLS Growth Toward the Self-Assembly of GaAs NW Junctions.....	96
5.4 Mechanism of Nanostructure Movement Under an Electron Beam.....	98
5.4.1 Experimental Observations	98
5.4.2 Theoretical Model for Electron Charge Implantation	100
5.4.3 Theoretical Model for Electrostatically Driven Bending	102
5.5 Proposed Mechanism Inducing GaAs NWs Bending	105
BIBLIOGRAPHY	107
CHAPTER 5 – MBE Au-Catalyzed Wurtzite GaAs NWs Bundling as a Case of Adhesion-Driven Lateral Collapse	109
6.1 Physics and Mechanics of Contact and Adhesion of Fibrillar Interfaces ..	109
6.1.1 The Gecko Effect.....	109
6.1.2 Adhesion of Bio-Mimicked and Bio-Inspired Artificial Single-Level Fibrillar Structures: Some Theoretical Considerations.....	110
Lateral Collapse of Adjacent Plate-Like Fibrils.....	113
6.2 Lateral Collapse of Nanowires.....	118
6.2.1 Estimation of parameter $2w$ for Randomly Located NWs.....	118
Extraction of 2-Dimensional Coordinate Systems Maps of the Spatial Location of NWs in the Arrays from SEM Images.....	118
Statistical Analysis of Spatial Point Patterns	119
6.2.2 Theoretical Calculation of Surface Energy of III-V NWs	122
6.2.3 Adhesion-Driven GaAs NW Bundles.....	124
BIBLIOGRAPHY	127
CHAPTER 7 – Conclusions and Future Directions	129

7.1 Si Grass SBDs	129
7.2 Electron Beam Mediated Bending and Bundling of GaAs NWs	129
LIST OF TABLES.....	132
LIST OF FIGURES	133
APPENDICES	
Appendix A – Block Diagram of DLTS Set-Up.....	143
LIST OF PUBLICATIONS.....	144

CHAPTER 1

Semiconductor Nanowires: Assets and Challenges in Nanotechnology

1.1 Semiconductor Nanowires: Weaving Together Nanophysics and Nanoelectronics

Semiconductor nanowires (NWs) are widely investigated one- or quasi one-dimensional systems. They share with other nanostructures physical properties that are unique as compared to bulk materials, because of their nanoscaled sizes. Moreover, the synthesis and fabrication of NW-based devices present new industrial-appealing opportunities with respect to the traditional wafer-based technologies. For instance, they allow to save materials or use cheaper substrates. Furthermore, they are the most probable candidates to offer continuance to the Moore's Law in the future [1.1]. Their size both provides a way to downscale the Integrated Circuits (ICs) and to overcome the approaching physical limit of the lithography technique. Their double nature of interconnection and active devices opens to new possibilities for the clever realization of ICs with a higher (3D) degree of integration. Technological applications of these 1D nanostructures range in every field of nanoelectronics: electronic devices [1.2], logical gates [1.3], nonvolatile memories [1.4], photovoltaics [1.5], photonics [1.6], and biological sensors [1.7].

The next delicate step is the coming out from the proof-of-concept, laboratory realizations in order to bridge the Nano achievements with the existent Micro technologies. The history of the semiconductor industry points to us that only those technologies that can be integrated and scaled up for large hierarchical systems will survive and finally have impact. To the end of reaching the full marketability the Nano-Micro-integration is thus mandatory. Among the many roads explored towards the realization of real-world nanoelectronic devices, the semiconductor NW arrays enter into nanodevices architectures as a promising way to scalable fabrication and

sizable quantities, as well as a smooth solution to the NWs integration related issues. This implies that a new set of fundamental and technical challenges have to be coped with.

1.2 Si Grass-Based Schottky-Barrier Diodes

1.2.1 Top-Down Fabricated Silicon NW Arrays: the Si Grass Case

The roughening of silicon surfaces generated by the Reactive Ion Etching (RIE) process, known as silicon (Si) Grass or Black Silicon, represents an alternative, cost-efficient way to fabricate nano-structured Si surfaces. Generally speaking it consists of an array of needle-like features decorating RIE processed Si substrates, endowing them with remarkable physical and chemical properties. The Si grass decorated surfaces sum up to the general advantages of nanotexturing the importance of being silicon, that is the ease of integration with existent Si technology.

The enhanced low reflectivity of Si grass makes it promising as anti-reflective coating or absorber for Micro-Opto-Electronic-Systems (MOEMS) and in general for opto-electronic devices. An obvious application is in Si solar cells [1.8, 1.9] to optimize Si photodiodes [1.10] or sunlight sensors [1.11]. The surface area enhancement and the additional possibility of good control of surface energies by coating make the nanostructured surfaces ideal as functional element for microfluidics, micro-reactors or bio-sensors. Si Grass can find application as a catalytic structure for microfluidic systems [1.12] or, in combination with Si NWs for better interfacing Si and biological cells [1.13] (Figure 1.2-1 a). Recently, a new type of bonding technology has been devised based on the mechanical adhesion of a form-fitted bond of Si Grass [1.14]. It allows for repeated, reversible bonding and unbonding of devices on substrates treated by Nano-Velcro, with effects comparable to low level adhesives (Figure 1.2-1 b).

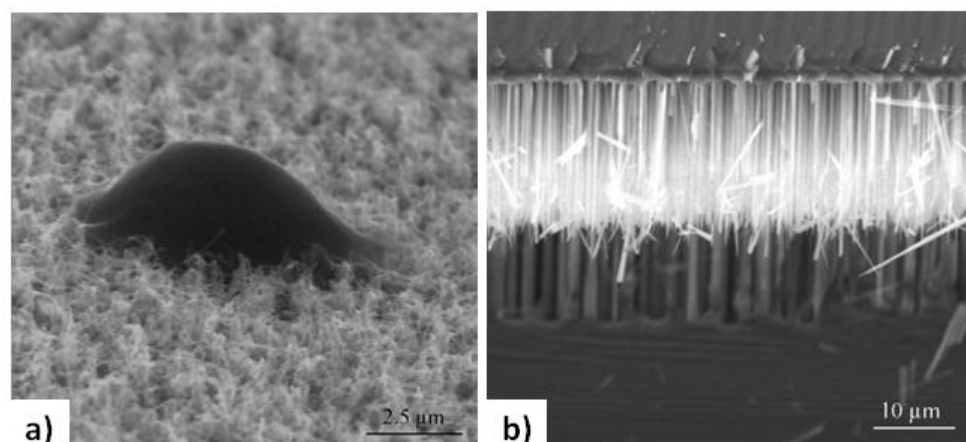


Figure 1.2-1 Applications of Si Grass.

a) chinese hamster ovaric cells on Si Grass. After V. Cimalla, M. Stubenrauch, F. Weise, M. Fischer, K. Tonisch, M. Hoffmann, O. Ambacher, *Applied Physics Letters*, 2007, **90** 2007, 10, 3.

b) Si Grass as Nano-Velcro. After M. Stubenrauch, M. Fischer, C. Kremin, S. Stoebenau, A. Albrecht, O. Nagel, *Journal of Micromechanics and Microengineering*, 2006, **16**, 6, S82-S87.

1.2.2 Schottky Contacts Over NW arrays

Fabrication of good quality Schottky contacts over nanostructures is of complex realization. As regards semiconductor NW arrays, front electrodes deposited directly onto them may be affected by high sheet resistance because of the poor physical contact of metal with the NWs. Furthermore the NWs-based device functionality may severely be reduced by shunting paths between the front electrode on top of the NW array and the back electrode on the rear of the substrate where NWs are grown [1.15]. Both these issues may be solved by embedding the NW array into a filling material [1.16, 1.17]. This latter, if insulating plays no active role in the actual working of the device while enhances the stability of the three-dimensional structure [1.17]. Aside the morphology of the NW array to be contacted, other challenges need to be afforded, such as those involving interface states, surface contamination, subsurface defects. All these factors affect the macroscopic electric behavior of metal-NWs junctions like, for example, the Schottky barrier height or the ideality factor [1.18, 1.19].

Schottky Barrier Diodes (SBDs) are the simplest semiconductor devices, but many high-performance applications in optoelectronic, high temperature, high-frequency and power fields rely on them. They are the basic building blocks of detectors, sensors, microwave diodes, gates of transistors, infrared and nuclear particle detectors. Therefore, the study of the conduction mechanisms of NW array-based SBDs (Figure 1.2-2) is of interest both from the fundamental physics perspective and the potentially applicative side.

1.2.3 Defect Characterization of NW Array-Based SBDs

First-principles as well as experimental studies of point and extended defects in bulk semiconductors are major topics of research, given the decisive effects of defects on the properties of these latter. A widely known example is the semiconductor doping. The addition of small amounts of donor or acceptor impurities to the semiconductor brings the material to change its electrical properties. This is of interest from the fundamental physics point of view but it is also the basis of the functionality of electronic or optoelectronic devices [1.22, 1.23]. The point defects are also important because they are involved in the diffusion processes and mediate the mass transport, hence contributing to equilibration during growth and to diffusion of dopants or other impurities during growth or annealing [1.24 – 1.26]. In general, by introducing levels within the forbidden gap, point and extended defects play an essential role in detrimental processes in semiconductor devices.

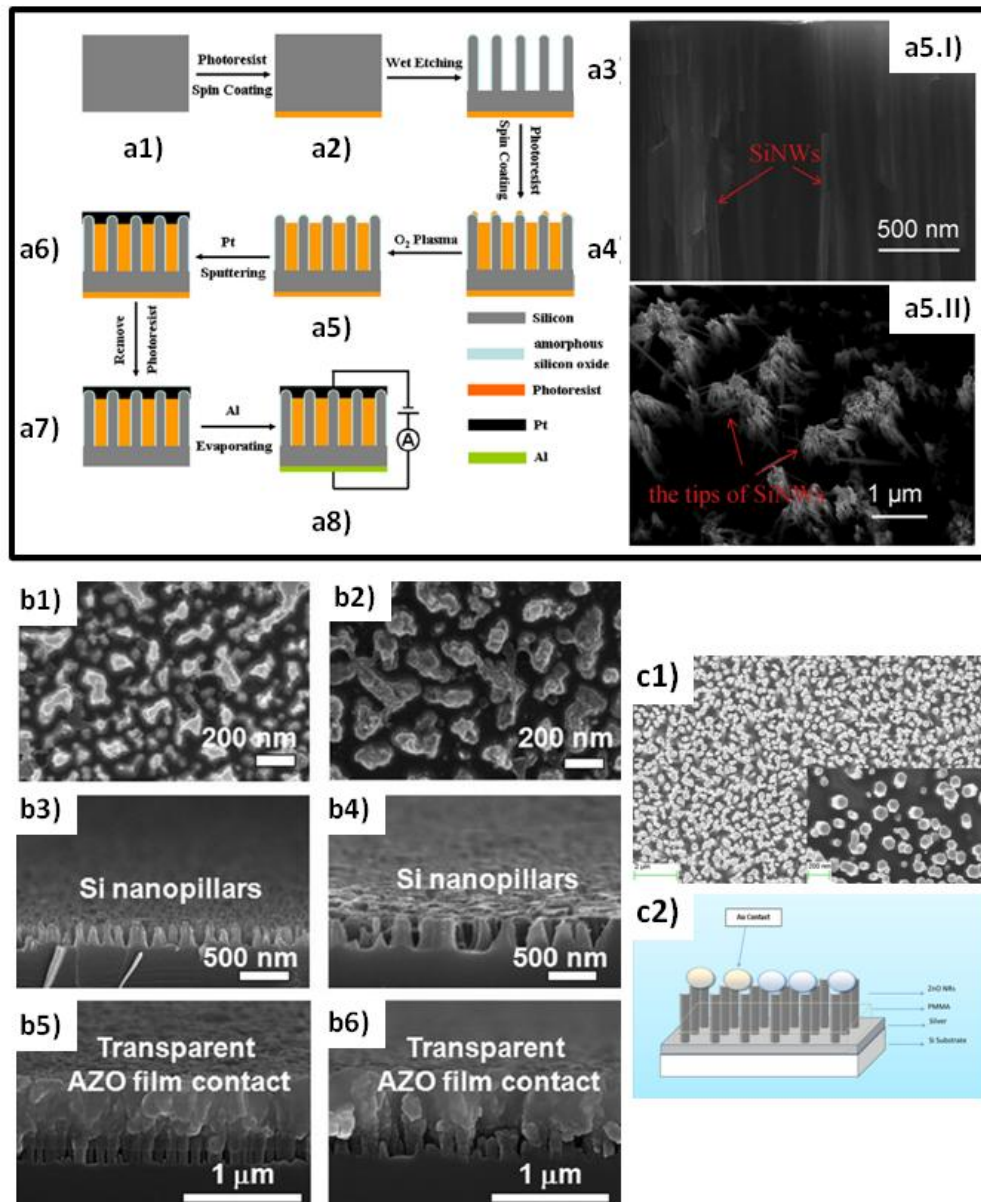


Figure 1.2-2 Semiconductor NW array-based Schottky diodes.

a1) – a8) Schematic illustration of the fabrication of Pt/p-Metal-Assisted wet Chemical Etched SiNWs devices. a1) – a3) NW wet etching process. a4) Photoresist spin coating over the Si NWs; the spin coating speed has been calibrated in order to get a polymer layer thickness less than the NWs height. a5) O₂ plasma dry etching of the remnants of photoresist from the exposed tips of Si NWs. SEM images of a5.I) cross section and a5.II) plane view of p-Si NWs after photoresist spin coating. a6) Pt contact deposition on the tips of p-SiNWs by electron beam evaporation. a7) Acetone removing of photoresist on wafer backside. a8) Current-Voltage measurement setup. After Z. Wang, M. Zhu, X. Chen, Q. Yan, J. Zhang, *Microelectronic Engineering*, 2013, **103**, 36–41.

b1) – b6) 3D radial heterojunction photodiode. b1, b2) Ag nanoparticle mask over p-Si substrate by annealing for different time durations. b3) – b4) Cross-sectional images after RIE etching of samples b1), b2) respectively, showing b3) an higher density, b4) a lower density of Si NWs. b5) – b6) AZO film was deposition on top of b3), b4) Si NWs, respectively. After S.-W. Jee, S.-J. Park, J. Kim, Y. C. Park, J.-H. Choi, J.-H. Jeong, J.-H. Lee, *Applied Physics Letters*, 2011, **99**, 053118.

c1) SEM image of as grown ZnO Nanorods, and in the inset after spin coating the insulating layer and subsequent soft backing. C2) Schematic illustration of Au/ZnO Nanorods Schottky diode. After I. Hussain, M. Y. Soomro, N. Bano, O. Nur, M. Willander, *Journal of Applied Physics*, 2013, **113**, 234509.

For bulk semiconductors Deep Level Transient Spectroscopy (DLTS) [1.29] is a mature, well established technique for studying electrically active defects. It has a sensitivity higher than almost any other equipollent methods. For example, in silicon it may detect impurities and defects at a concentration of one part in 10^{12} of the material host atoms. As it will be later discussed in detail (Subsection 4.1.3), the performing of DLTS needs the presence of a depletion region in the probed structures, which then most commonly are Schottky diodes or p-n junctions.

The semiconductor NWs exploitation as active layers in actual nanodevices brings the nano-world research to face another important issue, that is if and how NWs synthesis conditions induce the formation of levels in their bandgap. The study of defects in NWs is a field that is presently at its earliest stage [1.27, 1.28] (Figure 1.2-3). Many difficulties both technological and theoretical have to be overcome in order to adapt the traditional characterization techniques to the probing of defects in these new structures. Up to now technological issues hinder the DLTS application to single semiconductor NWs (Subsection 4.3.1). Thus the realization of NW array-based SBDs represents, aside the considerations illustrated in Subsection 1.2.2, a preliminary, necessary step for the successive application of DLTS to the study of electrically active defects in NWs. The filler material in this context, by avoiding shunting paths to the substrate, plays the fundamental role of allowing the DLTS to be performed only over the NW arrays excluding any unwanted influence from the substrate.

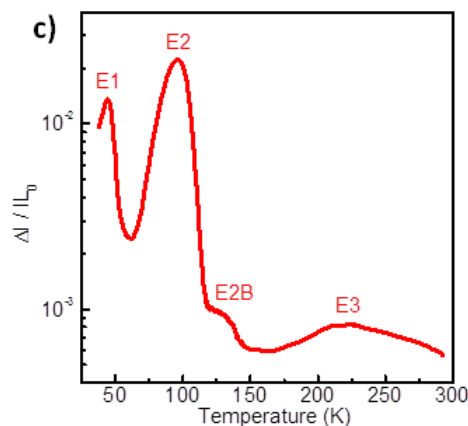
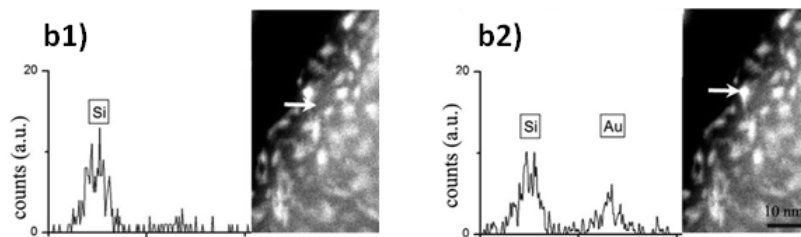
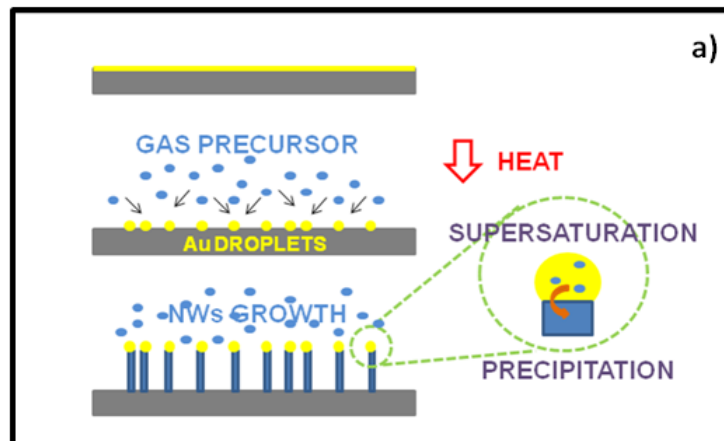


Figure 1.2-3 Defect level formation and characterization in Au-catalyzed VLS grown Si NWs.

a) Schematics of Growth of Au-catalyzed Si NWs by VLS mechanism. After A. Cavallini, S. Carapezzi, A. Castaldini, A. Irrera, *Physica B*, 10.106/j.physb.2013.11.021

b1), b2) Experimental proof of surface diffusion of Au from the NWs tip. EDX spectra and STEM images of a Si NW grown at 575 °C with 0.077 mbar silane partial pressure. These arrows show the location where the EDX spectrum has been taken. The brighter particles are unambiguously gold rich clusters, as three typical gold lines appear in the EDX spectrum about 2200 eV. After M. I. Hertog, J.-L. Rouviere, F. Dhalluin, P. J. Desré; P. Gentile, P. Ferret, F. Oehler, T. Baron, *Nano Letters*, **2008**, 8, 1544–1550.

c) Typical PICTS spectrum of P-doped VLS grown Si NWs, obtained with an emission rate $e_p = 512 \text{ s}^{-1}$ and a pulse width of 10 ms. The labels identify the four traps emitting at the peaked positions. The E2B level has the emission characteristics of the donor level E(0/+) peculiar of the phosphorus-vacancy (PV) pairs of the E-center. The E3 level has the thermodynamic characteristics of the donor (0/+) level of the Au-H complex. After K. Sato, A. Castaldini, N. Fukata, A. Cavallini, *Nano Letters*, **2012**, 12 (6) 3012.

1.3 Misalignment and Bundles Formation of Gallium Arsenide NWs

A Preliminary Lexicon Note to the Interested Reader

In the pages that will follow, as well as along all this thesis, many different fields will be met, each bringing with it its proper jargon. We have willingly kept the various terminologies, in order to respect the flavor of the original backgrounds. But to avoid useless confusion we also state now that the terms of nanopillar and nanofilament refer each to an one- or quasi one-dimensional structure with at least one nanoscale size. Then they have the same meaning of NW even if they are usually not used in NW related literature.

1.3.1 Pre-Growth and During Growth Engineering of Vertical Orientation in NWs

The growth of metal-catalyzed semiconductor NWs via the Vapor–Liquid–Solid (VLS) or Vapor–Solid–Solid (VSS) mechanism occurs generally in the crystal direction that minimizes the total free energy. In most cases the total free energy is dominated by the surface free energy of the interface between the semiconductor and the metal catalyst. For diamond and Zinc-Blende (ZB) crystals (Si, Ge, GaAs, InP) the semiconductor–catalyst interface often forms a single surface at the lowest-energy $(1\ 1\ 1)$ plane thus the NWs tend to grow in the $\langle 1\ 1\ 1 \rangle$ direction for most growth conditions. In particular, for compound ZB semiconductors and their alloys (GaAs, GaP, InAs and InP) $(1\ 1\ 1)_B$ (group-V terminated) is the lower energy plane [1.32]. As a consequence, the NWs generally grow in the $\langle 1\ 1\ 1 \rangle_B$ [1.33]. Other low-index growth directions occasionally reported include $\langle 0\ 0\ 1 \rangle$, $\langle 1\ 1\ 0 \rangle$ and $\langle 1\ 1\ 2 \rangle$. WZ NWs (ZnO, GaN) are often observed to grow along the $\langle 0\ 0\ 0\ 1 \rangle$ direction (*c*-axis). III-nitride NWs show less preference for a particular growth orientation, and their growth axes are perpendicular to the α -planes [1.34], m -planes [1.35, 1.36] and c -plane [1.37]. III–V NWs can also form a WZ crystal structure or exhibit polytypism [1.38] switching between ZB and WZ.

The simplest way to engineer the NW orientation relative to the growth surface is the choice of the crystal orientation of the substrate. For example, as discussed before, NWs with cubic crystal structure typically grow in the $\langle 1\ 1\ 1 \rangle$ direction and therefore they are often epitaxially grown on $(1\ 1\ 1)$ substrates to achieve out-of-plane vertically alignment. In the case of compound semiconductor NWs $(1\ 1\ 1)_B$ substrates are chosen for vertically aligned $\langle 1\ 1\ 1 \rangle_B$ oriented NWs. Similarly, vertically aligned WZ ZnO and GaN NWs can be grown on, for example, α -plane sapphire substrates. Also the surface of the growth substrate plays an important role in the subsequent NW orientation. A first preliminary step to NW growth is the

removal of the native oxide on substrate surface. Without proper removal of it NWs will grow without epitaxial relationship with the substrate, thus in a random direction relative to the surface. An *in situ* anneal step is a further common preliminary process before the NW growth. It desorbs any residual native oxide or contaminants from the substrate surface. It alloys too the metal catalyst and the substrate in order to form the initial interface that will eventually become the NW growth front.

It has been observed a diameter dependence of the NW orientation [1.39, 1.40]. The explanation is related to the surface energetic as the diameter is scaled and the surface-to-volume ratio is increased. Indeed the NWs grow in a direction that minimizes the total free energy. Below a critical diameter the free surface energy of the NW side facets begins to dominate and may control the growth direction.

An additional approach to modify the NW orientation is by means of growth conditions. By “growth conditions” it is generally understood the growth temperature, pressure (total or partial pressure of precursors) and precursor molar ratios (i.e. group V/III). The growth conditions are not necessarily independent of each other. As an example, the modification of the growth temperature may result in a change of the effective precursor molar ratios in the Metal Organic Chemical Vapor Deposition (MOCVD) technique. Furthermore, the growth conditions may vary through the various growth apparatus. As regards the growth temperature, for example, this parameter is measured indirectly of the susceptor or sample holder.

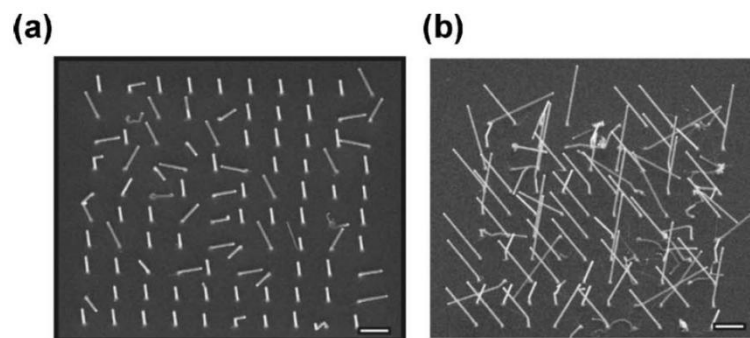


Figure 1.3-1 Effect of pressure and temperature on the epitaxial growth direction.

a) Array of 60-nm-diameter Si NWs grown at $p_{\text{SiH}_4}=80$ mTorr. Most of NWs grow in the vertical $\langle 111 \rangle$ direction, epitaxial to the substrate. b) 60-nm-diameter wires grown at $p_{\text{SiH}_4}=400$ mTorr. At this pressure all wires have kinks, but all are still epitaxial. After H. Schmid, M. T. Bjork, J. Knoch, H. Riel, W. Riess, P. Rice, T. Topuria, *Journal of Applied Physics* 2008, **103**, 024304–7.

1.3.2 Vertical Aligned Gallium Arsenide NWs in Nanophotonics

The control of the NW growth direction has several technological and fundamental scientific implications, like the manufacturability of arrays of Vertical Aligned (VA) NW field-effect transistors. Although much success has been reached in forming small area NW arrays, commercial logic products based on them will require millions (sometimes billions) of devices per chip. In this context a single misaligned NW may be the difference between a yielding or a faulty chip. Therefore the optical, electrical and mechanical properties of the NWs are expected to differ with the growth direction, which means they can be tailored by orientation.

Photonics is one of the most congenial applications of semiconductor NWs. In fact NWs may show peculiar optical characteristics, due to the size-related quantum confinement effect. Additionally they have such large aspect-ratio that makes them suitable to be exploited as waveguides or interconnects in photonic platforms [1.42]. Bulk GaAs is a compound semiconductor with high electron mobility and direct bandgap [1.43], features which make it a natural choice for high speed and optoelectronic devices. GaAs NWs are expectedly easy candidates to be employed in nanophotonics, where the vertical alignment of the NWs is a mandatory feature. In fact, VA NWs can be used as natural resonance cavities in lasers, without any fabricated mirror [1.44]. As regards light emitting diodes (LEDs), VA NWs lead to waveguided emission [1.45], which makes NW arrays advantageous in respect to the thin films. The same VA NWs architecture is beneficial for photovoltaic and photodetection applications [1.46].

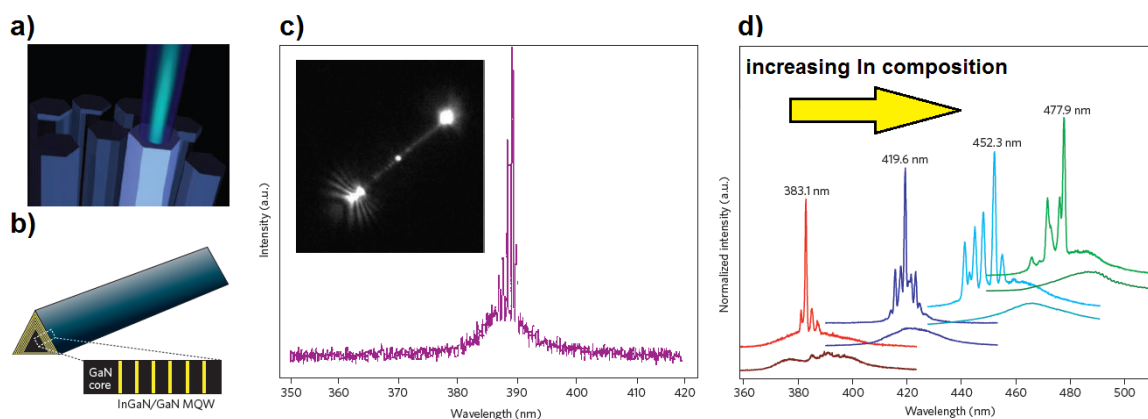


Figure 1.3-2 NW nanolasers.

a) Schematic of an optically pumped nanowire laser cavity. b) A multi-quantum-well (MQW) NW and magnified cross-sectional view of a NW facet showing the InGaN/GaN MQW structure. The InGaN layer is indicated in yellow. c) Lasing spectrum from an individual ZnO NW; in the inset a far-field optical image of a lasing GaN nanowire. d) Normalized lasing spectra collected from four representative MQW nanowire structures with different indium composition. After R. Yan, D. Gargas, P. Yang, *Nature Photonics*, 2009, **3**, 569 - 576.

1.3.3 Post-Growth Vertical Misalignment: Bending of NWs Under an Electron Beam

As already stated at the beginning, it is commonly accepted that the control over the NW orientation is exercised only during the growth. Less recognized is that the NW orientation may be influenced also by further factors. Few recent papers about self-attraction and bundling of ZnO nanorods and NWs [1.47 – 1.49] as well as of GaAs NWs [1.50, 1.51] have been published. The NW bending has been attributed to the interaction between the accumulation charges induced by electron-beam [1.47, 1.50], or to electrostatic interaction [1.48, 1.49]. The NW bending has been reported to occur during the NWs building up [1.48, 1.50] and, on the contrary, to be a post-growth occurrence [1.47, 1.48]. In all these cases the phenomenon has been mainly investigated towards determining the nature of the driving force responsible for the NWs bending, which has been deemed to be of electrostatic nature [1.47, 1.48, 1.51]. Little effort has been dedicated instead in understanding the coupled bundling effect, its nature and its possible consequences over the novel technological architectures and applications based on NW arrays.

13.4 Lateral Collapse and Bundling in Semiconductor NWs

We will elucidate the rising of the NWs clusters after the contacting of NWs in the framework of the studies about adhesion, friction, and compliance properties of natural and bio-mimetic contact surfaces [1.52]. This interdisciplinary field, which encompasses biology, physics, mechanical engineering and applied mathematics, recently has attracted great attention in view of the alluring perspective of artificial mimicking the natural contact surfaces in lizards and insects by means of synthetic structures [1.53, 1.54]. In this context, it is of major importance to avoid the self-adhesion of next-neighbor pillars (fibrils) because this drives to a reduction of the adhesiveness of the artificial surface. This occurrence, initially defined “lateral collapse of *fibrillar* structures”, has been quantitatively modeled [1.55] and experimentally verified by means of poly(dimethylsiloxane) (PDMS) fibrillar arrays [1.55], but never studied in semiconductor NWs, which are actually also pillars from a mechanical point of view.

1.3.5 Self-Assembly of NWs: a Way to NWs Patterning

A large body of research [1.56] has been devoted in the last years towards explaining, controlling, exploiting the elastocapillary self-assembly of vertical nanofilaments on substrates for nano/microfabrication and surface engineering issues (Figure 1.3-3). Elastocapillary self-assembly (or elastocapillary aggregation) is the mechanical deformation and change in the arrangement of a population of filaments influenced by capillary forces during wetting or drying of a liquid.

The materials which compose the filaments range from polymers to semiconductors to metals. The phenomenon, which could be detrimental in certain circumstances, has showed conversely good potentiality for solving the scalability issues of nanostructures, like enhancing their packing density [1.57 – 1.62], forming periodic superstructures [1.63 – 1.65], to reorient thin films into horizontal sheets and multidirectional circuits [1.66 – 1.70], and to fabricate intricate 3D microarchitectures [1.68, 1.71 – 1.74].

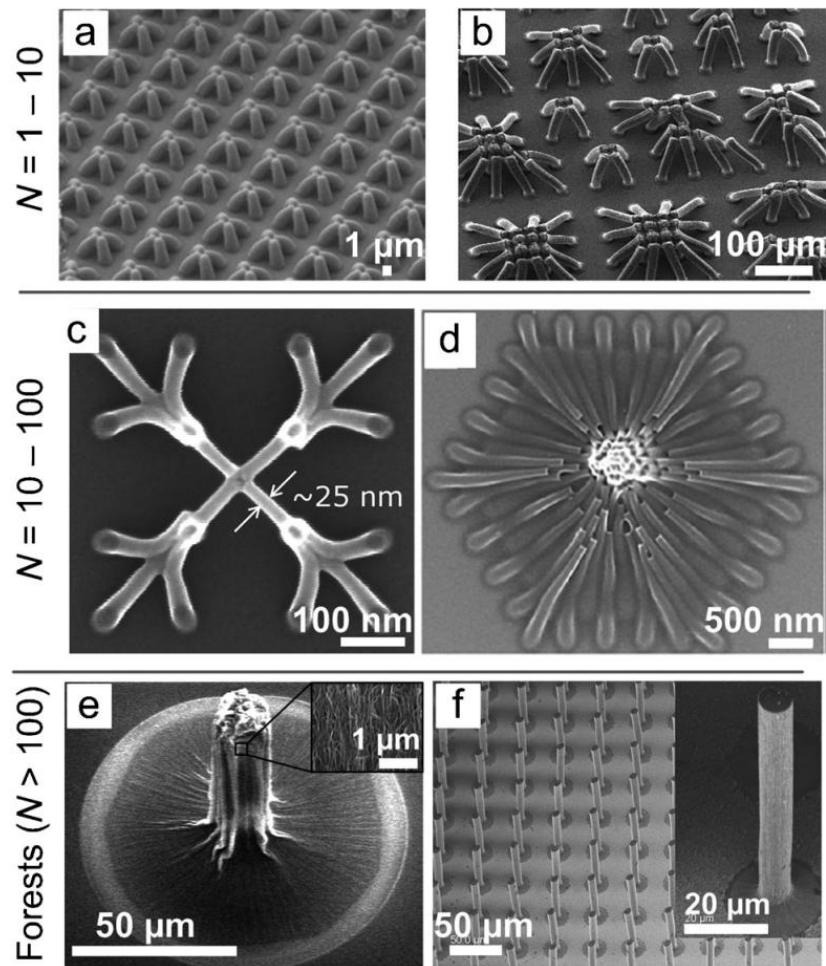


Figure 1.3-3 Examples of capillary self-assembly of top-gathering pillars.
a) Photoresist pillars fabricated by multibeam lithography. After D. Wu, Q.-D. Chen, B.-B. Xu, J. Jiao, Y. Xu, H. Xia, H. B. Sun, *Applied Physics Letters*, 2009, **95**, 091902.
b) SU8-epoxy pillars after capillary self-assembly and subsequent pyrolysis. After M. F. L. De Volder, R. Vansweevelt, P. Wagner, D. Reynaerts, C. Van Hoof, A. J. Hart, *Acs Nano*, 2011, **5**, 6593 – 6600.
c,d) Arrays of polymer nanopillars fabricated by electron-beam lithography, then clustered by capillary self-assembly. After H. Duan, K. K. Berggren, *Nano Letters*, 2010, **10**, 3710 – 3716.
e,f) CNT forest micropillars that aggregate by capillary self-assembly. After M. F. L. De Volder, S. J. Park, S. H. Tawfick, D. O. Vidaud, A. J. Hart, *Journal of Micromechanical Microengineering*, 2011, **21**, 045033.

Recently electron beam-induced bending of gold-coated epoxy nanopillars [1.78] has been demonstrated and proposed as a powerful patterning technique (Figure 1.3.4). The main focus of the research has been the explanation of the electron beam-induced bending, whose mechanism has been identified with a two-steps electrostatic process. First, electrons from the electron beam get implanted into the nanopillars as a result of their backscattering. Second, charging and induction produce an electric field inside the specimen. The ensuing electrostatic forces and torques deflect the nanopillars. The devised model has been successfully tested for gold-coated insulators, and both the model and the experimental results agree on the fact that doped-silicon nanopillars do not bend under electron beam, because of the much faster charge relaxation time, which prevents the steady-state charging building up.

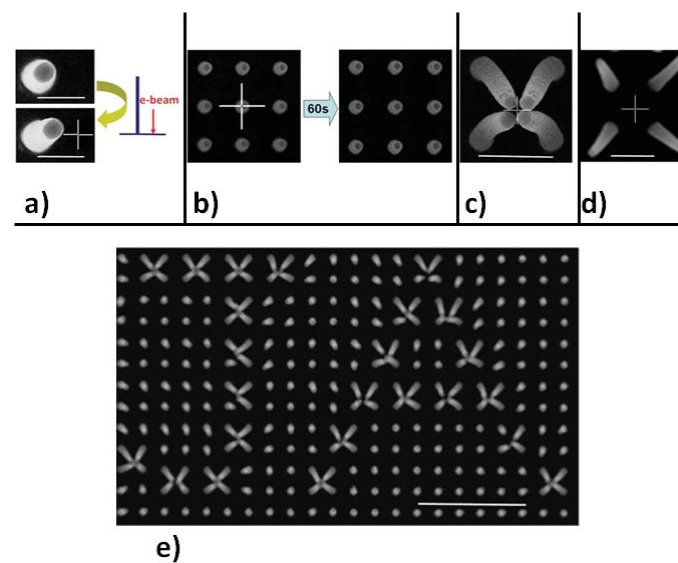


Figure 1.3-4 Arrays composed of grounded gold-coated epoxy nanopillars.

a) Position of a single nanopillar before (top) and after (bottom) electron beam exposure in spot mode; the white cross indicates the position of the electron beam. Scheme for the edge-on view is on the right. b) Image of a sample before (left) and after (right) 60 s exposure to the electron beam in spot mode, focused on the center of a single nanopillar. The white cross indicates the position of the electron beam. c) Inward bending and cluster formation upon focusing the electron beam in the center of four gold-coated nanopillar, disconnected from the ground. d) Outward bending of four carbon-coated nanopillar, disconnected from the ground. Scale bars are $1\ \mu\text{m}$ for a), $2\ \mu\text{m}$ for c) and d). e) Applications for patterning. Writing of letters in nanopost arrays through repeated exposure to the e-beam in spot mode. After A. Seminara, B. Pokroy, S. H. Kang, M. P. Brenner, J. Aizenberg, *Physical Review B*, 2011, **83**, 235438.

The study has duly stressed the fact that the patterning is due to both the bowing and the sticking together of the nanopillars, even if it has not dealt with this second, necessary process. Then the case of GaAs NWs electron beam-mediated bending coupled to the adhesion-induced bundling demonstrates the possibility of a procedure for the selective fabrication of NW integration over the nanoscale, with the great advantage that the semiconductor NWs allow for realization of nanoscaled semiconductor devices.

1.4 Objectives and Structure of This Thesis

This thesis has mainly focused on two different, cutting-edge aspects of research over semiconductor NW arrays as pivotal components of NW-based devices.

- Part I has dealt with the fabrication process of Si Grass and implementation of Si Grass-based SBDs. The conduction mechanism of the Si Grass-based SBDs has been studied. More importantly, the DLTS characterization of these devices has made it possible to probe the electrically active defects of the RIE etched Si NWs.
- Part II has been dedicated to present results over post-growth misalignment of originally VA NWs. A possible explanation of the experimental observation of the electron-beam induced bending has been proposed. The companion formation of NWs bundles has been successfully interpreted in the framework of the lateral collapsing of fibrillar structures.

Part I is composed of Chapters 2 – 4. Chapter 2 briefly illustrates the RIE etching process and the derivative Bosch process. The Bosch processing of Si substrates has been especially examined in the context of Si Grass fabrication. Successively the focus has been moved on the fabrication procedure we have followed for the Si Grass-based SBDs object of study of this work. Chapter 3 begins with a theoretical review about Schottky barrier formation and current transport in SBDs. Experimental results have been reported about Si Grass-based SBDs current-voltage characterizations. Different fitting models have been compared through the Akaike's Information Criterion, this finally allowing to find the most probable candidate as conduction mechanism for the Si Grass-based SBDs. Chapter 4 is the core of Part I. At the beginning the theory of DLTS technique for majority carriers traps is introduced. Then it follows a review on the existent literature about defect formation mechanisms in RIE processed bulk Si, in cross reference with the description of the RIE etching presented in Chapter 2. This part concludes with the DLTS results from Si grass-based SBDs. It is reported their comparison to DLTS results from reference SBDs based on bulk Si that has been RIE etched in conditions similar to the fabrication of Si Grass. The final discussion of both closes this part of the thesis.

Part II is composed of Chapters 5 – 6. Chapter 5 illustrates, first, the Molecular Beam Epitaxy (MBE) growth technique. Specific growth details for the both doped and undoped, Au-catalyzed GaAs NW arrays which has been studied in this thesis have been given. A complete characterization of the observed electron beam induced bending of the GaAs NWs is shown through a set of Scanning Electron Beam (SEM) micrographs. The few interpretations from literature of similar reported occurrences with GaAs or other semiconductor NWs have been presented. Reasons have been given for their rejection in the present case. An explanation of the phenomenon, based on the Scanning Electron Beam Induced Voltage (SEBIV) effect, has been proposed. Chapter 6 deals with the complementary NW bundles formation following the electron beam induced bending. After introducing the so called Gecko Effect, that is the adhesion properties possessed by natural surfaces of lizards and insects, the theory and the experimental results of lateral collapsing for fibrillar structures modeling such surfaces are briefly surveyed. The same model has been then successfully applied to explain the GaAs NWs clustering.

Chapter 7 is dedicated to the conclusions. As regards Part I, the main stress has been put on the DLTS measurements of semiconductor NW arrays. In this thesis has been set up an operative procedure for their DLTS characterization. Then, the DLTS measurements performed over Si Grass-based SBDs have been discussed in details with reference to the RIE of Si NWs and consequent RIE damages introduced. As regards Part II, the present study puts into evidence how not only the growth conditions control the NW orientation. Hence, they are not the only parameters to be taken into account for the realization of VA NW arrays. The mechanical and surface properties of the NWs together with the geometrical design of the NW arrays play a key role for post-growth misalignment. These parameters also matter in order to avoid the NWs bundling when departure from verticality is detrimental for the realization of NW array-based devices. On the other hand, the same parameters open to the benign possibility of locally engineering NW arrays in micro- and macro-templates.

BIBLIOGRAPHY

- [1.1] D. K. Ferry, *Science*, 2008, **319**,579.
- [1.2] W. Lu, P. Xie, and C. Lieber, *IEEE Trans. Electron Devices*, 2008, **55**, 2859.
- [1.3] Y. Huang, X. Duan, Y. Cui, L. J. Lauhon, K.-H. Kim, C. M. Lieber, *Science*, 2001, **294**, 1313.
- [1.4] X. Duan, Y. Huang, C. M. Lieber, *Nano Letters*, 2002, **2**, 487.
- [1.5] B. Tian, T. J. Kempa, C. M. Lieber, *Chemical Society Review*, 2009, **38**, 16.
- [1.6] P. J. Pauzauskie, P. Yang, *Materials Today*, 2006, **9**, 36.
- [1.7] J.-I. Hahm, C. M. Lieber, *Nano Letters*, 2004, **4**, 51.
- [1.8] D. S. Ruby, S. Zaidi, S. Narayanan, S. Yamanaka, R. Balanga, *Journal of Solar Energy Engineering-Transactions of the Asme*, 2005, **127** , 1, 146-149.
- [1.9] J. Yoo, K. Kim, M. Thamilselvan, N. Lakshminarayn, Y. K. Kim, J. Lee, K. J. Yoo, J. Yi, *Journal of Physics D-Applied Physics* 2008, **41** , 12, 7.
- [1.10] A. M. Moloney, L. Wall, A. Mathewson, G. Healy, J. C. Jackson, *Bellingham : SPIE: Int. Soc. Optical Engineering*, 2006, B1190-B1190.
- [1.11] C. Lee, S. Y. Bae, S. Mobasser, H. Manohara, *Nano Letters*, 2005, **5**, 12, 2438-2442.
- [1.11] M. Rournanie, C. Delattre, F. Mittler, G. Marchand, V. Meille, C. de Belle-fon, C. Pijolat, G. Tournier, P. Pouteau, *Chemical Engineering Journal* , 2008, **135**, S317-S326.
- [1.13] V. Cimalla, M. Stubenrauch, F. Weise, M. Fischer, K. Tonisch, M. Hoffmann, O. Ambacher, *Applied Physics Letters* , 2007, **90**, 10, 3.
- [1.14] M. Stubenrauch, M. Fischer, C. Kremin, S. Stoebenau, A. Albrecht, O. Nagel, *Journal of Micromechanics and Microengineering*, 2006, **16**, 6, S82-S87.
- [1.15] L. Tsakalacos, J. Balch, J. Fronheiser, B. Korevaar, O. Sulima, J. Rand, *Applied Physics Letters*, 2007, **91**, 233117.
- [1.16] A. C. E. Chia, R. R. LaPierre, *Nanotechnology*, 2011, **22**, 245304.
- [1.17] L. F. Voss, Q. Shao, C. E. Reinhardt, R. T. Graff, A. M. Conway, R. J. Nikolic, N. Deo, C. L. Cheung, *Journal Vacuum Science Technology B*, 2010, **28**, 916.
- [1.18] I. Hussain, M. Y. Soomro, N. Bano, O. Nur, M. Willander, *Journal of Applied Physics*, 2012, **112**, 064506.
- [1.19] I. Hussain, M. Y. Soomro, N. Bano, O. Nur, M. Willander, *Journal of Applied Physics*, 2013, **113**, 234509.

- [1.20] Z. Wang, M. Zhu, X. Chen, Q. Yan, J. Zhang, *Microelectronic Engineering*, 2013, **103**, 36–41.
- [1.21] S.-W. Jee, S.-J. Park, J. Kim, Y. C. Park, J.-H. Choi, J.-H. Jeong, J.-H. Lee, *Applied Physics Letters*, 2011, **99**, 053118.
- [1.22] H.J. Queisser, E.E. Haller, *Science*, 1998, **281**, 945.
- [1.23] C.G. Van de Walle, D.B. Laks, G.F. Neumark, S.T. Pantelides, *Physical Review B*, 1993, **47**, 9425.
- [1.24] S. Limpijumngong, C.G. Van de Walle, *Physical Review B*, 2004, **69**, 035207.
- [1.25] A. Janotti, C.G. Van de Walle, *Physical Review B*, 2007, **76**, 165202.
- [1.26] A. Janotti, M. Krcmar, C.L. Fu, R.C. Reed, *Physical Review Letter*, 2004, **92**, 085901.
- [1.27] A. Motayed, S. Krylyuk, A. Davydov, *Applied Physics Letters*, 2011, **99**, 113107.
- [1.28] K. Sato, A. Castaldini, N. Fukata, A. Cavallini, *Nano Letters*, 2012, **12**, 6, 3012.
- [1.29] G.L. Miller, D.V. Lang, L.C. Kimerling, *Annual Review of Materials Science*, 1977, **377**.
- [1.30] A. Cavallini, S. Carapezzi, A. Castaldini, A. Irrera, *Physica B*, 10.106/j.physb.2013.11.021
- [1.31] M. I. Hertog, J.-L. Rouviere, F. Dhalluin, P. J. Desré; P. Gentile, P. Ferret, F. Oehler, T. Baron, *Nano Letters*, 2008, **8**, 1544–1550.
- [1.32] W. Braun, V. M. Kaganer, A. Trampert, H.-P. Schonherr, Q. Gong, R. Notzel, L. Daweritz, K. H. Ploog, *Journal of Crystal Growth*, 2001, **227–228**, 51–5.
- [1.33] K. Hiruma, M. Yazawa, T. Katsuyama, K. Ogawa, K. Haraguchi, M. Koguchi, H. Kakibayashi, *Journal of Applied Physics*, 1995, **77**, 447–62.
- [1.34] S. Gradecak, F. Qian, Y. Li, H.-G. Park, C. M. Lieber, *Applied Physics Letter*, 2005, **87**, 173111.
- [1.35] X. Duan, C. M. Lieber, *Journal of American Chemical Society*, 2000, **122**, 188–9.
- [1.36] R.-S. Chen, S.-W. Wang, Z.-H. Lan, J T.-H. Tsai, C.-T. Wu, L.-C. Chen, K.-H. Chen, Y.-S. Huang, C.-C. Chen, *Small*, 2008, **4**, 925–9.
- [1.37] T. Kuykendall, P. J. Pauzauskie, Y. Zhang, J. Goldberger, D. Sirbully, J. Denlinger, P. Yang, *Nature Materials*, **3**, 524–8.
- [1.38] M. Koguchi, H. Kakibayashi, M. Yazawa, K. H. Katsuyama, Toshio, *Japanese Journal of Applied Physics*, 1992, **31**, 2061–5.
- [1.39] Y. Cui, L. J. Lauhon, M. S. Gudixsen, J. Wang, C. M. Lieber, *Applied Physics Letters*, 2001, **78**, 2214–6.

- [1.40] Y. Wu, Y. Cui, L. Huynh, C. J. Barrelet, D. C. Bell, C. M. Lieber, *Nano Letters*, 2004, **4**, 433–6.
- [1.41] H. Schmid, M. T. Bjork, J. Knoch, H. Riel, W. Riess, P. Rice, T. Topuria, *Journal of Applied Physics* 2008, **103**, 024304–7.
- [1.42] R. Yan, D. Gargas, P. Yang, *Nature Photonics*, 2009, **3**, 569 - 576.
- [1.43] A. G. Baca, C. Ashby, *Fabrication of GaAs Devices*, EMIS processing series, 2009.
- [1.44] M. H. Huang, S. Mao, H. Feick, H. Yan, Y. Wu, H. Kind, E. Weber, R. Russo, P. Yang, *Science*, 2001, **292**, 5523, 1897-1899.
- [1.45] R. Könenkamp, R. C. Word, C. Schlegel, *Applied Physics Letters*, 2004, **85**, 24, 6004-6006.
- [1.46] W. Wei, X. Y. Bao, C. Soci, Y. Ding, Z. L. Wang, D. Wang, *Nano Letters*, 2009, **9**, 8, 2926-2934.
- [1.47] X. Wang, C. J. Summers, Z. L. Wang, *Applied Physics Letters*, 2005, **86**, 013111.
- [1.48] J. Liu, S. Lee, K. Lee, Y. H. Ahn, J.-Y. Park, K. H. Koh, *Nanotechnology*, 2008, **19**, 185607.
- [1.49] H. Xinhai, G. Wang, L. Zhou, J. G. Hou, *Chemical Communications*, 2006, **2**, 212–214.
- [1.50] S. Plissard, G. Larrieu, X. Wallart, P. Caroff, *Nanotechnology*, 2011, **22**, 275602.
- [1.51] D. Xing, S. A. Dayeh, V. Veeramuthu, A. Larrue, J. Wang, H. Su, C. Soci, *Nano Letters*, 2011, **11**, 4947–4952.
- [1.52] A. Jagota, C.Y. Hui, *Materials Science and Engineering R*, 2011, **72**, 253–292.
- [1.53] D. H. Lee, Y. Kim, R. S. Fearing, R. Maboudian, *Langmuir*, 2011, **27**, 11008–11016.
- [1.54] A. K. Geim, S. V. Dubonos, I. V. Grigorieva, K. S. Novoselov, A. A. Zhukov, and S. Y. Shapoval, *Nature Materials*, 2003, **2**, 7, 461–463.
- [1.55] N. J. Glassmaker, A. Jagota, C.-Y. Hui, J. Kim, , *Journal of the Royal Society Interface*, **2004**, 1, 23–33.
- [1.56] M. De Volder , A. J. Hart, *Angewandte Chemie International Edition*, 2013, **52**, 2 – 16
- [1.57] Z. C. Liu, L. J. Ci, S. Kar, P. M. Ajayan, J. Q. Lu, *IEEE Transactions on Nanotechnology*, 2009, **8**, 196-203.
- [1.58] E. Verploegen, A. J. Hart, M. De Volder, S. Tawfick, K. K. Chia, R. E. Cohen, *Journal of Applied Physics*, 2011, **109**, 094316.

- [1.59] M. F. L. De Volder, S. J. Park, S. H. Tawfick, D. O. Vidaud, A. J. Hart, *Journal of Micromechanical Microengineering*, 2011, **21**, 045033.
- [1.60] D. Copic, S. J. Park, S. Tawfick, M. F. L. De Volder, A. J. Hart, *Lab on a Chip*, 2011, **11**, 1831– 837.
- [1.61] C. Journet, S. Moulinet, C. Ybert, S. T. Purcell, L. Bocquet, *Europhysics Letters*, 2005, **71**, 104 – 109.
- [1.62] D. Copic, S. J. Park, S. Tawfick, M. De Volder, A. J. Hart, *Journal of Visualized Experiments*, 2012, **65**, e3980.
- [1.63] N. Chakrapani, B. Q. Wei, A. Carrillo, P. M. Ajayan, R. S. Kane, *Proceedings of the National Academy of Sciences USA*, 2004, **101**, 4009 – 4012.
- [1.64] M. De Volder, S. H. Tawfick, S. J. Park, D. Copic, Z. Zhao, W. Lu, A. J. Hart, *Advanced Materials*, 2010, **22**, 4384 – 4389.
- [1.65] H. Liu, S. H. Li, J. Zhai, H. J. Li, Q. S. Zheng, L. Jiang, D. B. Zhu, *Angewandte Chemie*, 2004, **116**, 1166–1169; *Angewandte Chemie International Edition*, 2004, **43**, 1146–1149.
- [1.66] S. Tawfick, M. De Volder, A. J. Hart, *Langmuir*, 2011, **27**, 6389–6394.
- [1.67] Y. Hayamizu, T. Yamada, K. Mizuno, R. C. Davis, D. N. Futaba, M. Yumura, K. Hata, *Nature Nanotechnology*, 2008, **3**, 289–294.
- [1.68] S. Tawfick, A. J. Hart, M. De Volder, *Nanoscale*, 2012, **4**, 3852 –3856.
- [1.69] Y. Hayamizu, R. C. Davis, T. Yamada, D. N. Futaba, S. Yasuda, M. Yumura, K. Hata, *Physical Review Letters*, 2009, **102**, 175505.
- [1.70] E. R. Meshot, K. D. Patel, S. Tawfick, K. A. Juggernaut, M. Bedewy, E. A. Verploegen, M. F. L. De Volder, A. J. Hart, *Advanced Functional Materials*, 2012, **22**, 577–584.
- [1.71] M. F. L. De Volder, D. O. Vidaud, E. R. Meshot, S. Tawfick, A. J. Hart, *Microelectronical Engineering*, 2010, **87**, 1233 – 1238.
- [1.72] See Ref. [24].
- [1.73] M. F. L. De Volder, S. Tawfick, S. J. Park, A. J. Hart, *ACS Nano*, 2011, **5**, 7310–7317.
- [1.74] M. De Volder, D. Reynaerts, C. Van Hoof, S. Tawfick, A. J. Hart, *IEEE Sensors*, 2010, 2369 – 2372.

[1.75] D. Wu, Q.-D. Chen, B.-B. Xu, J. Jiao, Y. Xu, H. Xia, H. B. Sun, *Applied Physics Letters*, 2009, **95**, 091902.

[1.76] H. Duan, K. K. Berggren, *Nano Letters*, 2010, **10**, 3710 – 3716.

[1.77] M. F. L. De Volder, R. Vansweevelt, P. Wagner, D. Reynaerts, C. Van Hoof, A. J. Hart, *Acs Nano*, 2011, **5**, 6593 – 6600.

[1.78] A. Seminara, B. Pokroy, S. H. Kang, M. P. Brenner, J. Aizenberg, *Physical Review B*, 2011, **83**, 235438.

PART I
ELECTRICAL AND
DEFECT LEVEL
CHARACTERIZATION
OF SI GRASS-BASED SBDS

CHAPTER 2

Si Grass Growth and Si Grass-Based SBDs Fabrication

2.1 Reactive Ion Etching (RIE) and the Bosch Process

The high fidelity transfer of a pattern onto a substrate is essential to the semiconductor technology. This process consists of two steps: lithographic resist patterning and the subsequent etching of the underlying material.

Basic steps to the etching [2.1] are:

- transport of etchants to surface (flow and diffusion)
- surface processes (adsorption, reaction, desorption)
- removal of product species (diffusion and flow).

and they are essentially the same for both wet etching and dry, or plasma, etching techniques aside that diffusion in the gas phase is faster than in the liquid phase, and that in plasmas there are many possibilities to accelerate ions, providing extra energy to the process.

2.1.1 Inductively Coupled Plasma Reactive Ion Etching (ICP RIE)

The technical aspects that define the plasma etching systems are how to control the generation of ions and how to direct them towards their target. The plasma etching mechanism regards how ions can either mechanically or chemically remove atoms from the substrate, once they have reached it, and defines the etching chemistry and required etch mask.

Plasma Generation for RIE

In plasma etch systems the plasma is generated by coupling electromagnetic field energy into the gas species. The starting point is gas injection into a vacuum system. The initial ionized electrons are accelerated by the electromagnetic field here present and they consequently collide with gas molecules. These collisions are such

to further ionize the gas and further generate an increasing population of ions and electrons. The applied electromagnetic field is time-varying (most commonly, a Radio Frequency -RF- electric field) because the injected gas is ionized by electrons more efficiently than in a static electric field. In fact massive ions are slower and cannot track the rapidly oscillating field variations. Lighter electrons will acquire a larger speed with the same energy input, and tend to leave the plasma. Alternating electrons multiply the opportunities to scatter and further ionize the gas. By increasing the electromagnetic field energy, the creation of ions increases over the loss mechanisms until the **Townsend Discharge** occurs, which is a breakdown event [2.2].

According to the techniques used to couple electromagnetic field energy into the gas species, we distinguish in:

- **Capacitive Coupled Plasmas (CCP) RIE systems** (Figure 2.1-1). A time-varying electric field is created by a RF voltage applied between an anode and a cathode plate. By placing a capacitor between the anode plate and the RF supply, negative charge accumulates on the plate (the **table**), and this leads to the rising of a potential difference between the charge neutral plasma and the negatively charged plate, called the **self-bias V_b** . The resulting electric field drives the positive ions in plasma towards the negatively charged table, which is the basis for traditional RIE.

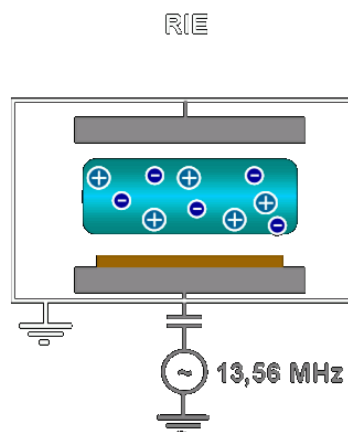


Figure 2.1-1 CCP RIE schematic chamber design.

- **Inductively Coupled Plasmas (ICP) RIE systems** (Figure 2.1-2). A RF magnetic field is provided by a coil wrapped around the RIE plasma discharge region. The varying magnetic field induces an electric field that tends to circulate the plasma in the plane parallel to the CCP plates. The plasma acts then as a secondary coil in a transformer, accelerating the electrons and ions, and thereby causing collisions. The lighter electrons acquire a larger speed than

ions with the same energy input and they tend to leave the plasma. The plasma cloud develops a positive static potential, called the plasma **voltage** V_{plasma} , with respect to the surroundings. As a result the plasma ions accelerate towards the chamber walls. By independently biasing the wafer chuck the energy of the ion bombardment of the wafer may be enhanced.

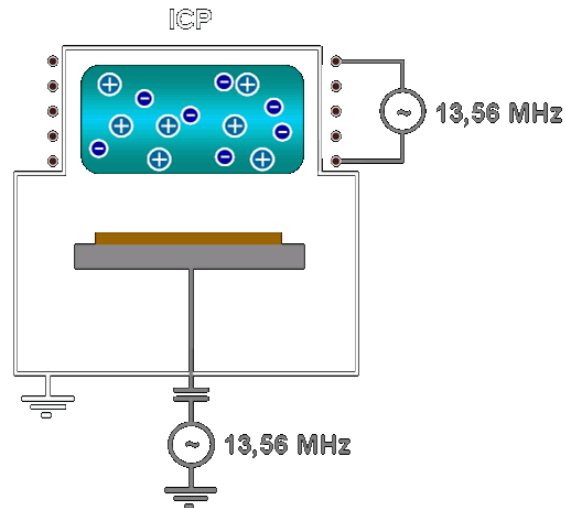


Figure 2.1-2 ICP RIE schematic chamber design.

Despite a constant flux of charged particles getting out of the plasma, the discharge is sustained through ionization of the neutral gases entering the chamber. The relaxation of the gas species from excited states causes a plasma glow, while in the nearby of the chamber walls and wafer surface the large electric field results in electron depletion and absence of ionization, leading to a non-glowing region, the so-called **dark space**.

The ICP method produces a dense plasma with an electron density about 10^{12} cm^{-3} . The high plasma density gives 5-10 times higher etch rate than in traditional CCP RIE systems, while the supply of radicals is the limiting factor in the etch process.

Some systems combine ICP with the traditional RIE. This means the possibility to change ion density, that is the number of ions reaching the substrate for the chemical etching process, and other plasma parameters by means of the ICP. This does not significantly perturb the incident energy of the ions, controlled by the CCP, which then controls the mechanical etching process.

Plasma Etching Mechanism

The main mechanism involved in plasma etching is the chemical etching: a chemical reaction takes place between a solid atom of the substrate and an etchant gas ion, to

form a molecule which is successively removed from the substrate [2.1]. Some sputtering component is also present because of the existing DC bias applied to the substrate, but usually this physical etching is negligible. The etching process may be subdivided in sequential steps (Figure 2.1-3):

1. etchant flow,
2. formation of the reactive ion,
3. diffusion of the reactive ion at the surface to be etched,
4. adsorption of the reactive ion at the surface
5. chemisorption of the reactive ion at the surface, i.e. a chemical bond is formed between the reactive ion and the atom of the substrate, with formation of the product molecule,
6. desorption of the product molecule,
7. diffusion of the product molecule,
8. pumping out from the reactor of the product molecule.

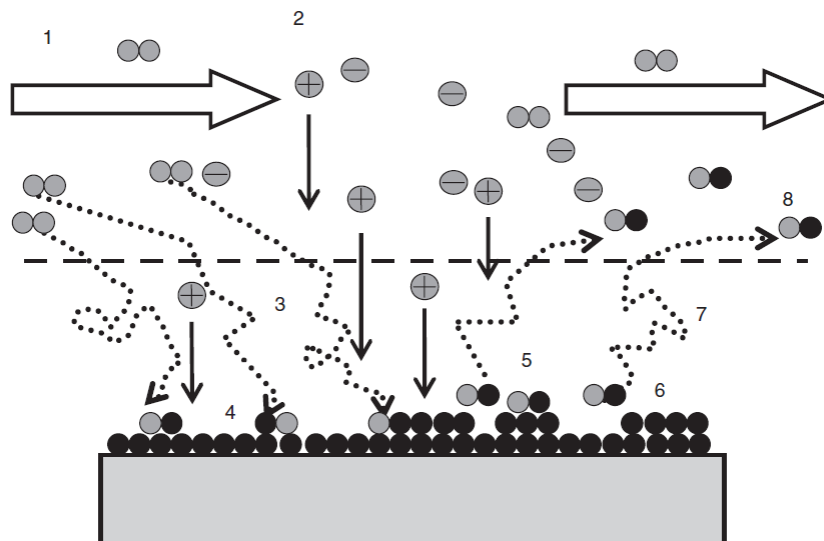


Figure 2.1-3 Basic Processes in Plasma Etching. 1: etchant flow. 2: ionization. 3: diffusion. 4: adsorption. 5: reaction. 6: desorption. 7: diffusion. 8: pump out. After S. Franssila, *Introduction to Microfabrication, Second Edition*, John Wiley & Sons 2010

Etch Chemistry of silicon

Reactions that lead to bonds stronger than the Si–Si bond will etch silicon, then the bond energies are indicative of possible etching reactions. Because silicon–halogen bonds are stronger than Si–Si bonds, fluorine, chlorine and bromine are all suitable candidates as etchant species for Si [2.1]. In the following we will concentrate over fluorine-based etching obtained by SF_6 source gas, because it is the etchant gas which has been used to realize our samples.

Different collision processes occur in the plasma [2.3], which lead to atomic fluorine generation. By decreasing order of importance:

- Impact dissociation: $SF_6 + e^- \rightarrow SF_5 + F + e^-$,
- Dissociative attachment: $SF_6 + e^- \rightarrow SF_5^- + F$,
- Impact ionization: $SF_6 + e^- \rightarrow SF_5^+ + F + 2e^-$.

The products of these processes then undergo a multitude of recombination, dissociation, and ionization processes, whose detailed description is outside the scope of this thesis. The three main steps which constitute the surface chemistry of the etching process are:

- Adsorption: $F(g) \rightarrow F(ad)$,
- Chemisorption: $Si(s) + 4F(ad) \rightarrow SF_4(ad)$,
- Desorption: $SF_4(ad) \rightarrow SF_4(g)$,

The desorption usually would constitute the rate limiting step of the total process, but the ion bombardment assistance instead brings the supply of atomic fluorine to be the only limiting factor. Also, it promotes the chemisorption of fluorine atoms to Si atoms.

2.1.2 Bosch Process and Si Grass Growth

Etching Profiles

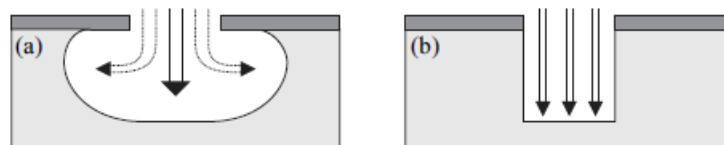


Figure 2.1-4 a) Isotropic profile by thermally activated etching, and b) ion-induced etched anisotropic profile.

The etching front may be distinguished in being isotropic or anisotropic (Figure 2.1-4), according to that it proceeds as a spherical wave from all points open to the etchant and then the lateral extent under the mask (undercutting) is identical to the vertical etched depth, or not. The degree of anisotropy depends on the specific plasma-Si interactions [2.1]. If adsorption of the radicals, chemisorptions and desorption of the reaction products, are all thermally activated, then the etching should be spontaneous and isotropic. When at least one of the steps is not, and ions bombardment is necessary, then the etching is anisotropic (Figure 2.1-5).

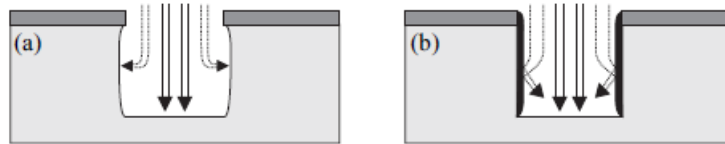


Figure 2.1-5 Methods for anisotropic etching: a) suppression of the spontaneous chemical component relative to the ion-induced component, b) surface passivation.

Sometimes, undercutting is desirable, for instance in order to fabricate free-standing beams and plates for Micro-Electro-Mechanical Systems (MEMS) [2.4]. On the other hand, for fine structure fabrication and lately for nanostructure fabrication is necessary an anisotropic etching, which may result in a vertical or almost vertical profiles.

In fluorine-based RIE of silicon, the volatile reaction product SF_4 is spontaneously formed, giving rise to anisotropic but not high aspect-ratio profiles. Special techniques have to be adopted to suppress the lateral etching and enhance the anisotropy [2.5], which may be grouped in two categories:

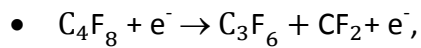
1. by reduction of the spontaneous chemical reaction of fluorine radicals (Figure 2.1-5 a),
2. by passivation of the silicon surface (Figure 2.1-5 b).

Bosch Process

Both Cryogenic Sidewall Passivation [2.6, 2.7] and Bosch Process [2.8] rely on fluorine-based ICP RIE, where an high degree of anisotropy is reached through sidewall passivation. A protective layer is formed on the sidewalls, resulting in the slowing down of the sidewalls etch rate with respect to the horizontal surfaces. The two techniques fall into the second of the above mentioned categories.

In the **Cryogenic Sidewall Passivation** technique O_2 gas is added to the SF_6 plasma. Moreover a cryogenically cooled sample holder allows to cool the silicon substrate to liquid nitrogen temperatures. At low temperatures the addition of oxygen to the fluorine plasma enables the formation of SiO_xF_y , a very efficient passivation layer, which evaporates when the sample is brought to room temperature [2.9].

In the **Bosch**, or Time Domain Multiplexed (TDM), **Process** the etch and the passivation chemistries are separated in time, with continuous switching between etching and passivation processes. The etchant gas is SF_6 , while the C_4F_8 is commonly used in the passivation step. This latter leads to formation of CF_2 through the reaction



and then adsorbs on the surfaces forming a soft teflon-like polymer film, $(CF_2)_n$.

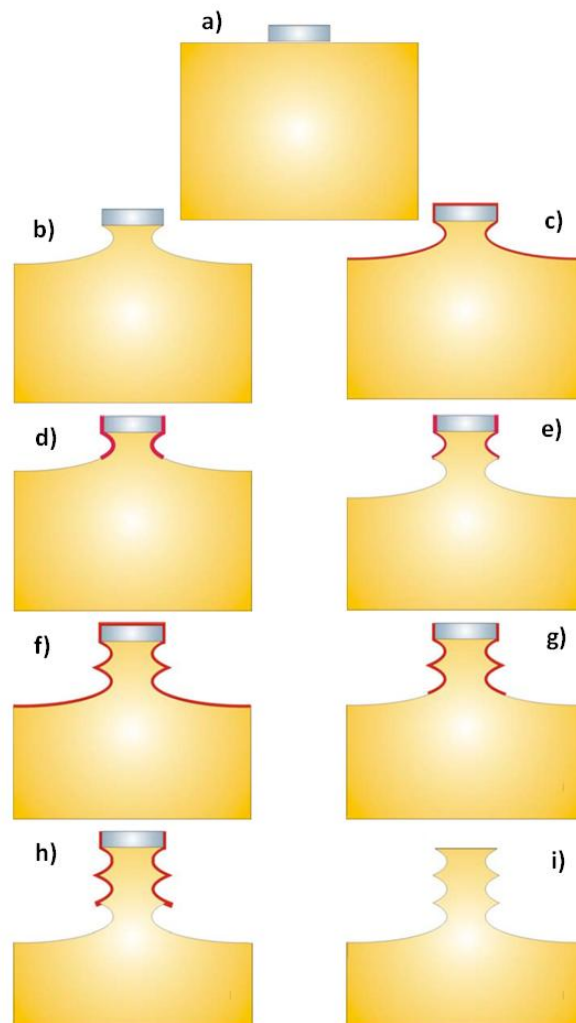


Figure 2.1-6 Bosch process steps. a) Deposition of a masking layer over Si substrate. b) STEP 0: Si etching, c) STEP 1: passivation, d) STEP 2.I: polymer etching, e) STEP 2.II: Si etching. f) – h) one cycle repetition. i) final removing of polymer.

A simplified Bosch sequence is the following (Figure 2.1-6):

0. short SF_6 -based etching step of the masked silicon substrate;
1. a thin fluorocarbon film is deposited on the wafer by substituting in the chamber SF_6 with C_4F_8 ;
2. C_4F_8 gas is substituted with SF_6 gas. This etching step is subdivided into two parts: in the first the passivation layer is removed from the horizontal surfaces due to the directional ion bombardment. Subsequently starts the anisotropic etching of silicon, the vertical sidewalls been protected by the

passivation layer if the ratio between the etching and passivation time is not too large;

3. the passivation step 1. is repeated.

The cycles of passivation/etching steps are repeated until the desired features depth is reached. The switching between passivation/etching step produces a sidewall corrugation, often referred to as **scalloping**, which depends on the etching time, the passivation layer thickness and the plasma density in both the steps.

Si Grass as a Self-Organized Nanostructure

The fabrication methods for micro- and nanostructuring of silicon surfaces are classified into organized and self-organized. The distinction between the two lies in if an additional process step (as lithography) is necessary in order to define fundamental geometrical properties (like shape, arrangement and density) of the sample. In self-organized processes the pattern of the structures arises from physical and chemical principles intrinsic to the system. Then they are independent from limiting factors of the additional, geometry-defining techniques (like resolution) used in organized fabrication methods. However, the possible geometries of self-organized structures are mostly limited and also difficult to control.

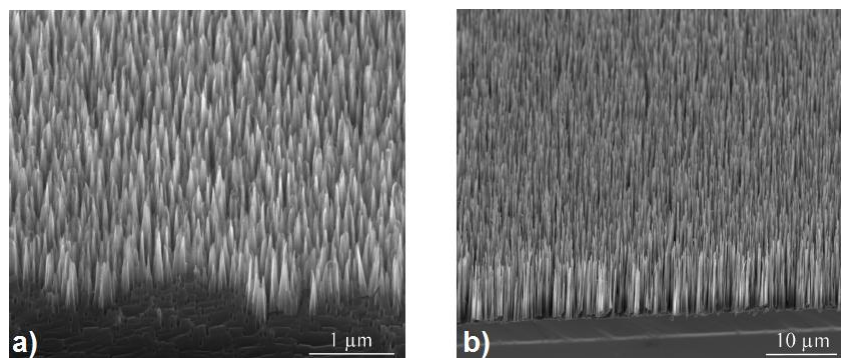


Figure 2.1-7 a) RIE and b) BOSCH processed Si grass.

As regards plasma processes, the complexities of internal relations and interference factors may lead to instabilities, fluctuations or even breakdown, preventing a reproducible fabrication process. Si Grass is a modification of primitive surface roughness, evolving into the growth of an array of self-organized, needle-like nanostructures. The observation of roughening occurrence in RIE processed silicon surfaces dates back to the middle of the 1980's [2.10, 2.11]. The terms of 'Silicon Grass' and 'Black Silicon' were related to the characteristic surface appearance (Figure 2.1-7) and its ensuing low reflectivity in the visible spectrum.

If the goal is the homogeneous etching for microfabrication of defined structures then Si Grass occurrence is detrimental, and research has been devoted to its

prevention. In 1995 a technique to optimize plasma etching processes, the 'Black Silicon Method' [2.12], has been developed. In it the Black Si is used in order to find the proper operating point of a RIE etching process. On the contrary, when the nanostructuring of the Si surface is searched for, then it is important to get a reproducible generation of Si Grass. Consequently study has been also aimed to this end. Different theories about the origin of Si Grass has been developed, the detailed mechanism of its growth and of its properties yet to be understood. The majority have discussed the occurrence of a so-called nanomask (or micromask) as explanation for the structures birth.

The literature on the topic [2.11 - 2.14] shows that there are different pathways which lead to nanomasking, and that the models to interpret it are tightly interwoven with the experimental setups. Anyway, nearly all theories share the concept of a nanomask consisting of a distribution of clusters with a material of high etch selectivity relative to Si (that is the ratio of the etch rate of Si to the etch rate of other materials) leading to a nucleation site for the Si grass structure formation.

2.1.3 Si Grass Samples

The Si grass samples object of this work are the result of Bosch processing the surface of p-type (B as dopant atom) Si substrates, whose resistivity was of 1-10 Ωcm correspondent to doping density of $1.4\text{e}15 - 1.5\text{e}15 \text{ cm}^{-3}$. The thickness of the substrates was of 525 μm . SF_6 has been used as the etchant gas, while C_4F_8 for the passivation layer deposition. The nanomasking at the origin of the Si grass occurrence (see subsection 2.1.2) has been obtained by unbalancing the cycles composing the Bosch process, inducing an excess of the passivation step (Figure 2.1-6 c) with respect to with the etching step (Figure 2.1-6 d). As a consequence the polymer layer is only partially removed and then a parasitic masking is formed, protecting spotted regions of the Si surface from the following etching by F atoms.

Subsequent Scanning Electron Microscopy (SEM) characterization has been performed (Figure 2.1-8) in order to get a morphological survey of the nanostructures. The extracted height distribution (Figure 2.1-9 a) shows that there is one prominent peak, located at average height $\sim 4.4 \mu\text{m}$, but also a minor peak at average height $\sim 3.5 \mu\text{m}$, suggesting that the NW height population is an overlapping of at least two different distributions, as it is also evident by visual inspection of SEM images of the cross section (Figure 2.1-8 b), c), d).

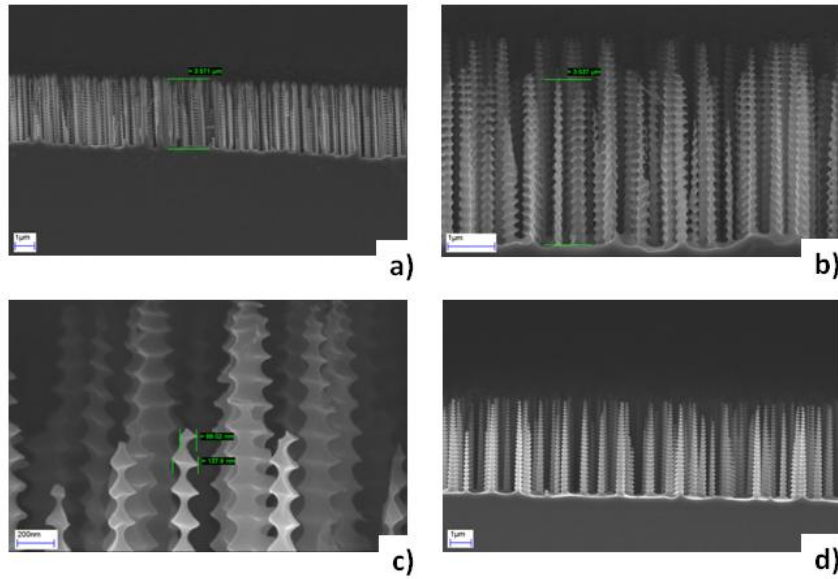


Figure 2.1-8 SEM cross section views of Si grass samples.

The nanostructures present also the typical need-like shape with scalloped profile. The base section distribution (Figure 2.1-9 b) shows a prominent peak at average section ~ 230 nm, but other minor peaks show themselves, suggesting again of an overlapping of different population. Anyway, an in-depth statistical study of Si grass morphology is beyond and unnecessary to the scope of the present study, then any attempt to correlate statistically the size distributions has not been tried.

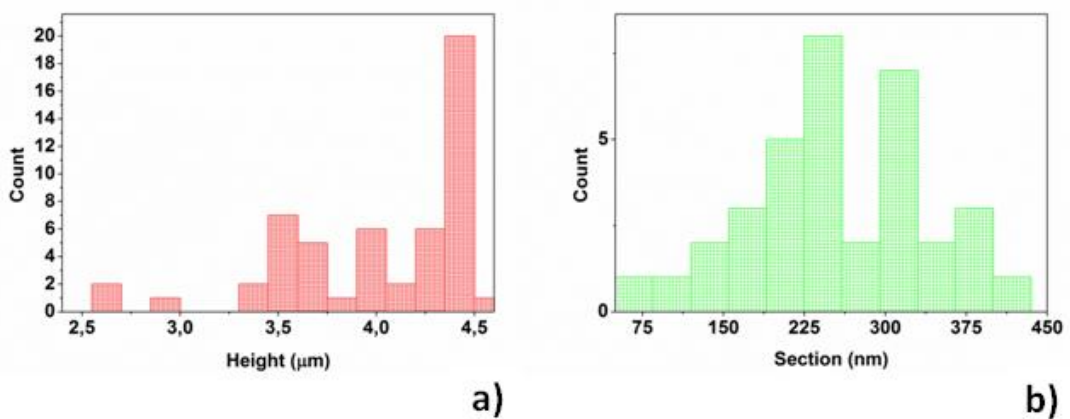


Figure 2.1-9 Si grass NW a) height distribution and b) base section distribution.

2.2 Si Grass-Based SBDs: the Fabrication Process

A survey of the fabrication of Si-grass based SBDs is illustrated in this section. Aside the specific details, this general procedure applies for the realization of similar devices based on a broad variety of semiconductor NW arrays.

2.2.1 NW Array Encapsulation into a Filler Material

The three-dimensional geometry of NW arrays is challenging for the realization of front contacts over them. Among the main technical difficulties the poor interconnection between NW tops and the metal contact, and the necessity to avoid the formation of shunting paths between the front contact and the back contact on the substrate. Both of them may be solved through integration of the NW arrays by means of a filling material [1.17], which while playing the role of inactive, support medium also prevents the occurrence of the above mentioned shunting paths [1.16]. Finally, it allows the deposition of a planar front contact with low sheet resistance on top of the NWs [2.15]. Many filler materials have been attempted to this end, with different results.

- **Spin-On-Glass (SOG).** It is a liquid solution which is spin-coated onto a silicon wafer, in order to fill even submicron gaps in the pre-metal and metal levels while planarizing the surfaces in the fabrication of modern ICs. After drying and curing/sintering, it turns into an interlevel (: something set between metallization levels on Si ICs) Si-O network, dielectric thin film with a performance similar to SiO₂. The use of SOG materials for filling of NW arrays has showed that the embedding process is difficult to achieve for dense arrays of thin NWs [2.16].
- **Chemical Vapor Deposition (CVD) of SiO₂ layer [2.17].** PECVD (plasma-enhanced CVD) or SACVD (sub-atmospheric CVD) silicon dioxides have been employed for NWs encapsulation purposes. They have shown that for depositions thicker than 1 μm the top surface roughness progressively vanishes but some voids are anyway left, particularly in the PECVD oxide layer. This could leads to mechanical failure of the layer as supporting medium especially in case of chemical mechanical polishing step performed prior to the top contact deposition. The final result is delamination. In the case of SACVD oxide the better coating quality is reached with the higher NWs density.
- **Organic polymers.** Various organic materials have been successfully used as fillers for NW arrays: poly(methyl methacrylate) (PMMA) [1.18, 1.19], accuflow T-27 (Honeywell) [2.16] and Cyclotene resin (DOW chemical) [1.16, 2.17]. A systematic comparative study [1.16] between four different transparent, organic polymers as filler materials for NWs encapsulation has

qualitatively analyzed the thermal stability and porosity (results listed in Table 2-1) of each one as embedding medium for NW arrays.




Organic Polymer	Softbaking Temperature (°)	Hardbaking Temperature (°)	Thermal Stability	Porosity
S1808 photoresist (Shipley)	110 for 2 min	130 for 2 min	-	Many, large voids present
SC200 (Silecs)	150 for 5 min	200 for 5 min	Delaminates under anneal	
SU8-2 photoresist (Microchem)	95 for 4 min	200 for 5 min	Cracks under anneal; stable if under contact.	
Cyclotene 3022-35 (DOW Chemical)	100 for 1.5 min	250 for 30 min		Few, small voids present

Table 2-1 – List of post-spincoating temperature treatments details (softbaking and hardbaking) and mechanical stability filling media for four different organic polymer. [1.16]

SU8 2002 Photoresist as Filler for Si Grass-Based SBDs

Upon consideration over previous results from literature, a brief survey of whom has been given above, the SU8 2002 photoresist has been deemed the most suitable choice as encapsulating material for the Si Grass samples. SU-8 is an epoxy-based negative photoresist, a very viscous polymer, that can be spun or spread over a thickness ranging from below 1 μm up to above 300 μm . It can be used to pattern high aspect ratio (> 20) structures. The reasons which have prompted its choice are listed below:

1. it is of common use in clean room operations, then it is cheap and easily attainable;
2. for the reverse of the above argument, SOG and CVD silicon dioxides have been ruled out; especially CVD needs the use of dedicated and costly machines, and there could also be issues related to mechanical weakness of the deposited filler layer [2.17];
3. among organic polymers it has showed good thermal stability under anneal after metal contact deposition, and good filling coverage [1.16];
4. it requires the lower softbaking temperature (see Table 2-1).

Points 1. and 2. are important in view of transferring the operative procedure for NW array-based SBDs outside the laboratory to industrial manufacturing. Easy and cheap processes are in fact highly searched for mass fabrication, because they lead to satisfactory economic yielding. Points 3. and 4. are instead related to the

successive DLTS characterization scheduled for the complete devices. DLTS measurements, as it will be illustrated better in Chapter 4, need a run in temperature, usually from 80 K (or lower) to 300 K (or even higher). Then thermal stability of the samples is a mandatory requirement for the performing of the DLTS characterization. It has not been possible to determine beforehand from literature the stability of SU8 to low temperatures, given that usually it is used from about 273 K to about 373 K. Finally, since that the solubility of contaminants in solids is enhanced with temperature, for DLTS probing of defect levels of as-processed Si Grass is necessary to avoid high temperature treatments preliminary to DLTS measurements.

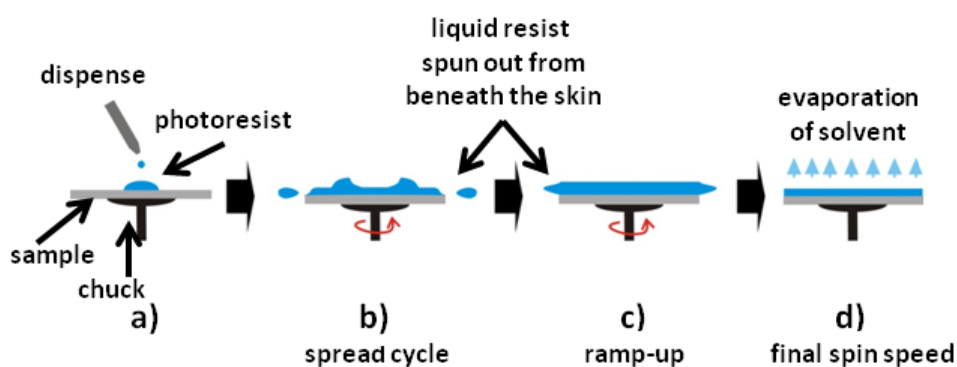


Figure 2.2-1 Scheme of spin coating of photoresist over Si Grass sample.

Si Grass NWs Encapsulation: Procedure Recipe

1. Deposition of of SU8 2002 onto the NW arrays by means of a syringe.
2. In order to minimize voids formation in the subsequent thin film SU8 2002 has been allowed to sit for 5 minutes to seep to the bottom of the NWs.
3. Dehydration treatment for 30 min at 110°C.
4. Spincoating SU-8 2002: 2000 round per minute for 30sec (Figure 2.2-1).
5. Soft-baking treatment: ascending ramp 30 °C → 95 °C (5 °C/min), 1 minute pause, descending ramp 95 °C → 30 °C (5 °C/min).
6. 10s of Near-UV (400 nm) lamp exposition (dose about 110 mJ/cm²).
7. Hard-baking treatment: ascending ramp 30 °C → 95 °C (5 °C/min), 2 minute pause, descending ramp 95 °C → 30 °C (5 °C/min).

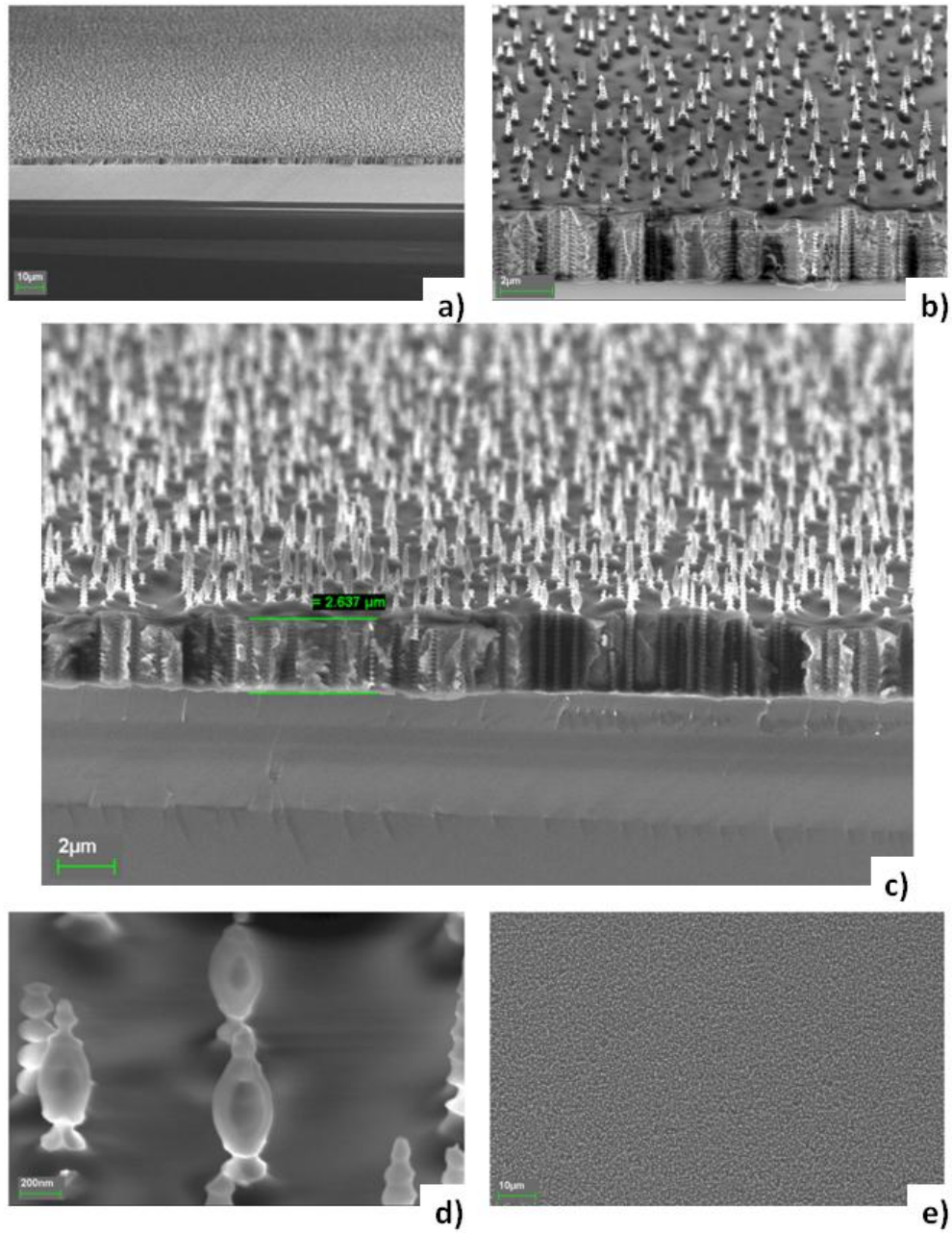


Figure 2.2-2 Si grass NW array sample after the filling step. a) Lower and b) higher magnification tilted view of the embedded NW array. c) Determination of the thickness of the filler layer. d) High magnification of details of the Si grass NWs tops above the filler surface; unwonted residuals of the filler material appears to cover them. e) SEM plane view of the embedded NW array; the filling of the sample appears to be complete. No observations of regions that are depleted of the filler due to bubbles formation during the deposition step.

2.2.2 Contact Deposition Over the Encapsulated NW Array

In Figure 2.2-2 the result of the SU8 2002 filling step over a representative Si Grass sample is showed. The salient features are that the Si Grass tops are covered with remnants of SU8 2002 (Figure 2.2-2 d), and that the filler coverage appears to be faultless (Figure 2.2-2 e).

In order to expose the NW tips for allowing subsequent metal deposition of front contact the samples have been RIE processed for 2 minutes with an O₂ flow rate. The result may be seen in Figure 2.2-3 for the same sample of Figure 2.2-2. The O₂ plasma treatment appears to have successfully

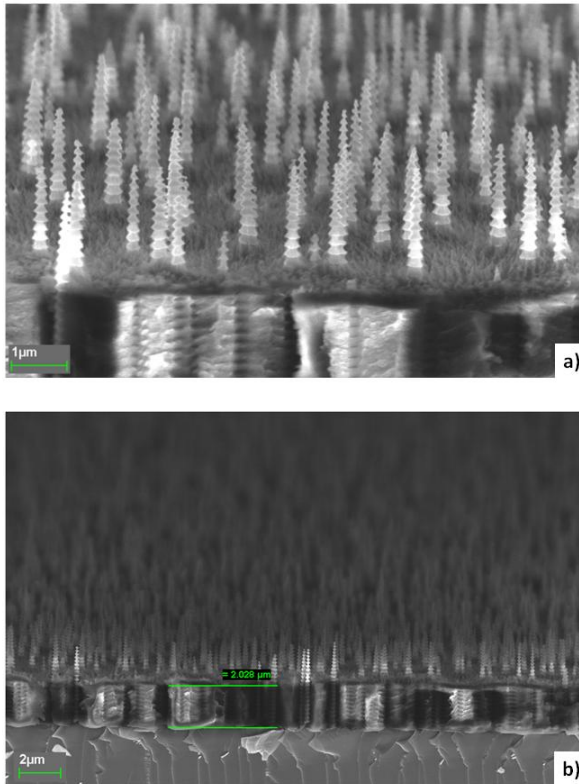


Figure 2.2-3 a), b) Results of RIE etching of SU8 for exposition of NW tips.

removed the unwanted excess of polymer, leading to a reduction in the thickness of the SU8 layer from about 2.6 μm (Figure 2.2-2 c) to about 2 μm (Figure 2.2-3 b).

Finally, after dipping the samples in 5% HF for 10 s to obtain oxide-free NW tips, metal contacts have been evaporated over the top surface of the samples, while ohmic, gallium-painted contacts on the back-substrates have been realized.

BIBLIOGRAPHY

- [2.1] S. Franssila, *Introduction to Microfabrication, Second Edition*, John Wiley & Sons 2010.
- [2.2] M. D. Henry, *ICP Etching for Silicon for Micro and Nanoscale Devices*, PhD Thesis, Caltech 2010.
- [2.3] H.M. Anderson, J.A. Merson, R.W. Light, *IEEE Transactions on Plasma Science*, 1986, PS-14, 2, 156-64.
- [2.4] R. Ghodssi, P. Lin (Eds), *MEMS Materials and Processes Handbook*, Springer 2011.
- [2.5] M. A. Blauw, *Deep anisotropic dry etching of silicon microstructures by high-density plasmas*, PhD Thesis, Delft University of Technology 2004
- [2.6] S. Tachi, K. Kazunori, S. Okudaira, *Applied Physics Letters*, 1988, **52**, 616-618.
- [2.7] J. M. de Boer, J. G. E. Gardeniers, H. V. Jansen, E. Smulders, M-J. Gilde, G. Roelofs, J. N. Sasserath, M. Elwenspoek, *Journal of Microelectromechanical Systems*, 2002, **11**, 385-401.
- [2.8] F. Lärmer, A. Schilp, *Method for Anisotropically Etching Silicon*, German Patent DE-4241045 (1994), US-Patent 5, 501, 893 (1996).
- [2.9] R. Dussart, M. Boufnichel, G. Marcos, P. Lefauchaux, A. Basillais, R. Benoit, T. Tillocher, X. Mellhaoui, H. Estrade-Szwarczopf, P. Ranson, *Journal of Micromechanics and Microengineering*, 2004, **14**, 2, 190-196.
- [2.10] I. W. Rangelow, P. Thoren, K. Masseli, R. Kassing, M. Engelhardt, *Microelectronic Engineering*, 1986, 5, 1-4, 387-394.
- [2.11] G.S. Oerlein, R.G.Schad and M.A. Jaso, *Surface and Interface Analysis*, 1986, **8**, 243.
- [2.12] H. Jansen, M. de Boer, R. Legtenberg, M. Ewenspock, *Journal of Micromechanical Microengineering*, 1995, **5**, 115.
- [2.13] G.S. Oerlein, J.F. Rembetski and E.H. Payne, *Journal of Vacuum Science and Technology. B*, 1990, **8**, 1199.
- [2.14] T. Hayakawa, T. Suzuki, T. Uesugi, Y. Mitsushima, *Japanese Journal of Applied Physics*, 1998, Part 1, **37**, 1, 5.
- [2.15] S. Perraud, S. Poncet, S. Noël, M. Levis, P. Faucherand, E. Rouvière, P. Thony, C. Jaussaud, R. Delsol, *Solar Energy Materials and Solar Cells*, 2009, **93**, 1568.
- [2.16] E. Latu-Romain, P. Gilet, P. Noel, J. Garcia, P. Ferret, M. Rosina, G. Feuillet, F. Lévy, A. Chelnokov, *Nanotechnology*, 2008, **19**, 345304.

[2.17] Goto H, Nosaki K, Tomioka K, Hara S, Hiruma K, Motohisa J and Fukui T
Applied Physics Express, 2009, **2**, 035004.

CHAPTER 3

Current Transport in Si Grass-Based SBDs

3. 1 The Schottky Barrier Formation

3.1.1 The Work Function of a Solid

The work function of a metal ϕ_M is the amount of energy required to promote an electron inside the metal from the Fermi Energy level to a state of rest outside the metal surface (: the vacuum level). The quantum mechanical computation of the work function shows that it consists of a volume contribution, which is the energy of an electron due to the periodic potential of the crystal and the interaction of the electron with other electrons, and a surface contribution, in case of existence of a dipole layer at the surface [3.1]. In fact, for the atoms belonging to the metal surface the electron charge is not anymore symmetrically distributed around the nucleus, these displacement between the centres of positive and negative charge resulting in a dipole layer. If the dipole layer has an electric dipole moment ρ per unit area, this will give rise to an electrostatic potential difference $\frac{\rho}{\epsilon_0}$ between vacuum and the metal interior. The correspondent change in energy $q \frac{\rho}{\epsilon_0}$ of an electron constitutes part of the work function. Any change in the surface electron charge distribution will lead to change in ϕ_M through a change in the dipole layer.

In analogy to the above definition, the work function of a semiconductor ϕ_S is the difference in energy between the Fermi level and the vacuum level. It is again composed of a bulk and a surface contribution.

3.1.2 Ideal Schottky Barrier: the Schottky-Mott Theory

Let us suppose a metal and an n-type semiconductor ($\phi_M > \phi_S$), to be electrically neutral and at the beginning separated by a gap δ from each other. In the ideal case no surface states are present. By connecting the metal and semiconductor through a wire, electrons are allowed to flow from the semiconductor into the metal until the

two Fermi levels E_F^S, E_F^M align themselves. Within the metal-semiconductor gap arises an electric field \mathcal{E}_i , due to negative charge accumulation on the metal surface because of the extra conduction electrons contained within the Thomas-Fermi screening distance, balanced by a positive charge in the semiconductor. Being the semiconductor n-type by premises, this positive charge will be provided by uncompensated positively charged donor ions contained in a near-surface region depleted by electrons (: depletion region). Since the donor impurity concentration is largely less than the metal electron density, then the layer thickness W of the depletion region is not negligible. $V_i = \delta\mathcal{E}_i$ is the difference in electrostatic potentials outside the surfaces of the metal and semiconductor. Letting $\delta \rightarrow 0 \Rightarrow V_i \rightarrow 0$ (if \mathcal{E}_i is to remain finite) and the Schottky Barrier Height (SBH) ϕ_b is given by the Schottky-Mott limit expression:

$$\phi_b = \phi_M - \chi_S \quad (3.1)$$

χ_S being the semiconductor electron affinity. Equation (3.1) is a first-order approximation for the SBH, rarely experimentally observed. In real Schottky contacts commonly there is a thin oxide insulating layer which electrons have to tunnel through, then the SBH is not as strongly dependent on ϕ_M . Furthermore, the Schottky-Mott limit also assumes:

- no change in the surface dipole contributions to ϕ_M and ϕ_S when the metal and semiconductor are brought into contact;
- no localized states on the surface of the semiconductor;
- the metal-semiconductor is an abrupt junction, with no intermixing of the two materials and no defects at the interface.

The band bending depends on the voltage drop across the junction, and in this simplified model is:

$$qV_b = \phi_M - \phi_S \quad (3.2)$$

equal to the contact potential difference between the metal and the interior of the semiconductor. V_b is termed the built-in voltage. It holds that

$$\phi_b = qV_b + E_C - E_F \quad (3.3)$$

since

$$\phi_S - \chi_S = E_C - E_F \quad (3.4)$$

For a p-type semiconductor Equation (3.1) is substituted by:

$$\phi_b = \phi_M - \chi_S - E_G \quad (3.5)$$

being E_G the semiconductor bandgap, while equation (3.2) is still valid.

Within the semiconductor the potential obeys the Poisson's equation. The boundary conditions are constituted by the definite energy relationship between the conduction and valence bands E_C , E_V and the Fermi level in the metal established once the metal-semiconductor junction is formed. Under the abrupt approximation that the bulk concentration of ionized impurities within the surface space charge region is $\rho \sim qN_D$ for $x < W$, and $\rho \sim 0$, $\epsilon \sim 0$ for $x > W$, the depletion layer width is:

$$W = \sqrt{\frac{2\epsilon_S(V_b - V)}{qN_D}} \quad (3.6)$$

Thus, the abrupt metal-semiconductor junction contains a parabolic band-bending region.

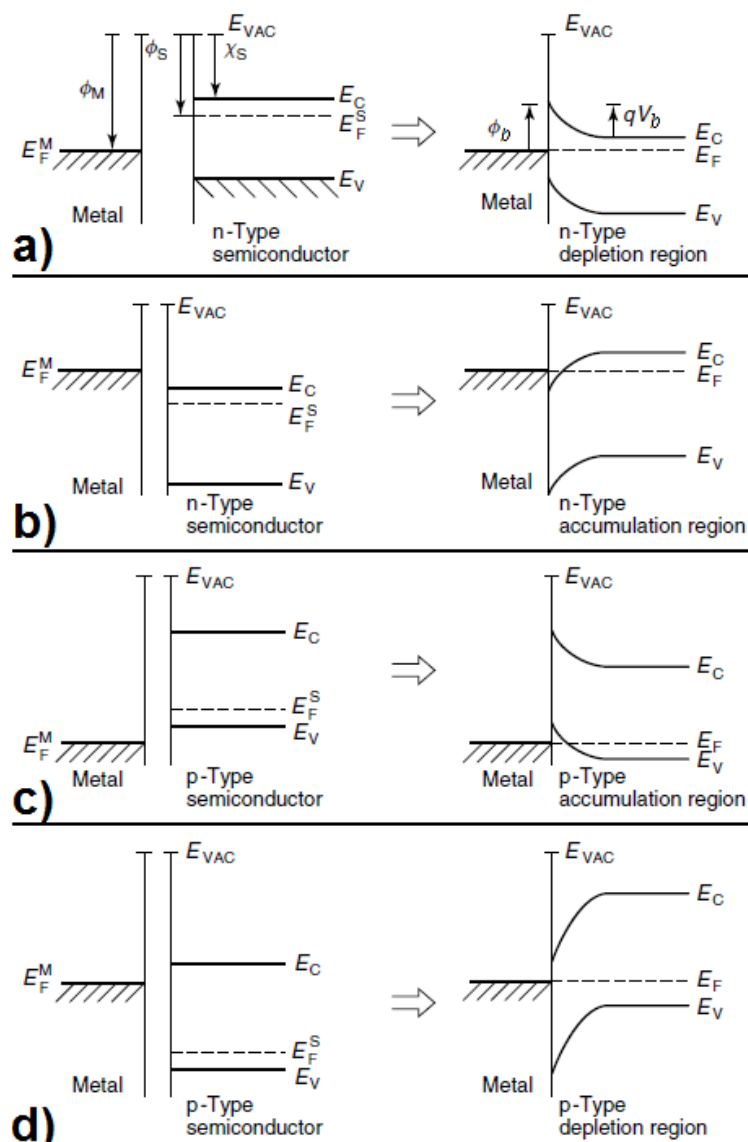
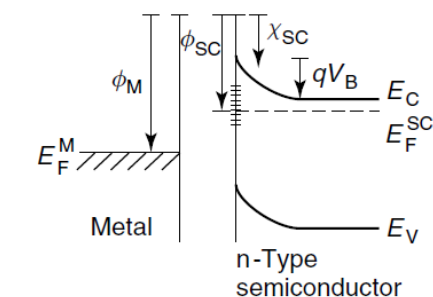


Figure 3.1-1 Band bending diagram before and after metal-semiconductor contact for a) metal and n-type semiconductor, $\phi_M > \phi_S$ b) metal and n-type semiconductor, $\phi_M < \phi_S$ c) metal and p-type semiconductor, $\phi_M > \phi_S$ and d) metal and p-type semiconductor, $\phi_M < \phi_S$. After L. J. Brillson, *Surfaces and Interfaces of Electronic Materials*, WILEY-VCH Verlag GmbH & Co. KGaA, Weinheim, 2010.

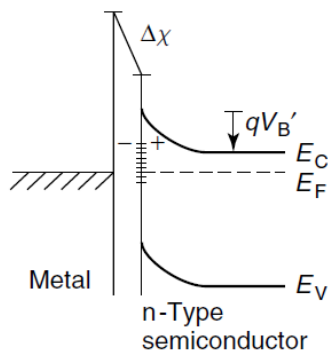
Forward and Reverse Bias

A voltage applied to the metal-semiconductor junction will fall mostly across its surface space charge region. If the metal-semiconductor junction is forward biased, ϕ_S is lifted relative to ϕ_M thus reducing the barrier height ϕ_b and narrowing the depletion width W . Correspondingly, the current flow increases. If the metal-semiconductor junction is reverse biased, ϕ_S drops increasing the SBH, and therefore the binding energy of the electrons increases. This means that the electron requires more energy to overcome the SBH. The consequence is that less current flows.

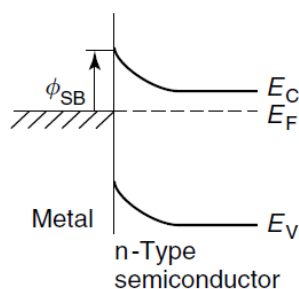
3.1.3 Real Schottky Barriers



a) Before contact



b) After contact



c) Abrupt interface

The ideal picture of Schottky barrier formation expressed by Equation (3.1) - (3.3) does not agree in many cases with experimental measurements of metal–semiconductor interfaces. Typically, for the same semiconductor the correlation between $\phi_M - \phi_S$ and the SBH is weak. According to Bardeen's work [3.4] that means that localized states at the interface can accumulate charge and generate dipoles that take up much of the metal–semiconductor potential difference.

In case of semiconductor with surface states, the band bending is present even before the junction formation with a metal. In the case depicted in Figure 3.1-2 a), this is due to negative charge that fills states localized at or near the surface at energies below the E_F^S .

Figure 3.1-2 Band bending diagram a) before and after b) metal–semiconductor junction formation in case of a high density of surface states; c) band diagram after contact in the ideal case. After L. J. Brillson, *Surfaces and Interfaces of Electronic Materials*, WILEY-VCH Verlag GmbH & Co. KGaA, Weinheim, 2010.

For relatively high density of surface states (10^{14} cm^{-2}) small variations of the Fermi level E_F^S within this energy range of states produce large changes of localized state occupation. Consequently, most of the contact potential difference $\phi_M - \phi_S$ falls across an atomically thin interface dipole region instead of the semiconductor space charge region (Figure 3.1-2 b). The voltage drop $\Delta\chi$ across this dipole depends on the density of electron filled localized states as well as the dielectric constant of the layer across which this voltage drops. Equation (3.3) is then substituted by

$$\phi_b = \phi_M - \chi_S - \Delta\chi \quad (3.7)$$

ϕ_b and qV_b are then relatively independent from ϕ_M , the Fermi level resulting **pinned** by surface states within a narrow range of energy in the semiconductor bandgap. If the dipole layer is so thin such that charge tunnel across it, then the dipole does not affect the metal-semiconductor junction (Figure 3.1-2 c).

3.2 Current Transport in Schottky Junctions

The current transport in metal-semiconductor contacts is mainly due to majority carriers. The five basic transport processes [3.4] in these devices under forward bias are depicted in Figure 2.3-2.

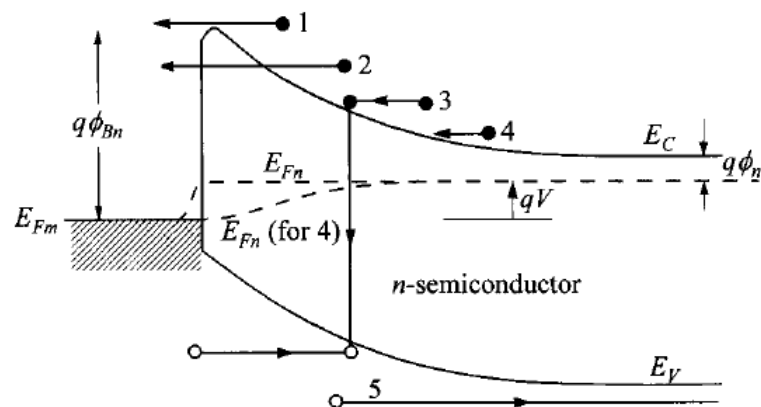


Figure 3.2-1 Basic transport processes in forward biased Schottky junction. 1) Thermionic emission. 2) Tunneling. 3) Recombination. 4) Diffusion of Electrons. 5) Diffusion of Holes. After S. M. Sze, *Physics of semiconductor devices*, Wiley, 1981.

3.2.1 Thermionic Emission Model

Thermionic emission is the rate limiting process of electron emission over the barrier for high temperature, non-degenerate semiconductor, under the assumption that the Schottky barrier be homogeneous (: loosely speaking, when its SBH varies on a lateral length scale much longer than the depletion region width). The current dependence on voltage follows the law:

$$J = J_S \left[\exp\left(\frac{qV}{k_B T}\right) - 1 \right] \quad (3.8)$$

$$J_S \equiv A^* T^2 \exp\left(-\frac{\phi_b}{k_B T}\right) \quad (3.9)$$

set that J is the diode current density, J_S is the diode saturation current density, $A^* \equiv \frac{4\pi e m^* k_B^2}{h^3}$ is the effective Richardson constant for thermionic emission, q is the electron charge, m^* is the semiconductor effective mass, k_B is the Boltzmann constant, h is the Planck constant, T is the temperature, ϕ_b is the SBH, V is the forward bias across the junction.

The expression for the Richardson constant given above holds if the semiconductor's conduction band has spherical constant energy surfaces, otherwise the m^* must be substitute accordingly.

Image Force Lowering of the Barrier

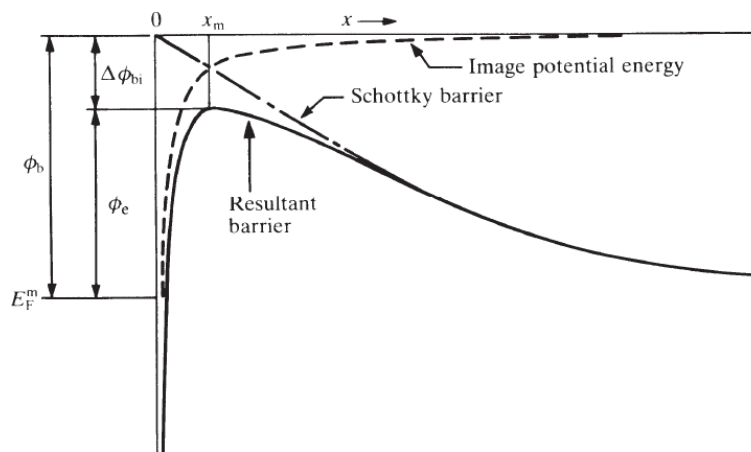


figure 3.2-2 Image force lowering of a Schottky barrier. After E. H. Roderick, R. H. Williams, *Metal-Semiconductor Contacts, Second Edition*. Oxford, Clarendon Press, 1988.

Let us assume no interfacial layer be present at the metal-semiconductor junction. If an electron $-q$ is located at distance x from the surface of the metal it experiences an attractive force

$$F = \frac{q^2}{4\pi\epsilon'_s(2x)^2} \quad (3.10)$$

where the requirement that the electric field must be perpendicular to the surface enables it to be calculated as due to a positive charge $+q$ located at the mirror-image of the electron with respect to the metal surface. ϵ'_s is the high frequency

semiconductor permittivity. The image potential energy (relative to this attractive force) is

$$U(x) = -\frac{q^2}{16\pi\epsilon'_S x} \quad (3.11)$$

set that $U(+\infty) = 0$.

The image potential energy has to be added to the potential energy due to the Schottky barrier (Figure 3.2-2). A good approximation is to consider the field due to the Schottky barrier of constant value \mathcal{E}_{max} , because the image potential is important only near the surface. The total potential energy will be

$$U_{tot} = -\frac{q^2}{16\pi\epsilon'_S x} + qx\mathcal{E}_{max} \quad (3.12)$$

which will reach the maximum at x_m such that

$$\frac{\partial U_{tot}}{\partial x} \Big|_{x_m} = 0 \Leftrightarrow \frac{q}{16\pi\epsilon'_S x_m} = x_m \mathcal{E}_{max} \Leftrightarrow x_m = \sqrt{\frac{q}{16\pi\epsilon'_S \mathcal{E}_{max}}} \quad (3.13)$$

The overall Schottky barrier lowering effect $\Delta\phi_{bi}$ at the maximum barrier height position x_m (Figure 3.2-2) as a result of the image force is:

$$\Delta\phi_{bi} = -\frac{q^2}{16\pi\epsilon'_S x_m} + qx_m \mathcal{E}_{max} = 2qx_m \mathcal{E}_{max} = q \sqrt{\frac{q\mathcal{E}_{max}}{4\pi\epsilon'_S}} \quad (3.14)$$

Let us define the **depletion approximation**:

- the electron density in the conduction band falls abruptly from its bulk value N_D to a negligible value within the depletion region \Leftrightarrow the charge density rises abruptly from zero to the value qN_D at the edge of the depletion region.

If N_D is constant, then the electric-field strength will increase linearly from the edge of the depletion region according to Gauss's theorem, and it will reach the maximum value at the metal-semiconductor interface $\mathcal{E}_{max} = \frac{qN_D W}{\epsilon_S}$. The average field strength being $\frac{\mathcal{E}_{max}}{2} \Leftrightarrow V_d \equiv \frac{\mathcal{E}_{max} W}{2} = \frac{\epsilon_S \mathcal{E}_{max}^2}{2qN_D}$ is the potential drop across the depletion region (: **diffusion potential**), so that:

$$\mathcal{E}_{max} = \sqrt{\frac{2qN_D V_d}{\epsilon_S}} \quad (3.15)$$

If instead of assuming an abrupt rising of the charge density at the edge of the depletion region this latter is supposed to increase gradually through a transition region, then Equation (3.15) becomes:

$$\varepsilon_{max} = \sqrt{\frac{2qN_D}{\varepsilon_S} \left(V_d - \frac{k_B T}{q} \right)} \quad (3.16)$$

By substituting Equation (3.16) into Equation (3.14), the expression for the barrier lowering due to the image force is finally determined to be

$$\Delta\phi_{bi} = q \left[\frac{q^3 N_D}{8\pi^2 \varepsilon_S^3 x_m} \left(\phi_b - E_C + E_F - V - \frac{k_B T}{q} \right) \right]^{1/4} \quad (3.17)$$

set that the potential drop across the depletion region may be rewritten as

$$V_d \equiv V_b - V = \phi_b - E_C + E_F - V, E_C + E_F = -\ln \left(\frac{N_D}{N_C} \right) \frac{k_B T}{q} \quad (3.18)$$

$N_C \equiv 2 \left(\frac{2\pi m^* k_B T}{h^2} \right)^{3/2}$ being the effective density of states in conduction band.

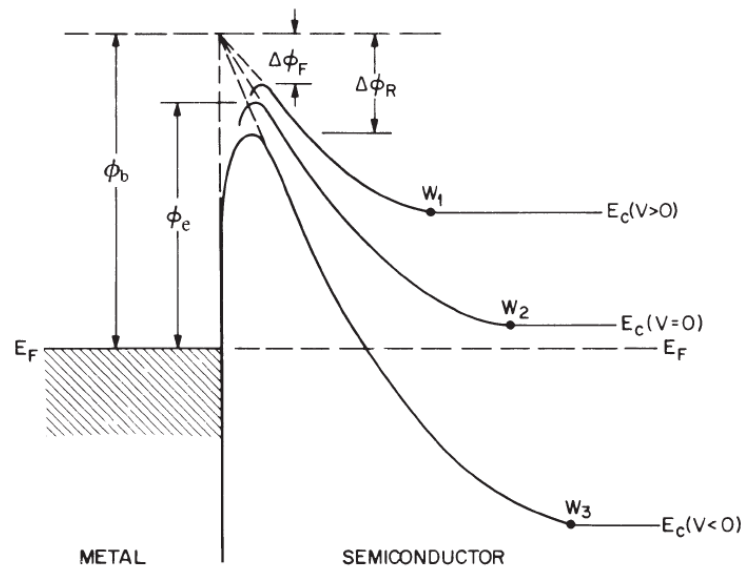


Figure 3.2-3 Image force lowering of a Schottky barrier under forward ($\Delta\phi_F$) and reverse ($\Delta\phi_R$) bias. After S. M. Sze, *Physics of semiconductor devices*, Wiley, 1981.

Effect of the Image Force Lowering of the Barrier Over the Thermionic Emission Model

The thermionic emission current-voltage relationship is expressed by Equation (3.9) provided that the SBH is bias independent. But even in a perfect contact with no interfacial layer, the SBH is lowered by an amount $\Delta\phi_{bi}$ as a result of image-force, so that $\phi_e \equiv \phi_b - \Delta\phi_{bi}$ is the effective barrier which electrons must surmount to be injected into the metal. Being $\Delta\phi_{bi}$ bias dependent, then also ϕ_e is bias dependent, even when ϕ_b is not.

Let us assume to be constant the gradient of the effective barrier with applied voltage, $\frac{\partial\phi_e}{\partial qV} \equiv \beta$, then the effective barrier can be rewritten as

$$\phi_{bEff} \equiv \phi_b|_0 - \Delta\phi_{bi}|_0 + \beta qV \quad (3.19)$$

$\phi_b|_0$, $\Delta\phi_{bi}|_0$ referring to SBH and image force barrier lowering at zero bias. By substituting $\phi_b \rightarrow \phi_e$ in Equation (3.8) this latter becomes

$$J = A^*T^2 \exp\left(-\frac{\phi_b|_0 - \Delta\phi_{bi}|_0 + \beta qV}{k_B T}\right) \left[\exp\left(\frac{qV}{k_B T}\right) - 1\right] \quad (3.20)$$

which can be rewritten as

$$J = J_S \exp\left(\frac{qV}{nk_B T}\right) \left[1 - \exp\left(-\frac{qV}{k_B T}\right)\right] \quad (3.21)$$

$$J_S \equiv A^*T^2 \exp\left(-\frac{\phi_{bEff}}{k_B T}\right) \quad (3.22)$$

set that $\beta \equiv 1 - \frac{1}{n}$, n is the **ideality factor**. Let us observe that there are also other mechanism which leads to a current-voltage relationship of the kind of that expressed by Equation (3.21). Equation (3.21) is frequently written as

$$J = J_S \left[\exp\left(\frac{qV}{nk_B T}\right) - 1\right] \quad (3.23)$$

which is incorrect, but the difference between it and Equation (3.22) is negligible for $V > 3 \frac{k_B T}{q}$.

By taking into account the effect of series resistance R_S , Equation (3.21) becomes:

$$J = J_S \exp\left(\frac{q(V - IR_S)}{nk_B T}\right) \left[1 - \exp\left(-\frac{qV}{k_B T}\right)\right] \quad (3.24)$$

Ideality Factor

From Equation (3.21) it follows that the ideality factor may be experimentally determined by plotting $\ln \left(\frac{J}{[1 - \exp(-\frac{qV}{k_B T})]} \right)$ against V , which would result in a straight line of slope $\frac{q}{nk_B T}$ if n were constant even for $V < 3 \frac{k_B T}{q}$ and for reverse bias [3.5], that is

$$\frac{1}{n} = \frac{k_B T}{q} \frac{d}{dV} \ln \left(\frac{J}{[1 - \exp(-\frac{qV}{k_B T})]} \right) \quad (3.25)$$

and which becomes the more commonly found in literature

$$\frac{1}{n} = \frac{k_B T}{q} \frac{d \ln J}{dV} \quad (3.26)$$

but only if $V > 3 \frac{k_B T}{q}$.

Often $\frac{\partial \phi_e}{\partial qV}$ is not constant, then the plot of $\ln \frac{J}{[1 - \exp(-\frac{qV}{k_B T})]}$ against V is not linear, that is n is bias dependent. Then n is a dimensionless quantity which parameterize show the diode deviates from an ideal thermionic barrier. To be confident the current across a barrier is determined by thermionic emission theory, a value of $n < 1.1$ is required. If it is greater than this then another transport mechanism is allowing electrons to pass over the SB.

3.2.2 Tunneling Current

Carriers with energies lower than the SBH may still quantum tunnelling through it. The tunnelling current is more likely to become significant in heavily doped semiconductors, due to the narrowing of the depletion region, and at low temperatures. In forward bias, at room temperature and on a non degenerate semiconductor, the narrowing of the width of the depletion region is insufficient before the electrons have enough energy to overcome the barrier thermally. Tunnelling is, instead, more often apparent in reverse bias as a departure from ideal thermionic emission behavior.

3.2.3 The Richardson Plot of the Saturation Current

At low currents under forward bias, when the effects of series resistance can be neglected, Equation (3.21) may be written as

$$\ln\left(\frac{I}{\left[1 - \exp\left(-\frac{qV}{k_B T}\right)\right]}\right) = \frac{qV}{k_B T} + \ln(I_S) \quad (3.27)$$

Then the saturation current I_S may be extracted by current–voltage–temperature characteristics. The so called **Richardson Plot** is obtained by plotting $\ln\left(\frac{I_S}{A^* T^2}\right)$ versus $\frac{1}{T}$, according to the relationship determined from Equation (3.22):

$$\ln\left(\frac{I_S}{A^* T^2}\right) \equiv -\frac{\phi_{bEff}}{k_B} \cdot \frac{1}{T} + \ln(A^*) \quad (3.28)$$

By linear fitting the Richardson Plot is thus possible to determine the effective SBH ϕ_{bEff} and the Richardson constant A^* . Actually, the parameter ϕ_{bEff} may be determined directly by the saturation current as

$$\phi_{bEff} \equiv k_B T \ln\left(\frac{A A^* T^2}{I_S}\right) \quad (3.29)$$

3.3 Si Grass-Based SBDs: the Electrical Characterization

As already briefly examined in Chapter 1, the properties of metal-semiconductor NWs junctions are a topic of major interest in view of developing NWs-based devices. With this aim the fabricated Si Grass-based SBDs have been electrically characterized by means of current-voltage (I-V) measurements (Figure 3.3-1 d). Their realization procedure has been illustrated in Chapter 2, and a survey is showed in Figure 3.3-1 a) - c). In fact, as discussed in Sections 3.1 – 3.2 for bulk SBDs, a significant amount of physical information may be extracted from the I-V characteristics of these devices.

In Figure 3.3-2 is displayed a representative $\ln(I)$ -V plot of the Si Grass-based SBDs. The region of linear behavior corresponds to the low bias interval 0.1 – 0.5 V. The ideality factor has been extracted by applying Equation (3.26). The determined value is of 2.8. This value is far away from the expected value of about 1 for an ideal SBD, indicating that non-ideal factors affect the current transport.

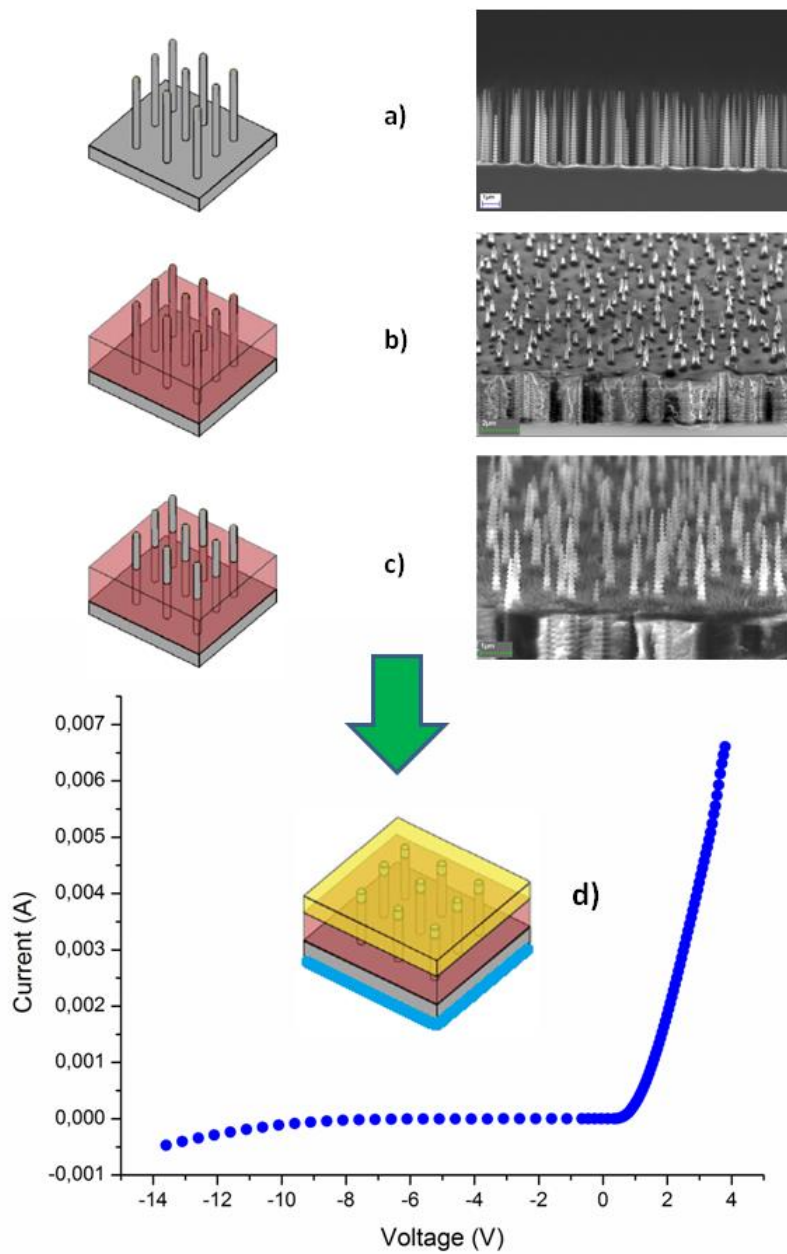


Figure 3.3-1 Schematic of the fabrication process of Si Grass-based Schottky diodes. a) As grown NW array. b) Filling step for NW integration with inactive layer. c) Dry etching step for cleaning of NW tips from unwonted residuals of filling step. d) Deposition of Schottky contact and of backside Ohmic contact; typical current-voltage characteristics of the realized devices is shown.

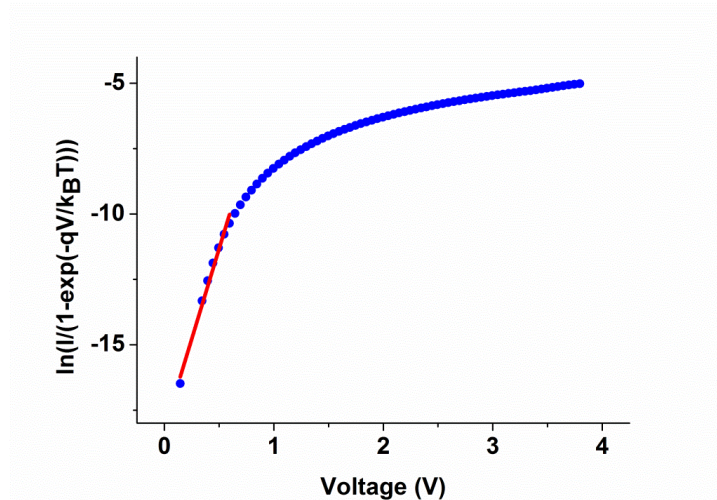


Figure 3.3-2 RT forward $\ln(I)$ -V of Si Grass-based SBDs. The red line corresponds to the linear region.

3.3.1 Review of Results of Current Transport Models in NW-Based SBDs

The behavior of nanoscale contacts on bulk semiconductors or NWs may depart significantly from that of their microscale counterparts.

Nano-Schottky Junctions

For nanoscale contacts to a bulk semiconductor, the solution of the Poisson equation predicts barrier width thinning and an increase in tunneling current is experimentally observed [3.6, 3.7]. Also a reduction of the Fermi-level pinning at the metal-semiconductor interface compared to bulk Schottky contacts [3.8].

Single Semiconductor NW-Based SBDs

Experimental current-voltage characteristics of single semiconductor (Si, ZnO and GaN) NW-based SBDs show deviation from the conventional thermionic emission theory [3.9 - 3.11]. A tunneling current contribution has been suggested to be the source of it. In addition, the Schottky barrier depletion width can be influenced by surface charge present along the adjacent surface of the nanowire [3.12]. For all these reasons, the Schottky barrier height extracted from the current-voltage (I-V) characteristics might be significantly different from the actual barrier height.

Array NW-based SBDs

Various NW array-based SBDs have been realized, their design concepts in many cases pretty similar to the one which has been adopted for the fabrication of the Si Grass-based SBDs. Anyway they have been rarely studied as regards the characterization of their electrical properties. Metal assisted wet Chemical Etched (MaCE) p-Si NWs [3.13] have been employed to fabricate PtSi SBDs [3.14, 1.20]. In

[3.14] the metal contact has been deposited directly upon the NWs, while in [1.20] previously to front electrode fabrication the as-grown NWs has been encapsulated in a filler material (Figure I-2 a1) – a8). Their electronic properties have been investigated using current–voltage–temperature (I–V–T) characteristics in the range 300-370 K. For all the experimental temperatures, the Pt/p-Si NWs Schottky diodes exhibited Schottky rectifying behavior. Room temperature (RT) I-V characteristics have been analyzed using the thermionic emission model. The correspondingly values of the ideality factor (Equation 3.26) and zero-bias barrier height (Equation 3.9) have been extracted (see Table 3-I).

Reference	Ideality Factor n	Zero-Bias Barrier Height $\phi_{b 0}$ (eV)	Voltage Range of Linear Behavior in LogI-V Plot
[3.14]	2.426	0.242	-
[1.20]	4.62	0.519	0.1-0.5 V

Table 3-I – Electrical parameters of the PtSi/p-SiNWs SBDs.

In [3.14] the Thermionic Emission model has been found to explain satisfactorily the experimental data, while in [1.20] defect-assisted tunneling has been deemed to better interpret the I-Vs characteristics.

SBDs have been fabricated [1.19, 3.15] starting from ZnO nanorods grown vertically aligned on n-SiC substrates. The device architecture is illustrated in Figure I-2 c1) – c2). The RT Current-Voltage curves have been analyzed in the framework standard thermionic emission theory [1.19]. The high value of the extracted ideality factor (2.4; 0.2-0.5 V the voltage range of linear behavior in LogI-V plot) has been related to the existence of interfacial layers or surface states, and also considered indicative that the transport mechanism is no longer dominated by thermionic emission. At higher bias the power law regime $I \propto V^2$ has been identified as operating, related to the space-charge limited current (SCLC) transport mechanism.

3.3.2 Alternative Current Transport Models for SBDs

The extracted value of 2.8 for the ideality factor of the Si Grass-based SBDs is then in line with the reported RT ideality factors of Si NWs-based SBDs ([3.14], [1.20]), as Subsection 3.3.1 has very briefly discussed. The departure from the thermionic emission model is even more evident at high bias ($V \geq 2$) (Figure 3.3-2). This could be due to the presence of high series resistance R_s , or mean that other mechanisms than the thermionic emission model originate the current transport. In the following the main features of all the possible alternative models will be briefly summarized.

The Parasitic Effects

A number of parasitic effects may occur in diodes, such as shunts, series resistances, and parasitic diodes. The inspection of the diode I - V characteristic allows for diagnosing and identifying these problems. In Table 3.II they are listed, together with their effects over the I - V curve. In particular, in a diode with series resistance (second record of Table 3.II) at high forward bias the current no longer increases exponentially with voltage, instead it increases linearly and:

$$R_S = \lim_{I \rightarrow \infty} \frac{\partial V}{\partial I} \quad (3.30)$$


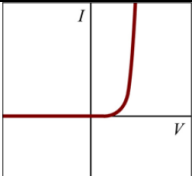
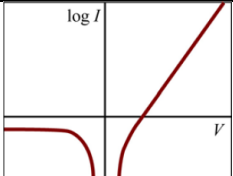

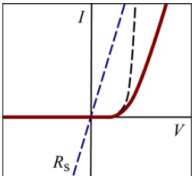
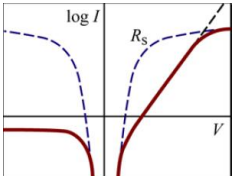
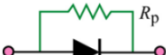
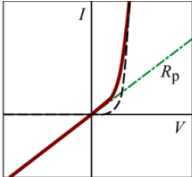
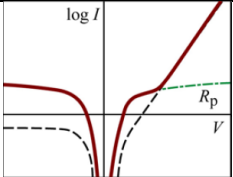
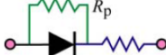
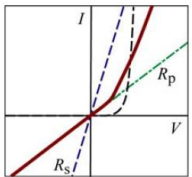
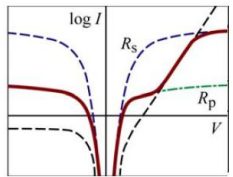
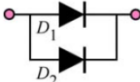
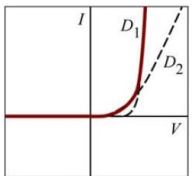
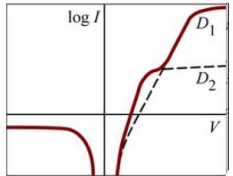
Parasitic Effect	I-V Characteristic: Linear Scale	I-V Characteristic: Log Scale
 <p>None: ideal diode</p>		
 <p>Diode with series resistance: it shows a deviation from the exponential behavior at high forward currents. According to Kirchhoff's voltage law, the voltages across the diode and the resistor add up.</p>		
 <p>Diode with parallel resistance (shunt): according to Kirchhoff's current law, the currents through diode and resistor add up.</p>		 <p>The forward "hump" has about the same level as the reverse saturation current.</p>
 <p>Diode with series and parallel resistance (shunt): Effects of shunt and series resistance found at low and high currents, respectively.</p>		
 <p>Parasitic diode with lower barrier height and smaller area than main diode</p>		 <p>The forward "hump" has much higher level than the reverse saturation current.</p>

Table 3-II Main parasitic effects that may occur in diodes. After E. Fred Schubert, *Light Emitting Diodes, Second Edition*, Cambridge University Press, New York, 2006.

Space Charge Limited Current (SCLC) Transport

The SCL conduction occurs in a material when the rate of the charge-carrier injection is higher than the rate of recombination. Consequently, the injected carriers form a space charge, resulting in an electric field which limits the current flow: the current is “bulk controlled”, which means that is determined by the material’s carriers mobility and affected by the traps in the material bandgap. To achieve bulk-limited electrical conduction the carrier-injecting contact must be ohmic, or anyway its resistance must be smaller than the intrinsic resistance of the material [3.17 – 3.19]. This in order that the contact acts as a reservoir of charge carriers. SCLC behavior has been mainly detected in the $I - V$ curves of simple sandwiched structures, that is metal-insulator-metal or metal-semiconductor-metal [3.17 – 3.19], for instance with amorphous silicon [3.12], and lately with organic semiconductors [3.17]. Sometimes, also more complicated structures have shown SCL current-voltage characteristics, typically $n^+ - i - n^+$, $p^+ - i - p^+$ or $p - i - n$ devices [3.17 – 3.19, 3.21 – 3.23]. In these latter cases the heavily doped regions are the charge injection contacts into the much more resistive intrinsic layer, which plays the role of the bulk controlling the current flow.

To go into the details of this theory is beyond the scope of the present thesis. The interested reader may consult primarily [3.17 – 3.19], that deal lengthily on this topic. Anyway, a distinctive feature of this current transport is that not only the magnitude, but the shape itself of the I-V characteristic is determined by the interaction between injected carriers and trap states in the forbidden bandgap.

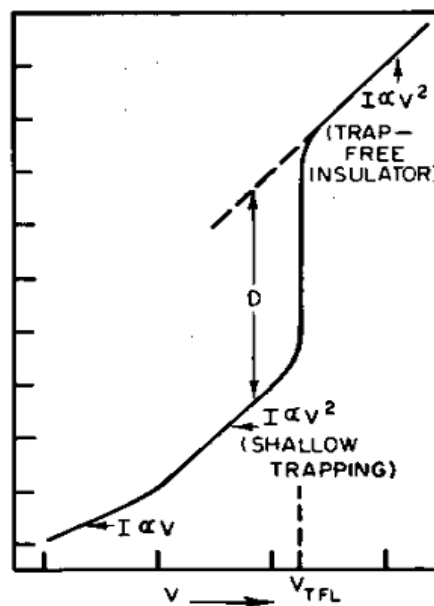


Figure 3.3-3 Log-Log plot of RT forward I-V curve in case of one-carrier SCLC injection controlled by a single set of traps. After M. A. Lampert, P. Mark, *Current Injection in Solids*, Academic Press, New York, 1970.

Figure 3.3-3 shows I-V curve in case of one-carrier SCLC injection controlled by a single set of traps. In general, if the I-V curve presents one or more power-law

$$I \propto V^m \quad (3.31)$$

regions, this is considered as a signature of SCLC current transport. In particular, the $I \propto V^2$ is the well-known **trap-free square law**.

Poole–Frenkel Current Transport

In disordered and amorphous semiconductors, the thermionic emission model fails due to the existence of trap centers. Trap sites act as potential wells, entrapping electron. By random thermal fluctuations an electron gain enough energy to escape from its localized state, and move to the conduction band, where it can move freely until relaxing into another localized state. The Poole–Frenkel effect describes how, in a large electric field, the field reduces the Coulombic potential barrier of the trap site.

The Poole–Frenkel effect manifests itself in semiconductors by exhibiting a current-voltage relationship of the kind

$$\ln\left(\frac{I}{V}\right) \propto \sqrt{V} \quad (3.32)$$

It occurs only at high applied fields ($\geq 3 \cdot 10^6 \text{ Vcm}^{-1}$) and temperatures greater or equal than 300 K. The effect has extensively been applied to conduction in amorphous materials and glasses [3.24].

3.3.3 Si Grass-Based SBDs I-Vs: Identification of the Current Transport Mechanism in the High Bias $V \geq 2$ Region

The current-voltage characteristics of the Si Grass-based SBDs have been fitted in the high bias ($V \geq 2$) region according to the different candidate models (Equations (3.30) – (3.31)). In Figure 3.3-4 are plotted the experimental data together with the corresponding fit curves for each model.

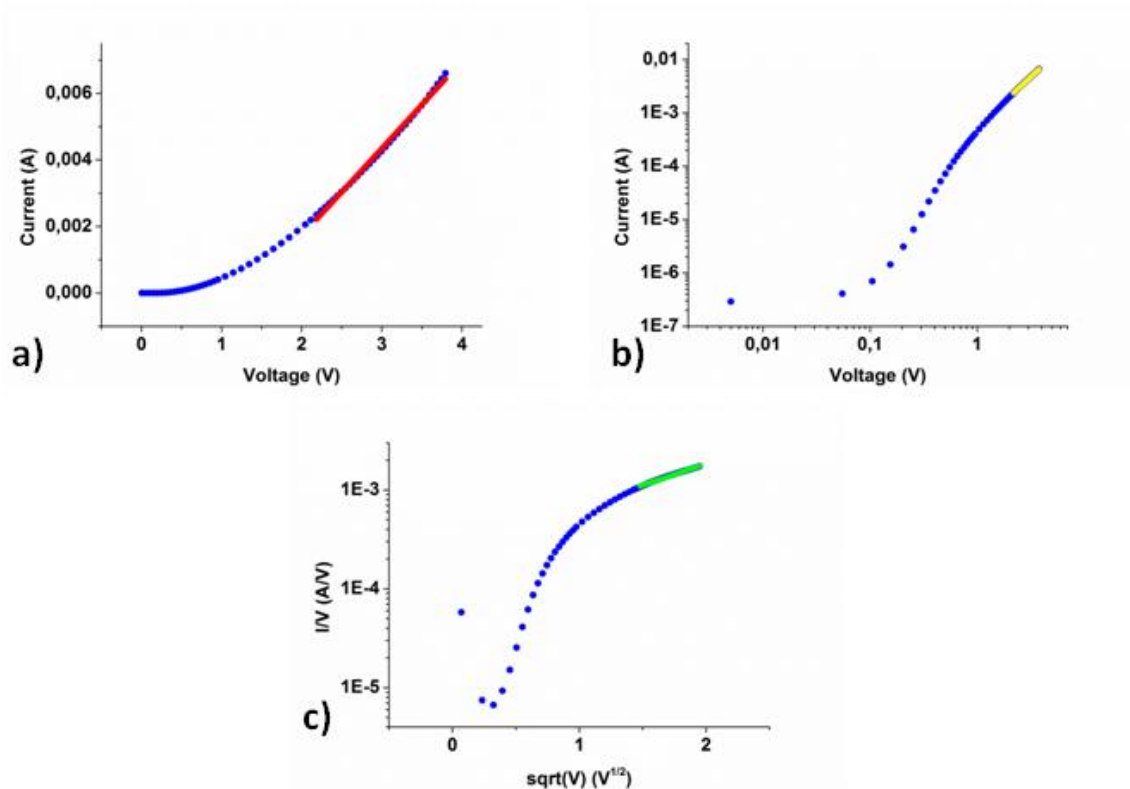


Figure 3.3-4 RT forward I-V of Si Grass-based SBDs, high bias ($V \geq 2$) region, fitted a) linearly, b) with power-law $I \propto V^m$, c) by Poole-Frenkel model.

Model fitting of experimental data is an iterative procedure in which the reduced chi-square value is minimized in order to get the optimal parameter values. The reduced chi-square is the ratio of the residual sum of squares (RSS) to the degrees of freedom (DOF). Anyway, it is better not to rely on the reduced chi-square value as a good measure of the closeness of the fit to the data points. Regression results are better interpreted according to the r-square proximity to the value of 1. But a larger value of r-square does not necessarily mean a better fit because the degrees of freedom can also affect the value. The **adjusted r-square** value accounts for the degrees of freedom and this could be a better measure of the goodness of fit. In Table 3-III are listed the adjusted r-square values for the current transport models of Equations (3.30) – (3.31). All of them are in near proximity to 1 and to each other.

Statistically speaking it is more appropriate to compare different fit results.

Model	Adjusted r-Square Value
Parasitic series resistance	0,99657
SCLC Current Transport	0,99957
Poole–Frenkel Current Transport	0,99991

Table 3-III Adjusted r-Square Values for the fitted models.

Comparing Current Transport Models by Akaike's Information Criterion

The Akaike's Information Criterion (AIC) [3.25] determine which, between two model is more likely to be correct, and it quantify how much more. The model fit to a data set can be summarized by AIC according to

$$AIC = N \cdot \ln\left(\frac{SS}{N}\right) + 2K \quad (3.33)$$

set that N is the number of data points, K is the number of parameters fit by the regression plus one, SS is the sum of the square of the vertical distances of the points from the curve. Let us consider two models, model A simpler than model B, that is model A has a greater number of parameters. The difference in AIC is defined by:

$$\begin{aligned} \Delta AIC &= AIC_B - AIC_A = N \left[\ln\left(\frac{SS_B}{N}\right) - \ln\left(\frac{SS_A}{N}\right) \right] + 2(K_B - K_A) \\ &= N \left[\ln\left(\frac{SS_B}{SS_A}\right) \right] + 2(K_B - K_A) \quad (3.34) \end{aligned}$$

- The simpler model A will almost always fit worse, so $SS_A > SS_B \Rightarrow \ln\left(\frac{SS_B}{SS_A}\right) < 0$.
- The more complex model B has more parameters, so $K_B > K_A \Rightarrow K_B - K_A > 0$.

If ΔAIC is negative, then the difference in sum-of-squares is more than expected based on the difference in number of parameters, and the conclusion is that the more complex model B is more likely. If ΔAIC is positive, then the variation in sum-of-squares is not as large as expected from the change in number of parameters, and the conclusion is that the more simpler model A is more likely.

The model with lower AIC is the more likely to be correct, according to the probability:

$$P = \frac{e^{-\Delta AIC/2}}{1 + e^{-\Delta AIC/2}} \quad (3.35)$$

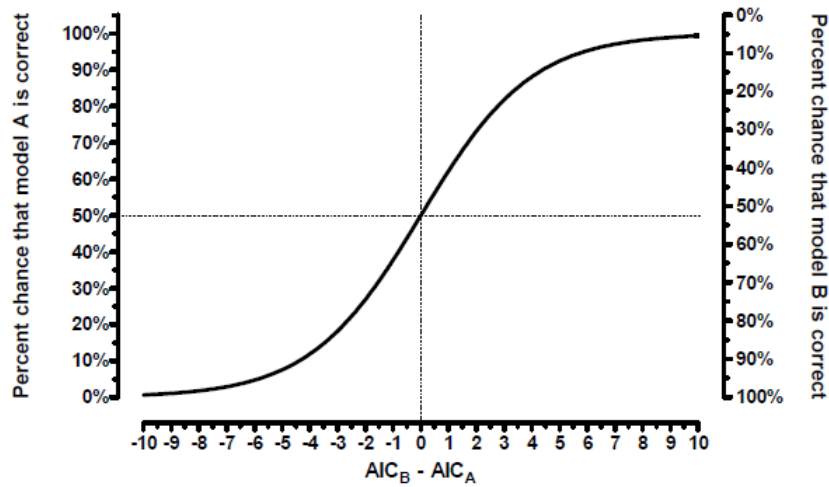


Figure 3.4-5 Relationship between the difference in AIC scores and the probability that each model is true. After H. J. Motulsky, A. Christopoulos, *Fitting Models to Biological Data Using Linear and Nonlinear Regression. A Practical Guide to Curve Fitting*. GraphPad Software Inc., San Diego CA, 2003.

The current transport models have been compared according to AIC scores. Results are reported in Table 3-IV. The SCLC current transport $I \propto V^m$, $m = 1.9$ is largely the more likely among all the models described by Equations (3.30) – (3.31).

Model A	AIC_A	Model B	AIC_B	ΔAIC
SCLC Current Transport	-743	Parasitic series resistance	-622	--121
SCLC Current Transport	-743	Poole–Frenkel Current Transport	-691	-52
Poole–Frenkel Current Transport	-691	Parasitic series resistance	-622	-69

Table 3-IV Difference in AIC values for the different pair of models.

BIBLIOGRAPHY

- [3.1] E. H. Roderick, R. H. Williams, *Metal-Semiconductor Contacts, Second Edition*. Oxford, Clarendon Press, 1988.
- [3.2] L. J. Brillson, *Surfaces and Interfaces of Electronic Materials*, WILEY-VCH Verlag GmbH & Co. KGaA, Weinheim, 2010.
- [3.3] J. Bardeen, *Physical Review*, 1947, **71**, 717.
- [3.4] S. M. Sze, *Physics of semiconductor devices*, Wiley, 1981.
- [3.5] M. Missous, E. H. Roderick, *Electronics Letter*, 1986, **22**, 477.
- [3.6] G. D. J. Smit, S. Rogge, T. M. Klapwijk, *Applied Physics Letters*, 2002, **81**, 20, 3852-3854.
- [3.7] C. Donolato, *Journal of Applied Physics*, 2004, **95**, 2184.
- [3.8] H. Hasegawa, T. Sato, S. Kasai, *Applied Surface Science*, 2000, **166**, 92–96.
- [3.9] S. M. Woodruff, N. S. Dellas, B. Z. Liu, S. M. Eichfeld, T. S. Mayer, J. M. Redwing, S. E. Mohney, *35th Conference on the Physics and Chemistry of Semiconductor Interfaces (PCSI)*, 2008, **26**, AVS, Santa Fe, New Mexico (USA), 1592-1596.
- [3.10] Y. W. Heo, L. C. Tien, D. P. Norton, S. J. Pearton, B. S. Kang, F. Ren, J. R. LaRoche, *Applied Physics Letters*, 2004, **85**, 15, 3107-3109.
- [3.11] S.-Y. Lee, S.-K. Lee, *Nanotechnology*, 2007, **18**, 49, 495701.
- [3.12] J. Piscator, O. Engström, *Physica E: Low-dimensional Systems and Nanostructures*, 2008, **40**, 7, 2508-2512.
- [3.13] L. J. Wan, W. L. Gong, K. Jiang, H. L. Li, B. R. Tao, J. Zhang, *Applied Surface Science*, 2008, **254**, 4899–4907.
- [3.14] M. Zhu, J. Zhang, Z. Wang, L. Wan, X. Chen, *Physica E*, 2010, **43**, 515–520.
- [3.15] I. Hussain, M. Y. Soomro, N. Bano, O. Nur, M. Willander, *Journal of Applied Physics*, 2013, **113**, 234509.
- [3.16] E. Fred Schubert, *Light Emitting Diodes, Second Edition*, Cambridge University Press, New York, 2006.
- [3.17] M. A. Lampert, P. Mark, *Current Injection in Solids*, Academic Press, New York, 1970.
- [3.18] K. C. Kao, W. Hwang, *Electrical Transport in Solids*, Pergamon, Oxford, 1981.
- [3.19] K. C. Kao, *Dielectric phenomena in solids*, Elsevier Academic Press, 2004.
- [3.20] V. Čech, *Solid-State Electronics*, 1997, **41**, 1, pp. 81-86.

[3.21] X. M. Shen, D. G. Zhao, Z. S. Liu, Z. F. Hu, H. Yang, J. W. Liang, *Solid-State Electronics*, 2005, **49**, 847–852.

[3.22] A.-M. Kamto Tegueu, O. Akpa, A. Guha, K. Das, *Material Research Society Symposium Proceeding*, 2007, **955**.

[3.23] R. Nana, P. Gnanachelvi, M. A. Awaah, M. H. Gowda, A. M. Kamto, Y. Wang, M. Park, K. Das, *Physica Status Solidi A*, 2010, **207**, 6, 14891496.

[3.24] H. Morkoç, *Handbook of Nitride Semiconductors and Devices Vol. 2: Electronic and Optical Processes in Nitrides*, John Wiley & Sons Inc, 2008.

[3.25] H. J. Motulsky, A. Christopoulos, *Fitting Models to Biological Data Using Linear and Nonlinear Regression. A Practical Guide to Curve Fitting*. GraphPad Software Inc., San Diego CA, 2003. www.graphpad.com

CHAPTER 4

Defect Level Characterization of Si Grass-based SBDs

4.1 Deep Levels and Their Electrical Characterization

The present paragraph is based mostly on [4.1].

4.1.1 Deep States

In semiconductors electrons and holes recombine if an electron transition occurs from the conduction band to the valence band, or are generated if the electronic transition is in the opposite direction. The Generation-Recombination processes are classified in various ways:

- **direct** or **band-band G-R**: the carrier transition occurs in a single process;
- **indirect** or **trap assisted G-R**: the carrier transition is via energy levels within the band gap;
- **non-radiative** or **thermal**: the energy involved in the transition is given by/transferred to lattice phonons it is;
- **radiative** or **optical**: the energy is balanced through a photon;
- **Auger mechanism**: energy is lost or acquired by another carrier.

Figure 4.1-1 shows the four possible non-radiative processes via a generic trap level E_T . The transition probability is exponentially related to the energy jump, then it is affected by the level position within the band gap. If the level is next to the valence band the (c) and (d) processes are more probable than the (a) and (b) ones, while if the level is next to the conduction band it is the opposite. Only when the level is close the midgap all the processes have the same probability. Generation of an electron-hole pair implies the occurring of processes (b) and (c), while its recombination the processes (a) and (d), then we speak of **G-R centre** when the level is nearby midgap situated.

The most important indirect GR mechanism is the non-radiative or Shockley-Read-Hall (SRH) one. There also exist indirect radiative mechanisms. We will not treat extensively the SRH theory. We will say only that, in a doped semiconductor, if the deep level is at or close to the midgap in low level injection condition (: the excess carriers concentrations are \ll than the majority carrier concentration) the minority carrier lifetime is:

$$\tau \sim \tau_{min0} \equiv \frac{1}{N_T \langle v_{min} \rangle \sigma_{min}} \quad (4.1)$$

set that σ is the carrier capture section, $\langle v \rangle$ is the carrier average thermal. That is τ depends on the deep level density N_t and minority carrier characteristic quantities. The recombination rate is thus limited by the minority carrier capture rate. If $\sigma_n \langle v_n \rangle = \langle v_p \rangle \sigma_p$ then the non-radiative lifetime is minimized if the trap level is at or close to the midgap energy. Deep levels are effective recombination centers if they are near the middle of the gap.

Shockley-Read-Hall Statistics

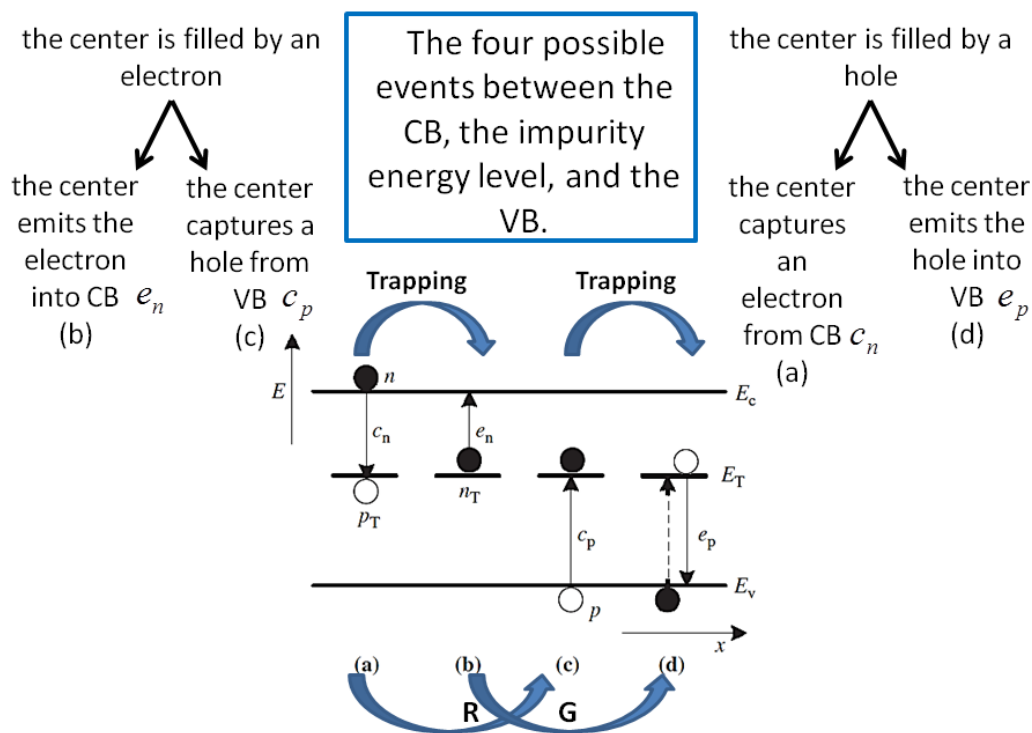


Figure 4.1-1 Emission and capture processes at a deep level: (a) hole emission to the valence band, (b) electron capture from the conduction band, (c) hole capture from the valence band, (d) electron emission to the valence band.

Transient Response

Let us consider a deep state with energy E_t and concentration N_t for a n-type semiconductor. The four basic processes which determine its population dynamic are the capture and emission (from and to the relative band) for both carriers. We will consider a deep centre exposed to a flux of $n\langle v_n \rangle$ electrons per unit area per unit time. If n_t deep states out of N_t are occupied by electrons at any instant, in a successive time interval Δt the number of electrons captured by the $p_t \equiv N_t - n_t$ unoccupied states is $\Delta n_t \sigma_n \langle v_n \rangle n (N_t - n_t) \Delta t$, for n the electron capture cross section. The electron capture rate per unoccupied state is:

$$c_n \equiv \frac{1}{N_t - n_t} \cdot \frac{\Delta n_t}{\Delta t} = \sigma_n \langle v_n \rangle n \quad (4.2)$$

An analogue expression holds for the hole capture rate per occupied state. Due to recombination of electrons and holes at the deep centre, the carrier capture rate is related to the minority carrier lifetime: for a p-type semiconductor $\frac{1}{\tau} = \frac{1}{n} \cdot \frac{\Delta n_t}{\Delta t}$, thus the non radiative lifetime associated with electron capture at the deep state is $\tau_{nonrad} = \sigma_n \langle v_n \rangle (N_t - n_t)$.

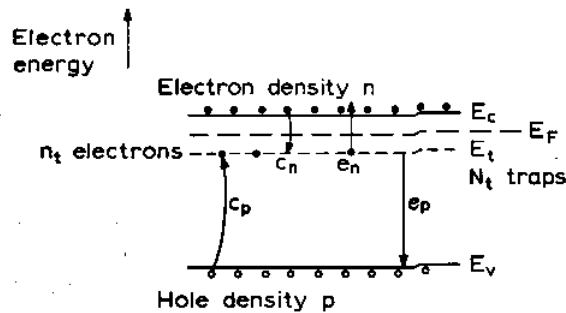


Figure 4.1-2 Electron and hole capture and emission processes for an electron trap in a n-type semiconductor. After P. Blood, J. W. Orton, *The electrical characterization of semiconductors: majority carriers and electron states*, London: Academic Press, 1990.

The electron occupancy of the deep state is determined by the competing processes of emission and capture. Electrons are emitted/holes are captured at the n_t occupied states, holes are emitted/electrons are captured at the p_t unoccupied states, and the net change rate of electron occupancy is

$$\frac{dn_t}{dt} \equiv (c_n + e_p)(N_t - n_t) - (c_p + e_n)n_t \quad (4.3)$$

for e_n, e_p the electron, hole emission rates. Solutions to Equation (4.3), termed as the **rate equation**, can be obtained when $N_t \ll N_d - N_a$, that is the trap density is largely smaller than the net doping density. This because the free carriers

concentrations n , p are not influenced by these processes and can be considered constant.

If we set the boundary condition $n_t(t = 0) = n_t(0)$, then the general solution of the rate equation (4.3) is:

$$n_t(t) = n_t(\infty) - [n_t(\infty) - n_t(0)] \exp\left(-\frac{t}{\tau}\right) \quad (4.4)$$

being the **steady state occupancy**

$$\frac{n_t(\infty)}{N_t} \equiv \frac{a}{a+b} \quad (4.5)$$

and the **time constant** $\tau \equiv \frac{1}{a+b}$ is, $a \equiv c_n + e_p$, $b \equiv e_n + c_p$. The **initial occupancy** $\frac{n_t(0)}{N_t}$ is usually set experimentally: when it differs from the equilibrium value $\frac{n_t(\infty)}{N_t}$, then the occupancy relaxes exponentially to this latter with rate constant $a + b$. Two special cases are:

$$n_t(0) = N_t \Rightarrow n_t(t) = \frac{N_t}{a+b} \left[a + b \exp\left(-\frac{t}{\tau}\right) \right] \quad (4.6)$$

$$n_t(0) = 0 \Rightarrow n_t(t) = n_t(\infty) \left[1 - \exp\left(-\frac{t}{\tau}\right) \right] \quad (4.7)$$

- Carefulness must be paid in distinguishing between the rate of change of n_t , and the emission and capture rates. For instance, when the only process is that of electron emission, then the instantaneous rate of emission of electrons from the trap is $\frac{dn_t}{dt} = -e_n n_t(t)$, which is time dependent, while e_n is the emission rate *per trapped electron*, i.e. the probability per unit time that a single electron is emitted.

The Trap Signature

At thermal equilibrium, it holds:

- the steady state condition: $\frac{dn_t}{dt} = 0$,
- the **principle of detailed balance**: the rates for a process and its inverse must be equal and balance in detail (so that it does not occur a net electron transfer from a band to another):

$$\begin{aligned} e_n n_t &= c_n (N_t - n_t) \\ e_p (N_t - n_t) &= c_p n_t \end{aligned} \quad (4.8)$$

By combining the above requirements with the rate Equation (4.2), we find that the thermal equilibrium trap occupancy is

$$\frac{c_n}{c_n + e_n} = \frac{\widehat{n}_t}{N_t} = \frac{e_p}{e_p + c_p} \quad (4.9)$$

On the other hand, at thermal equilibrium, the electron occupancy is ruled by Fermi-Dirac statistics, and so $\frac{\widehat{n}_t}{N_t} = \frac{1}{1 + g \exp\left(\frac{E_t - E_F}{k_B T}\right)}$, set that $g \equiv \frac{g_0}{g_1}$ is the **degeneracy ratio**, g_0 being the degeneracy of the trap level E_t when it is electron-less and g_1 the one when the trap level is occupied by one electron. Thus we can relate the capture and emission rates for both carriers:

$$\frac{e_n}{c_n} = g \exp\left(\frac{E_t - E_F}{k_B T}\right) = \frac{c_p}{e_p} \quad (4.10)$$

Since g is of order of unity, then, roughly speaking: if $E_F > E_t \Rightarrow c_n > e_n, e_p > c_p$, while if $E_F < E_t \Rightarrow c_n < e_n, e_p < c_p$. If $E_F = E_t \Rightarrow c_n \sim e_n, e_p \sim c_p$. Strictly speaking $e_n = c_n$ when $E_F = E_t - k_B T \ln g$.

Because of Equation (4.2), the capture rate c_n is dependent on the doping density. The analogue is valid for c_p too. Instead, the emission rates and the capture cross sections are intrinsic characteristics of the trap. From Equations (4.2) and (4.10) we derive that:

$$e_n = \sigma_n \langle v_n \rangle g \exp\left(-\frac{E_C - E_t}{k_B T}\right) \quad (4.11)$$

$$e_p = \sigma_p \langle v_p \rangle \frac{1}{g} \exp\left(-\frac{E_t - E_V}{k_B T}\right) \quad (4.12)$$

For a non degenerate semiconductor holds the Boltzmann approximation:

$$n = N_C \exp\left(-\frac{E_C - E_t}{k_B T}\right) \quad (4.13)$$

$$p = N_V \exp\left(-\frac{E_t - E_V}{k_B T}\right) \quad (4.14)$$

Since $\langle v_n \rangle = \sqrt{\frac{3k_B T}{m^*}}$, $N_C = 2M_C \left(\frac{2\pi m^* k_B T}{h^2}\right)^{3/2}$ for M_C the number of conduction band minima, the temperature dependence of the emission rates in case of electron emission is:

$$e_n(T) \equiv \gamma T^2 \sigma_{na} \exp\left(-\frac{E_{na}}{k_B T}\right) \quad (4.15)$$

if we assume that $\sigma(T) \equiv \sigma_\infty \exp\left(-\frac{\Delta E_\sigma}{k_B T}\right)$. The **trap signature** is the plot of $\ln \frac{e_n}{T^2}$ versus $\frac{1}{T}$, and it is a straight line. Experimental data for most traps fit the above curve

over many orders of magnitude of e_n . Let us observe that the **apparent activation energy** $E_{na} \equiv E_C - E_t + \Delta E_\sigma$ is not the trap level, and that the **apparent capture cross section** σ_{na} is proportional to the extrapolated ($T = \infty$) value of the capture cross section through the degeneracy factor. Both the identifications are valid only if $E_C - E_t$ is temperature independent. Traps are catalogued according the E_{na} and σ_{na} values.

Electron Trap and Hole Trap

From Equations (4.11), (4.12) we find that $e_n = e_p$ if:

$$E_t = E_1 \equiv E_{Fi} + \frac{k_B T}{2} \ln \left(\frac{\sigma_p \langle v_p \rangle}{\sigma_n \langle v_n \rangle} \right) \quad (4.16)$$

Since the **intrinsic Fermi level** is $E_{Fi} + \frac{k_B T}{2} \ln \left(\frac{\sigma_p \langle v_p \rangle}{\sigma_n \langle v_n \rangle} \right)$, then the energy E_1 is located near the midgap. The deep level E_t is called an **electron trap** if it is $e_n > e_p$, that is it is located in the upper part of the gap ($E_t > E_1$), while it is an **hole trap** if it is $e_n < e_p$, that is it is located in the lower part of the gap.

Majority and Minority Carrier Traps

Up to now we have showed that:

- the relation $e_n \gtrless e_p$, which establish if the trap is electron-kind or hole-kind, is determined by the position of the trap level E_t respect to the energy E_1 (Equation (4.16));
- the ratio $\frac{e}{c}$ depends on the relative positions of E_t , E_F (Equation (4.10)). But, if we assume that $N_t \ll N_d - N_a$, then E_F is controlled by the doping, that is it is close to:
 - the conduction band edge for a n-type semiconductor $\Rightarrow E_F > E_t$,
 - the valence band edge for a p-type semiconductor $\Rightarrow E_F < E_t$.

By combining the two points above, we find that (Figure 4.1-3):

- an electron trap ($e_n \gg e_p$) in a n-type semiconductor ($c_n > e_n$, $e_p > c_p$) is such that $c_n > e_n \gg e_p > c_p \Rightarrow n_t(t)$ relaxes with time constant $\tau \equiv \frac{1}{c_n + e_n}$. The equilibrium occupancy is $\frac{n_t(\infty)}{N_t} = \frac{c_n}{c_n + e_n}$, thus if $c_n \gg e_n$ then at equilibrium $\widehat{n}_t = N_t$.
- a hole trap ($e_n \ll e_p$) in a p-type semiconductor ($c_n < e_n$, $e_p < c_p$) is such that $c_n < e_n \ll e_p < c_p \Rightarrow n_t(t)$ relaxes with time constant $\tau \equiv \frac{1}{c_p + e_p}$. The

equilibrium occupancy is $\frac{n_t(\infty)}{N_t} = \frac{e_p}{e_p + c_p}$, thus if $c_p \gg e_p$ then at equilibrium $\widehat{n}_t = 0 \Rightarrow \widehat{p}_t = N_t$.

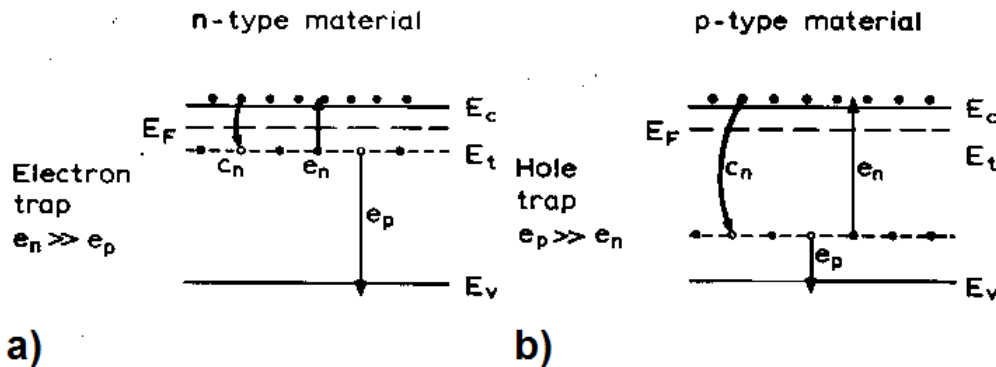


Figure 4.1-3 Majority carrier traps. After P. Blood, J. W. Orton, *The electrical characterization of semiconductors: majority carriers and electron states*, London: Academic Press, 1990.

We can generalize: we speak of **majority carrier** (electron type (electron for n-type material, hole for p-type one) **trap** when $e_{maj} \gg e_{min}$ and E_t is close to the majority carrier band edge; the majority carrier equilibrium occupancy is equal to N_t if $c_{maj} \gg e_{maj}$.

By analogy we speak of **minority carrier trap** (Figure 4.1-4) for:

- an electron trap in a p-type semiconductor. Now only c_n is negligible (because $c_n \propto n \Rightarrow n_t(t)$ relaxes with time constant $\tau \equiv \frac{1}{e_p + e_n + c_p}$. The equilibrium occupancy is $\frac{n_t(\infty)}{N_t} = \frac{e_p}{e_p + e_n + c_p} \Rightarrow$ the relaxation process involves the exchange of carriers with both bands, and the equilibrium value $\widehat{p}_t = N_t$ the equilibrium value is reached when both hole capture and electron emission dominate over hole emission.
- a hole trap in a n-type semiconductor: $n_t(t)$ relaxes with time constant $\tau \equiv \frac{1}{c_n + e_p + e_n}$. The equilibrium occupancy is $\frac{n_t(\infty)}{N_t} = \frac{c_n + e_p}{c_n + e_p + e_n} \Rightarrow$ the equilibrium value $\widehat{n}_t = N_t$ is reached when electron capture and hole emission dominate over electron capture.

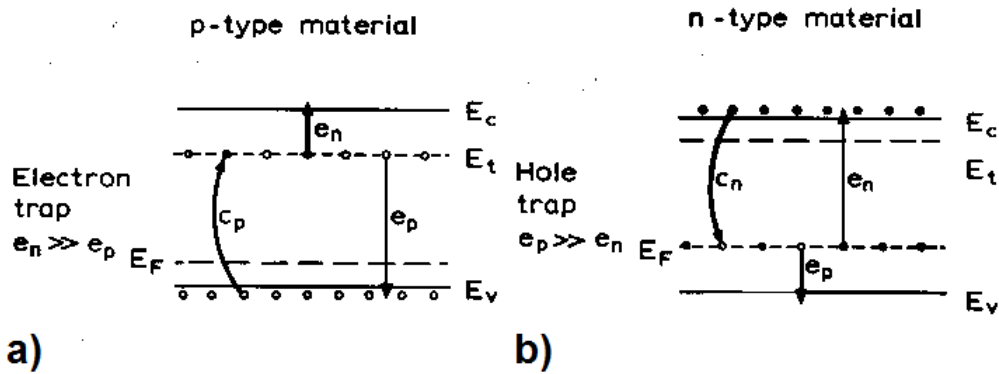


Figure 4.1-4 Minority carrier traps. After P. Blood, J. W. Orton, *The electrical characterization of semiconductors: majority carriers and electron states*, London: Academic Press, 1990.

Again E_t is close to the appropriate (: minority carrier) band edge. The distinctive feature of minority carrier traps is that the equilibrium occupancy is established through interaction with both bands: it follows that the trap occupancy cannot be perturbed from its equilibrium value by simply acting on the majority carrier population, as in the case of majority carrier traps.

4.1.2 Basis of Transient Depletion Experiment for a Majority Carrier Trap

We now will examine the sequence in a transient depletion experiment for a Schottky barrier on a n-type semiconductor, the latter containing a donor-like majority carrier trap with energy level E_t . With no bias applied, deep states in neutral material (: $x > x_0$, set that x_0 is the depletion depth at zero bias) are occupied because $c_n > e_n$.

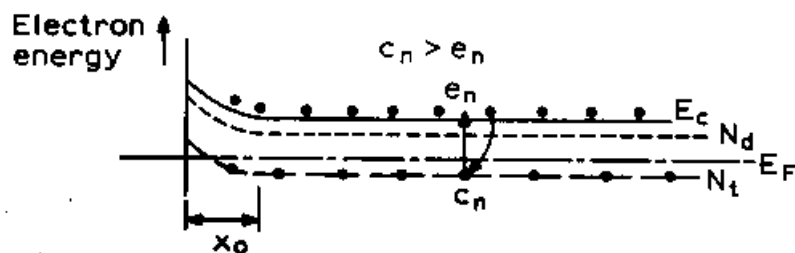


Figure 4.1-5 Conduction band diagram at zero bias applied. After P. Blood, J. W. Orton, *The electrical characterization of semiconductors: majority carriers and electron states*, London: Academic Press, 1990.

By applying suddenly a reverse bias V_R , within the enlarged depletion region the capture process of electrons from the conduction band to the trap level is turned off. The traps empty, and the emitted electrons are rapidly swept out of the depletion region by the associated field.

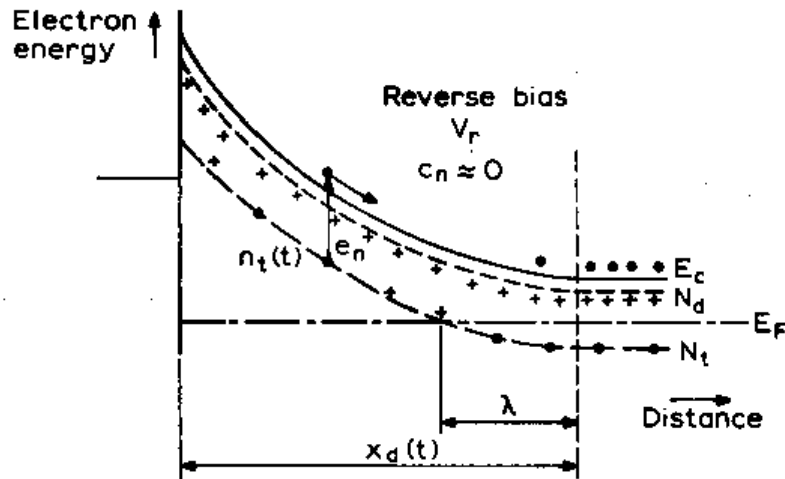


Figure 4.1-6 Conduction band diagram at reverse bias applied. After P. Blood, J. W. Orton, *The electrical characterization of semiconductors: majority carriers and electron states*, London: Academic Press, 1990.

Let us define the transition distance $\lambda \equiv x_n - x_1$, set that x_n is the zero bias depletion edge and x_1 is the point in which the trap level crosses the Fermi level. In case the bias applied is so large that $\lambda \ll x_n$, the net space charge density during the emission process is $\rho(x) = q [N_d + N_t - n_t(t)]$.

The parallel plate expression for the capacitance associated with a bias V applied across the depletion depth of a Schottky junction is:

$$C = A \left(\frac{\epsilon_S q N_d}{2} \right)^{1/2} V^{-1/2} \quad (4.17)$$

set that A is the junction area, ϵ_S is the semiconductor permittivity, q is the electron charge. We get the time dependent capacitance by substituting in (4.17) $N_d \rightarrow N_d + N_t - n_t(t)$:

$$C(t) = A \left(\frac{\epsilon_S q}{2} \right)^{1/2} [N_d + N_t - n_t(t)] V^{-1/2} \equiv C(\infty) \left[1 - \frac{n_t(t)}{N_d + N_t} \right]^{1/2} \quad (4.18)$$

$C(\infty)$ is the **steady state** (since $n_t(\infty) = 0$ within the depletion region) **capacitance**.

In the **dilute trap concentration limit** $N_t \ll N_d \Rightarrow n_t \ll N_d$ the square root term in the above equation can be expanded, so that the change in capacitance is:

$$\Delta C(t) = C(t) - C(\infty) \sim -\frac{n_t(t)}{2N_d} C(\infty) \quad (4.19)$$

Because the initial occupancy is $n_t(0) = N_t$, then $n_t(t)$ follows a decaying law expressed by Equation (4.6). For a majority carrier trap $c_{maj} > e_{maj}$ are the only not-negligible capture and emission rates, so $a + b = c_{maj} + e_{maj}$. In our case (: electron trap) the only possible process being that of electron emission, then $a + b = b = e_n$. Finally $n_t(t) = N_t \exp(-e_n t)$ and thus:

$$\frac{\Delta C(t)}{C(\infty)} = -\frac{N_t}{2N_d} \exp(-e_n t) \quad (4.20)$$

If the reverse bias is removed then the empty traps are refilled by electron capture. Equation (4.20), which states that the capacitance increases exponentially with time as carriers are emitted from the trap, is the basis of the transient capacitance techniques and the DLTS ones. According to it the time constant of the capacitance transient gives the thermal emission rate, and

$$\Delta C_0 \equiv \Delta C(0) = -\frac{N_t}{2N_d} C(\infty) \quad (4.21)$$

4.1.3 Deep Level Transient Spectroscopy (DLTS)

DLTS is a widely used spectroscopic technique to observe thermal emission from majority carrier traps in semiconductor materials. It allows the extraction of concentration, thermal activation energy and capture cross sections of deep level defects. DLTS uses capacitance, voltage or current transient signals resulting from relaxation processes following an abrupt change of the bias voltage or light applied to the investigated sample. According to the measured transient signal, we distinguish in capacitance (C-) DLTS, constant capacitance (CC-) DLTS, current (I-) DLTS respectively. The specific details of these methods may be found in [4.2, 1.29] (C-DLTS and CC-DLTS) and [4.3] (I-DLTS).

In this work the defect level characterization has been performed by means of the C-DLTS method, originally proposed in [4.4].

C-DLTS: Principle of Operation

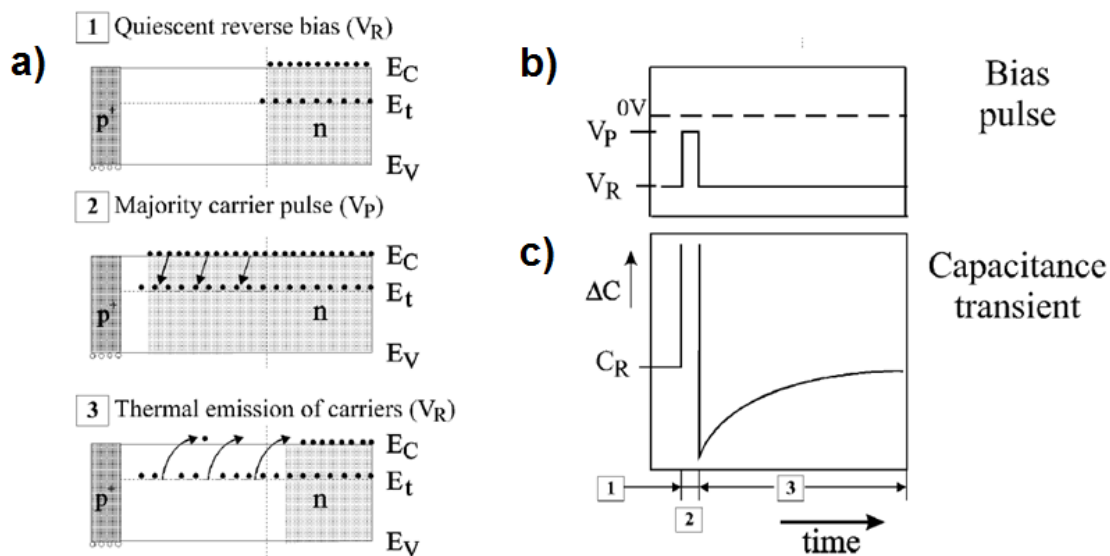


Figure 4.1-7 Principle of C-DLTS operation by reduced reverse bias pulse for majority carrier injection. a) Charge state of defects, b) bias pulsing, c) time dependence of the capacitance during the measurement. After *Radiation Damage in Silicon Particle Detectors - Microscopic Defects and Macroscopic Properties* - PhD thesis, [DESY-THESIS-1999-040](#), December 1999

States in the depletion region of a reversely biased junction have no possibility of being filled by capture processes due to the depletion of free charge carriers. The emission processes can be induced in order to be characterized only forcedly introducing carriers in the depletion region, which are to be captured. One way to get this is by pulsing of the voltage applied across the junction (Figure 4.1-7 a).

We will assume in the following for simplicity that only an electron trap in the upper half of the band gap is present in a n-type semiconductor. The measurement is performed by repeating periodically the following steps:

1. a reverse bias V_R is applied across the junction; the defect states within the depletion region are not occupied by electrons.
2. the junction is pulsed (for a short time interval t_{fill}) with a positive smaller voltage V_P . Consequently the depletion region is temporarily reduced from width W to W' . The traps within $\Delta W = W - W'$ are filled with majority carriers, in this case electrons, allowing them to be captured. Since defect levels are now below the Fermi level, they will be filled by electrons. The parameter t_{fill} affects the filling level of the traps, while the relative magnitude of $V_R + V_{bi}$, V_P the probed region. In fact, the whole ($V_R + V_{bi} \sim V_P$) or only a section ($V_R + V_{bi} > V_P$) of W is thus repleted during the filling pulse t_{fill} . In the former case the instrument is probably overloaded with the high zero capacitance.

3. the reverse bias V_R is restored across the junction by turning off the voltage pulse (for a time interval t_R). The junction capacitance is reduced because compensating negative charges have been trapped in the depletion region. These charges are subsequently emitted with rate $\frac{1}{\tau}$ into the conduction band, if sufficient thermal excitation energy is present. They are swept away from the depletion region by the applied junction bias. Consequently we observe a transient capacitance (Figure 4.1-7 c):

$$C(t) = C(\infty) + \Delta C(0) \exp\left(-\frac{t + t_0}{\tau}\right) \quad (4.22)$$

Since the level of compensation becomes smaller as electrons are emitted, the depletion region depth is decreasing and the capacitance is increasing.

The characteristic time constant of the capacitance transient is τ .

The capacitance bridge needs some time to give the correct capacitance after the turning off of the filling pulse (pulse overload recovery, Figure 4.1-8 a), then a delay period t_0 has to be included before recording the transient.

This sequence is repeated periodically, with time period $t_P \equiv t_{fill} + t_R$. During the DLTS measurement, the temperature is slowly increased.

C-DLTS notably gives the possibility to discriminate between electron and hole traps by the sign of the observed capacitance transient $\Delta C(t)$. The signals arising from electron and hole traps in n-type semiconductors correspond to positive and negative peaks in C-DLTS spectra, respectively.

The Two-Point Subtraction Rate Window Principle

At the core of the DLTS technique is the principle of the two-point subtraction rate window, whose implementation we illustrate through the use of the double box-car or standard dual-gate signal averager system. Every capacitance signal, following the periodical bias pulse, is sampled by two gates set at times t_1 and t_2 from the onset of the transient ($t = 0$). This is equivalent to integrate the product of the signal and the weight function $w(t)$. The first gate t_1 should be set so to avoid the overload recovery part of the capacitance signal. With a small gate width $\Delta t \ll \tau$, under the hypothesis that transients are exponential, the box-car steady signal output is:

$$S(\tau) \propto C(t_1) - C(t_2) = \Delta C(0) \left[\exp\left(-\frac{t_1}{\tau}\right) - \exp\left(-\frac{t_2}{\tau}\right) \right] \quad (4.23)$$

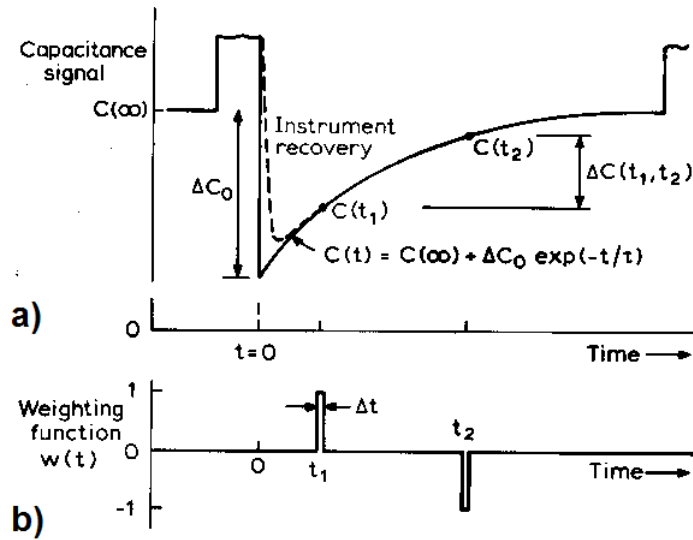


Figure 4.1-8 Schematics of the principle of the two-point subtraction rate window: a) the capacitance transient sampled at times t_1 , t_2 , b) the weighting function $w(t)$. After P. Blood, J. W. Orton, *The electrical characterization of semiconductors: majority carriers and electron states*, London: Academic Press, 1990.

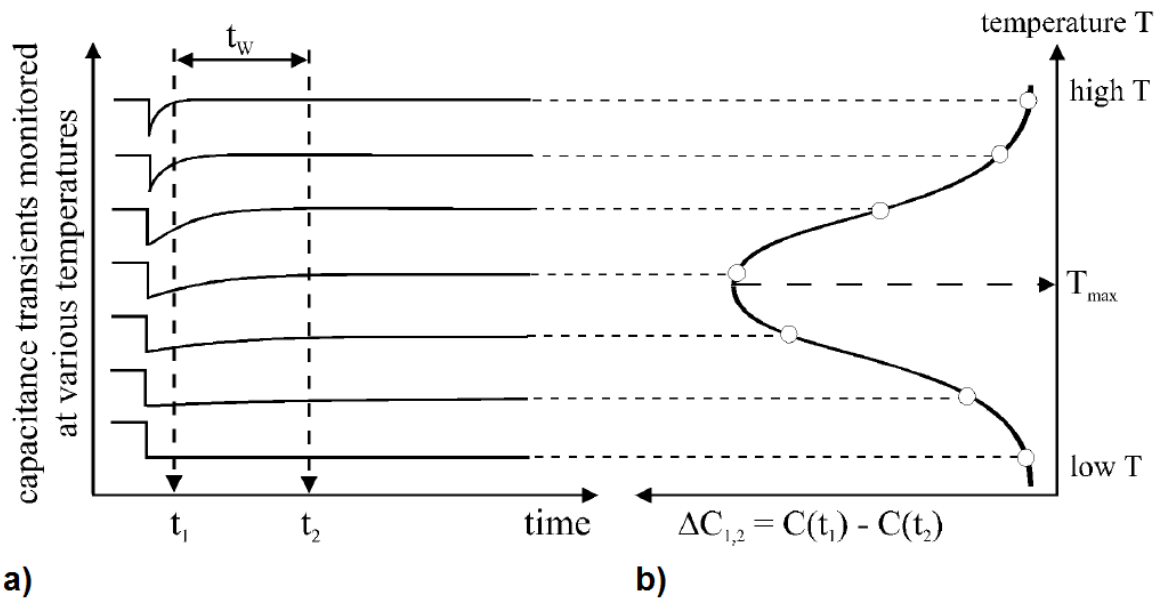


Figure 4.1-9 a) Capacitance transients at various temperatures, b) corresponding double box-car DLTS signal.

As we can see from Equation (4.23) and Figure 4.1-9, the signal output is zero for $\tau \ll t_1$ or $\tau \gg t_2$, not negligible only if $\tau \sim t_1, t_2$. For $t_1 < t_2$, $S(\tau) < 0$ for majority carrier traps, $S(\tau) > 0$ for minority carrier ones. Set that $\tau = \frac{1}{e_n}$, the peak output is

determined by the condition $0 = \frac{dS(T)}{dT} = \frac{dS(e_n)}{de_n} \cdot \frac{de_n}{dT}$, which is reduced to $\frac{dS(e_n)}{de_n} = 0$ since it holds $\frac{de_n}{dT} \neq 0 \forall T$ (see Equation (4.15)), and thus it occurs when

$$\tau_{ref} \equiv \ln \frac{t_2 - t_1}{\ln \frac{t_2}{t_1}} \quad (4.24)$$

for τ_{ref} the reference time constant of the rate window $t_2 - t_1$, which depends only by t_2, t_1 . By presetting τ_{ref} at the beginning of the DLST measurement, the peak temperature T_{peak} will result characteristic of the trap. The emission rate $e_n(T_{peak})$ will be equal to $\frac{1}{\tau_{ref}}$. By repeating the temperature scan with different values of τ_{ref} , sets of values $(T_{peak}, e_n(T_{peak}))$ are measured. From them we can generate an Arrhenius plot of $\ln \frac{T^2}{e_n}$ versus $\frac{1}{T}$, and finally determine the trap parameters E_{na}, σ_{na} . $S_{peak} \equiv S(\tau_{ref})$ is function only of the ratio $\beta \equiv \frac{t_2}{t_1}$, in fact:

$$S_{peak} \propto \Delta C(0) \left[\exp\left(-\frac{\ln \beta}{\beta - 1}\right) - \exp\left(-\frac{\beta \ln \beta}{\beta - 1}\right) \right] \quad (4.25)$$

By changing τ_{ref} such that β is constant the peak height results independent from τ_{ref} . Because $S_{peak} \propto \Delta C(0)$, from Equation (4.20) we can estimate the trap concentration.

Since the transient is not recorded directly, it is possible to work with time constants as short as a few ms. The repetition time can also be short (~ 10 ms), so that e_n is actually constant over several cycles and thus the output signal is averaged without prolonging the scan time, provided that τ_{ref} values are not too long.

4.2 Damages Induced by the RIE Mechanism

Electronic transport and optical properties of semiconductor materials are greatly sensitive to the presence of imperfections in their crystal lattice. Therefore, it is of paramount importance to study how the processes involved in device fabrication may contribute to generate new defects in the as-grown material. The aim is to understand how they possibly affect the behavior of the realized devices and if it is possible to minimize them.

In Chapter 2 the RIE technique has been briefly reviewed. Dry etching typically involves the interplay between chemically reactive species and fluxes of energetic particles, whose simultaneous exposure yields the highly directional etch of the material. However, both the chemical and physical factors at the basis of the etching

process are also intimately related to the damages of the surfaces and sidewalls of the etched structures.

4.2.1 Survey on the RIE Damage

Energetic Particle Flux

The main indicator of the energy of the ions impinging on the substrate is usually considered to be the DC bias voltage applied to the substrate electrode. However, the ions are actually accelerated in an electric field determined by the negative DC bias and the positive plasma potential (see Subsection 2.2.1 about the description of the main RIE etching systems, both the CCP and ICP). This latter may be substantial. In the RIE process the ions are always distributed in energies, because [4.5]:

1. the ion acceleration at the edge of the sheath starts at different phases of the RF;
2. the ions may undergo collisions and charge exchange while traversing the dark space above the substrate electrode.

In general, the lower is the ion energy, the lower is the lattice damage because the momentum transfer to the surface is minimized and cascade processes in the solid are avoided. The chemical and physical fluxes are interdependent: ion energies of more than 100eV are often required for anisotropic etching, at the given levels of pressure/RF power levels.

Beam-Solid Interaction Processes

Dry etching damage leads to the generation of some traps and dislocation loops, strain induced modifications, changes in stoichiometry, differently with respect to gross structural disorder as with ion implantation. As regards the changes of the electrical properties, enhanced depletion, increased leakage and higher contact resistance have been observed. As regards the optical properties, non-radiative recombination processes increase leading to a decrease of Photoluminescence and Cathodoluminescence intensity. In particular, damage build-up on surfaces and sidewalls significantly differ.

Plasma related impurities can penetrate the substrate during RIE, either as a result of the implantation or the diffusion. Heavier ions show a lower damage penetration depth, while lower particle energies cause a smaller damage penetration range [4.6 – 4.8]. The damage depth has been attributed to channeling of the ions into the material [4.9].

Point defects or/and extended defects can be introduced into RIE processed substrate. In case of silicon etched with CF₄ plasmas, as achieved by radiation

damage studies (carbon-carbon-silicon self-interstitial complexes [4.10, 4.11]) point defects have been observed.

Surface residues

These can be related to the chemistry of discharge such as the fluorocarbon or due to the formation of not-volatile products with film impurities, e.g. CaF_2 from Ca in quartz etching. They can also depend on the particular etching chamber configuration (material composition of the electrode).

Heavy Metal Contamination

Sputtering of stainless steel parts of the etching chamber may induce transition metal contamination (nickel, iron and chromium) [4.12]. These impurities diffuse very quickly into the semiconductor and may introduce midgap energy levels.

4.3 DLTS Characterization of Si Grass-Based SBDs

4.3.1 Challenges of DLTS Characterization of Semiconductor NWs

As shown in Subsection 4.1.3, the DLTS method needs a depletion region in the probed structures to be reversely voltage pulsed in order to induce the carrier emission from the trapping centers. The commonly used configuration for DLTS characterization are Schottky diodes or p-n junctions. According to the Double Boxcar method used to perform DLTS in this thesis, the DLTS signal is proportional to the difference in capacitance transients measured at two sampling times t_1 and t_2 (Equation (4.23)). In case of bulk semiconductor samples, the average capacitance usually ranges from 10 to about 300 pF, while the amplitudes of typical DLTS transients range from about 10^{-1} down to less than 10^{-4} times the sample average capacitance. To observe a DLTS signal with amplitude $\frac{\Delta C(t)}{C(\infty)} \sim 10^{-4}$ then the system has to measure transients $\Delta C(t) \sim 10^{-15}$ F, that is with amplitude as low as 1 fF superimposed on a background capacitance $C(\infty) \sim 10$ pF. The noise in the system should be an order of magnitude less than the smallest expected transient, i.e. 0.1 fF, in order to have a reliable signal to noise ratio.

To date, very few capacitance measurements on single semiconductor NWs have been reported [4.13 – 4.15], due to the difficulty of these measurements from both the fundamental and technical point of view. The capacitance values reported in literature lie in the fF regime, which is well below the required minimum bulk capacitance $C(\infty) \sim 10$ pF for performing C-DLTS. This technical limitation has forbidden up to now the application of the C-DLTS technique to detect the electrically active defects in a single semiconductor NW. In case of NW array-based SBDs the single NW SBDs are connected in parallel, thus allowing the summing up of their capacitances (Figure 4.3-1) till reaching macroscopically detectable values.

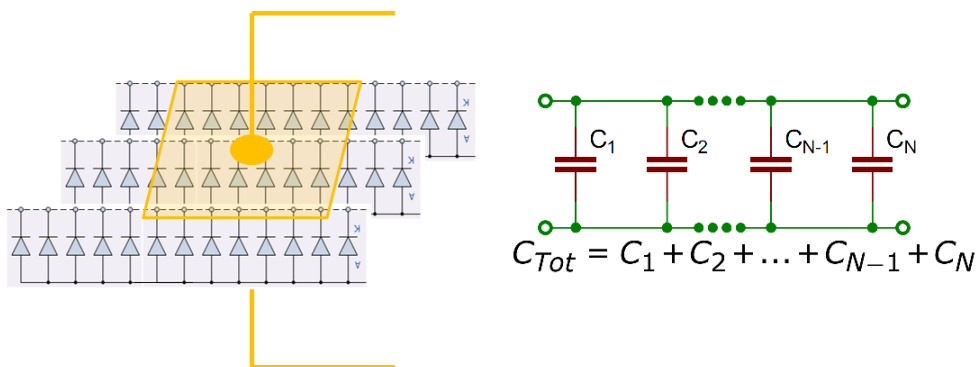


Figure 4.3-1 Schematic of the ideal equivalent circuit of a NW array-based SBD.

The realization of NW-based SBDs represents a prerequisite for the C-DLTS characterization of semiconductor NWs. Various device architectures have been adopted, all of them bearing the name of NW array-based SBDs. The main difference lies in the presence or absence of a filler material for the NW encapsulation. In the framework of C-DLTS, by providing a way for avoiding shunting paths to the substrate the filler also ensures that the C-DLTS measurement is actually probing only the NW arrays, excluding any unwanted influence from the substrate.

4.3.2 C- DLTS Measurements of Si Grass-Based SBDs

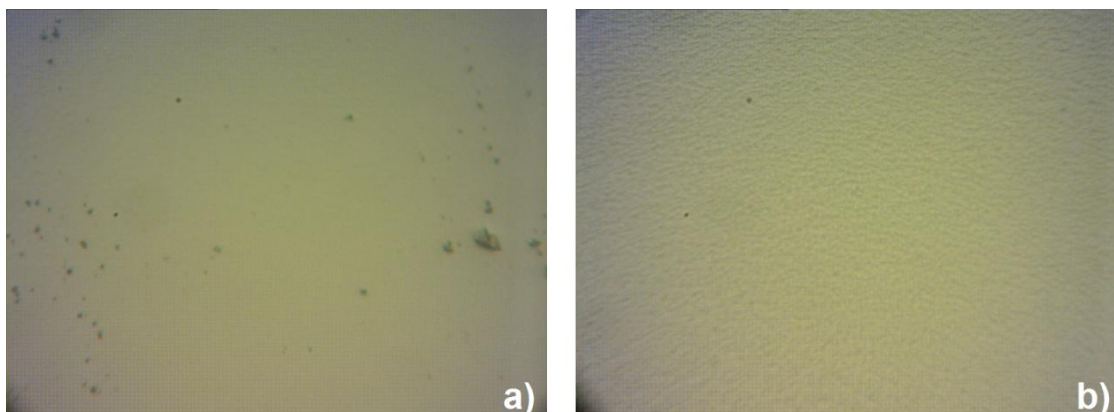


Figure 4.3-2 Optical images of the substrate surface of a) sample I, b) sample II.

Three sets of samples have been fabricated and investigated:

set I: SBD realized with the unprocessed Si substrate,

set II: SBD realized with a RIE processed Si substrate,

set III: Si Grass-based SBD.

The realization of set III has been exhaustively described in Section 2.2 of this thesis. The original Si wafer has been used also for the fabrication of set I and II (the details are reported in Subsection 2.1.3). Set II has been obtained by dry etching a Si wafer under the same conditions as those for the Si Grass formation. Only, the unbalancing between the passivation and the etching steps has been avoided. Figure 4.3-2 shows the optical images of the surfaces of samples of set I and II before the contact deposition.

The samples of sets I and II have been realized to check the defects actually induced by RIE and by the nanowire peculiarities. DLTS measurements of samples I have been performed to understand which kind of damage the dry etching could induce with respect to the virgin Si wafer. The DLTS measurements of sample II have aimed to determine if the growth of the Si NWs has introduced further defects in the Si lattice.

All the DLTS measurements have been performed with the following instrumental parameters:

V_R (V)	V_P (V)	t_{fill} (ms)
-4	+4	10

C- DLTS Measurements of Samples from Set I

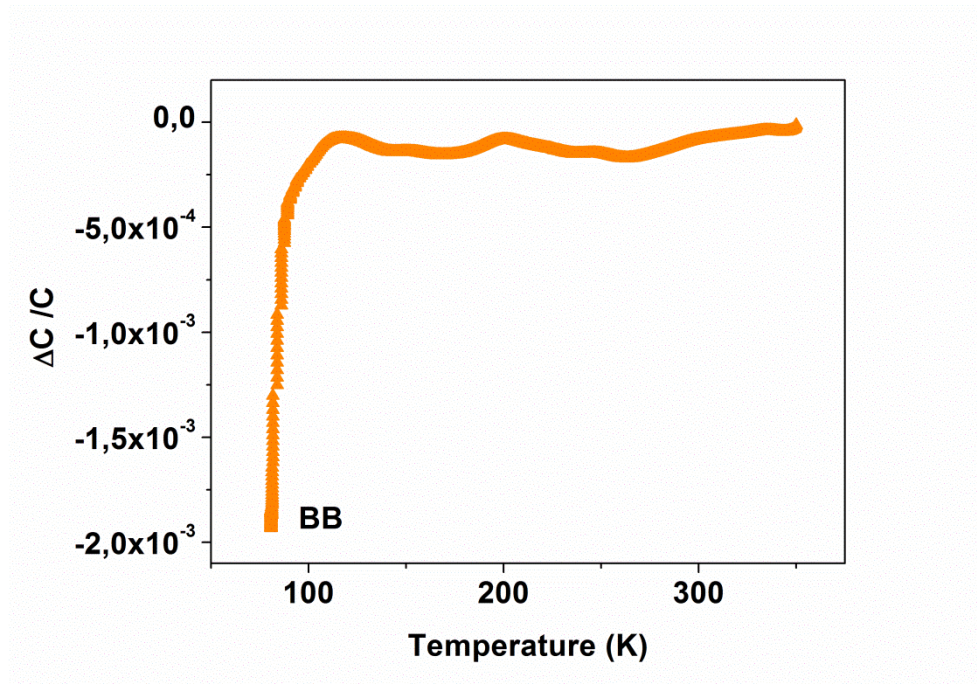


Figure 4.3-3 DLTS spectrum at emission rate $e_p = 512.8 \text{ s}^{-1}$; the peak labeled BB has activation energy $E_a = 0.06 \text{ eV}$ and apparent capture cross section $\sigma_a = 1 \cdot 10^{-17} \text{ cm}^2$, correspondent to those of the shallow level due to B dopant in substitutional position in bulk Si.

DLTS measurements performed with emission rates ranging from $e_p = 46.5 \text{ s}^{-1}$ to $e_p = 465.1 \text{ s}^{-1}$ have yielded spectra (in Figure 4.3-3 a representative spectrum) with no detectable presence of deep defect-related peaks. The peak labeled BB in Figure 4.3-3 exhibits the thermodynamic properties peculiar of the B dopant in bulk Si [4.16, 4.17].

C- DLTS Measurements of Samples from Set II

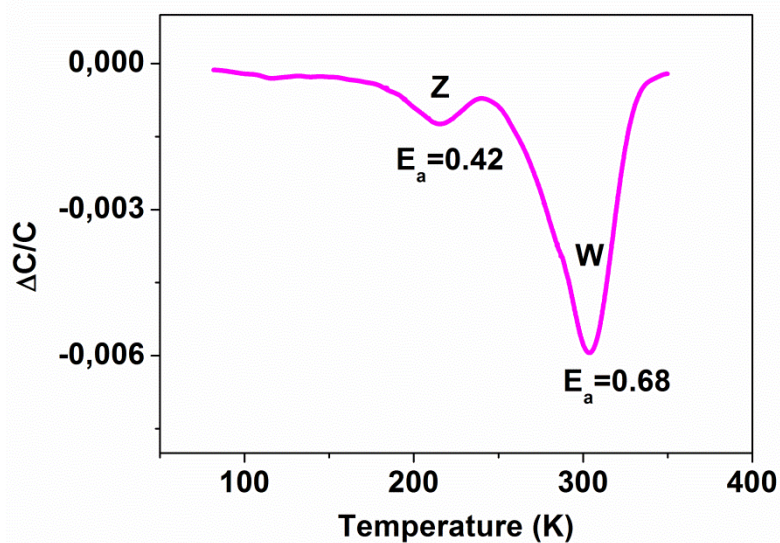


Figure 4.3-4 DLTS spectrum at emission rate $e_p = 46.5 \text{ s}^{-1}$.

DLTS measurements performed with different emission rates (ranging from $e_p = 11.6 \text{ s}^{-1}$ to $e_p = 2325.6 \text{ s}^{-1}$) have yielded spectra with two defect-related peaks labeled W and Z (in Figure 4.3-4 a representative spectrum). Figure 4.3-5 shows the correspondent Arrhenius plot and in table 4-1 are reported their thermodynamic parameters.

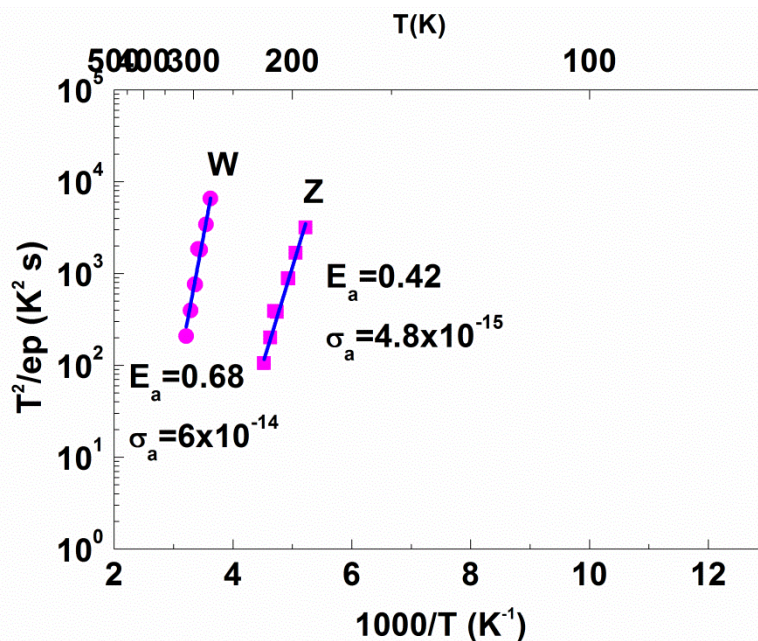


Figure 4.3-5 Arrhenius Plot reporting the signatures of the deep levels W and Z.

C- DLTS Measurements of Samples from Set III

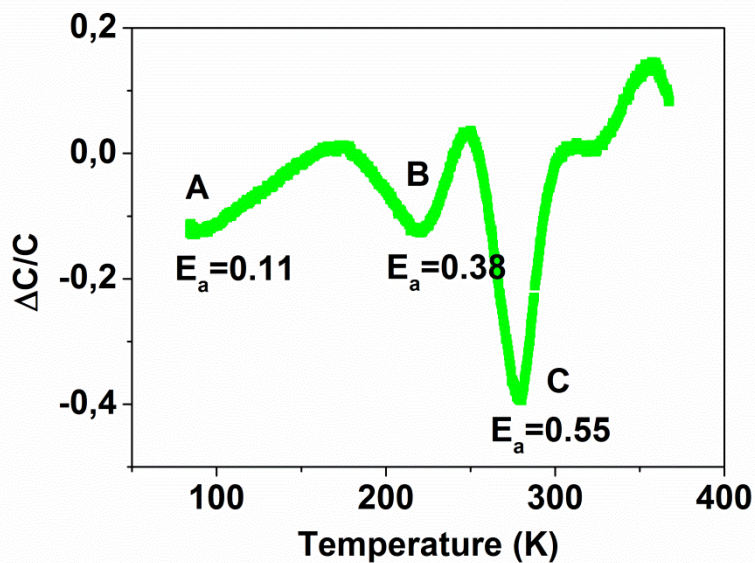


Figure 4.3-6 DLTS spectrum at emission rate $e_p = 46.5 \text{ s}^{-1}$.

DLTS analysis performed with different emission rates (ranging from $e_p = 11.6 \text{ s}^{-1}$ to $e_p = 2325.6 \text{ s}^{-1}$) has yielded spectra with three defect-related peaks labeled A, B, C (in Figure 4.3-6 a representative spectrum). Figure 4.3-7 shows the correspondent Arrhenius plot, whose thermodynamic parameters are reported in table 4-1.

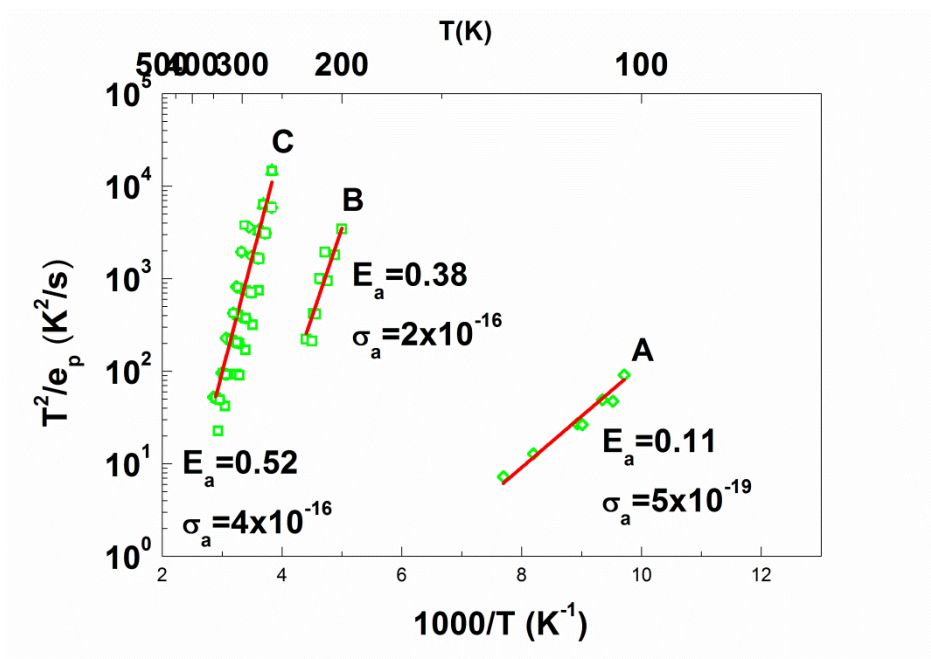


Figure 4.3-7 Arrhenius Plot reporting the signatures of the deep levels A, B, C.

Sample	Deep Level	Enthalpy E_a (eV)	Capture Cross Section σ_a (cm ²)
I	BB	0.06	$1 \cdot 10^{-17}$
II	W	0.68	$6 \cdot 10^{-14}$
II	Z	0.42	$4.8 \cdot 10^{-15}$
III	A	0.52	$4 \cdot 10^{-16}$
III	B	0.38	$2 \cdot 10^{-16}$
III	C	0.11	$5 \cdot 10^{-19}$

Table 4-1 Thermodynamic parameters of the Deep Levels detected in samples I, II, III.

Preliminary Discussion on the DLTS Results and Future Work Plan

DLTS measurements of set I have detected only the presence of the boron level in the Si Substrate, as expected because of the doping. DLTS results of samples from sets II and III show that:

1. both the RIE processed substrate and the Si Grass have been affected from the etching procedure;
2. the deep levels introduced in the samples of sets II and III are different.

The RIE procedure is known to introduce damages in the processed samples (Subsection 4.2) especially in the near-surface region. Even if samples of both sets II and III have been processed in the same way, aside the unbalancing between the passivation and etching steps in samples of set III to induce the Si Grass formation, the produced defects are different in the etched substrate with respect to the Si Grass. This could appear puzzling in the first instance, being the processing substantially the same in both cases. A closer look to the RIE damage literature may help us to advance a first tentative interpretation. In fact, there are at least two main known differences in the RIE damage caused on surfaces and on sidewalls:

- a. because of compensation by removal due to etching, a saturation of the damage occurs on the surface, while the sidewall damage is cumulative in time;
- b. plasma related impurities may be direct implanted or diffuse during RIE, the damage depth being attributed to ions channeling into the material [4.13]. While exponential decay of ion induced defects from the surface downwards

has been proposed for dry etched bulk material, the energetic flux of impinging particles on the sidewalls is absolutely unknown, as consequently the kind of defects distribution under their surface.

Presently work is in progress to identify all the defects related to the detected trap levels of samples of sets II and III.

BIBLIOGRAPHY

- [4.1] P. Blood, J. W. Orton, *The electrical characterization of semiconductors: majority carriers and electron states*, London: Academic Press, 1990.
- [4.2] P. Braunlich Ed., *Thermally Stimulated Relaxation in Solids*, Volume 37 of Topics in Applied Physics. Springer-Verlag, Berlin, Heidelberg, New York, 1979.
- [4.3] E. Meijer, H. G. Grimmeiss, *Semiconductor Science and Technology*, 1992, **7**, 188-197.
- [4.4] D. V. Lang, *Journal of Applied Physics*, 1974, **45**, 3023.
- [4.5] B. Gossick, *Journal of Applied Physics*, 1959, **30**, 8, 1214–1218.
- [4.6] A. H. Bensaoula, A. Bensaoula, A. Freundlich, *Journal of Applied Physics*, 1994, **75**, 2818.
- [4.7] P. D. Wang, M. A. Foad, C. M. Sotomayor Torres, S. Thoms, M. Watt, R. Cheung, C. D. W. Wilkinson, S. P. Beaumont, *Journal of Applied Physics*, 1992, **71**, 3754.
- [4.8] M.A. Foad, S. Thoms, C.D.W. Wilkinson, *Journal of Vacuum Science and Technology B*, 1993, **11**, 20.
- [4.9] D.L. Green, E.L. Hu, P.M. Petroff, Y. Liberman, M. Noony, R. Martin, *Journal of Vacuum Science and Technology B*, 1993, **11**, 2249.
- [4.10] G. A. Northrop, G. S. Oehrlein, *Materials Science Forum*, 1986, **10-12**, 1253.
- [4.11] J. Weber, M. Singh, *Applied Physics Letters*, 1986, **49**, 1617.
- [4.12] G. S. Oehrlein, R. G. Schad, M. A. Jaso, *Surface and Interface Analysis*, 1986, **8**, 243.
- [4.13] A. C. Ford, J. C. Ho, Y. L. Chueh, *Nano Letters*, 2009, **9**, 1, 360-365.
- [4.14] R. Tu, L. Zhang, Y. Nishi, H. Daial, *Nano Letters*, 2007, **7**, 1561-1565.
- [4.15] H. Zhao, R. Kim, A. Paul, M. Luisier, G. Klimeck, F. Ma, S. C. Rustagi, G. S. Samudra, N. Singh, G. Q. Lo, D. L. Kwong, *IEEE ELECTRON DEVICE LETTERS*, **30**, 5, 526-528.
- [4.16] G. L. Pearson, J. Bardeen, *Physical Review*, 1949, **75**, 865–883.
- [4.17] F. J. Morin, J. P. Maita, *Physical Review*, 1954, **96**, 28–35.

PART II

ELECTRON BEAM

INDUCED BENDING

AND

ADHESION DRIVEN

BUNDLING

FOR

NANOSCALED PATTERNING

CHAPTER 5

Electron Beam Induced Bending of MBE Au-Catalyzed Wurtzite GaAs NWs

5.1 The Vapor-Solid-Liquid (VLS) Mechanism and Molecular Beam Epitaxy Method for NWs Growing

5.1.1 The VLS Mechanism

Bottom-Up fabrication of NWs is mostly [5-1] achieved by Chemical Vapor Deposition (CVD) [5-2] or Molecular Beam Epitaxy (MBE) [5-2] methods. In both cases it is operative the Vapor-Solid-Liquid growth mechanism. The classical **adsorption-induced VLS model** [5-3 – 5-5] has been first proposed [5-3] for the CVD **axial growth** of Au-catalyzed Si NWs on Si(111) substrate (Figure 5-1 a)). In it, metal nanoparticles (NPs) are deposited or formed on the substrate surface while the elemental semiconductor atoms are supplied by gaseous precursors. Then the system is heated above the eutectic point temperature of the metal-semiconductor alloy in such a way that the NPs melt and get alloyed. The further impingement of semiconductor atoms from vapors around the NPs make the metal-semiconductor compound supersaturate. The excess semiconductor atoms precipitate to the NP (liquid) / substrate (solid) interface, the latter acting as a sink for them and causing their incorporation into the lattice adsorption sites. This leads to the nucleation of vertical NWs whose diameter is determined by the size of the NPs sitting at the growth fronts.

In the **diffusion-induced VLS model** [5-6, 5-7], aside semiconductor atoms that directly impinge over the NPs, another contribution to NW axial growth derives from atoms adsorbed on the substrate surface or NW sidewalls. For each NW these adatoms diffuse along the concentration gradient of its sidewalls towards the metal NP in order to be therein incorporated. In particular, as regards group III-V NWs,

group III (like Ga) adatoms have larger diffusion length than group V (like As) adatoms, then group V adatoms are believed to be incorporated close to the adsorption sites.

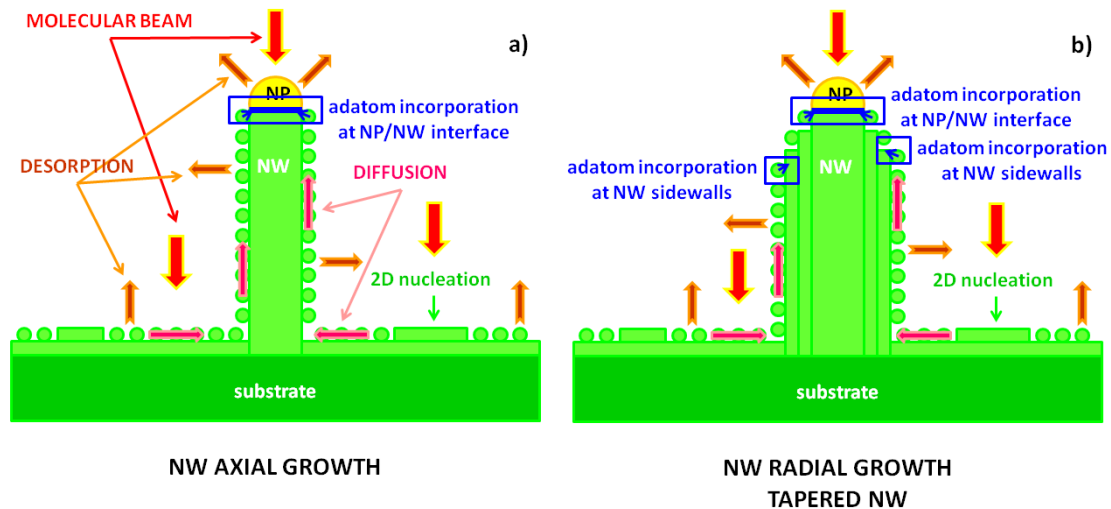


Figure 5.1-1 MBE model of NW growth [5-9]. NW is assumed as being a cylinder of diameter $D=2R$ and length L , the contact angle of drop to be of 90° . The processes on the substrate surface are adsorption, desorption, diffusion, and nucleation. The processes on the NW sidewalls are desorption and diffusion (NW axial growth) and adsorption (NW radial growth). The processes on the NW top are adsorption and desorption on the liquid surface and the vertical growth of the top facet.

NW **radial** (or lateral, or conformal) **growth** occurs when adatoms deposit themselves onto the NW sidewalls following a simple Vapour–Solid (VS) growth mechanism not involving the metal NP [5-8] (Figure 5-1 b)). A competition between axial and radial growths is the result. In case of radial growth, NWs present a distinctive **tapered morphology**: NWs bases are wider than the tips. In fact, the lower regions of NWs experience more radial growth than the higher ones, having been built up first and so exposed for longer time to reactants. Also the NWs bases are nearer to the substrate then they may incorporate a greater fraction of adatoms from it.

5.1.2 NW Growth by MBE

In metal-assisted NW growth by MBE the metal NPs does not act as catalysts to promote the local dissociation of vapor precursors, like in many CVD techniques, since the semiconductor atoms are directly offered by the molecular beams. This could lead in principle to NWs' length comparable to the nominal thickness of the 2D deposited material over the non activated (that is uncovered by metal NPs) substrate surface. However, the experimental evidence shows that MBE NWs always emerge from the substrate. This occurs since in the MBE technique the diffusion length of the adatoms reaches very high values (1–10 μm), in the range or higher

than typical NW lengths. Then, the adatom diffusion from the substrate largely dominates with respect to the direct impingement on the metal NPs or the diffusion from NW sidewalls. The first process is no longer restricted by the deposition rate, that is the maximum NW growth rate is not limited by the deposition rate.

The same explanation has been invoked [5-9] to account for the thinner MBE NW the the longer it is. For CVD NWs is just the opposite, that is the thicker CVD NWs are also the longer ones.

5.1.3 Au-Catalyzed WZ GaAs NWs: Details of the Samples Growth

Two samples of VA GaAs NWs have been grown by Au-assisted solid-source Molecular Beam Epitaxy (MBE) on n-type ($n = 10^{18} \text{ cm}^{-3}$) GaAs (111)B wafers [5.10]. Two samples have been fabricated. The former, labeled A1, is undoped, while the latter, labeled A2, is doped during the growth by coevaporation of Si. The deposition of 0.1 monolayer of Au has occurred at room temperature into a metallization chamber connected in ultrahigh vacuum to the MBE system after thermal deoxidation of the GaAs substrate. Then the NWs have been grown for 60 min at 580°C with an As/Ga beam-equivalent pressure ratio of 12, using Ga flux value such that to yield an equivalent two-dimensional GaAs layer-by-layer growth rate of $1 \mu\text{m} / \text{h}$.

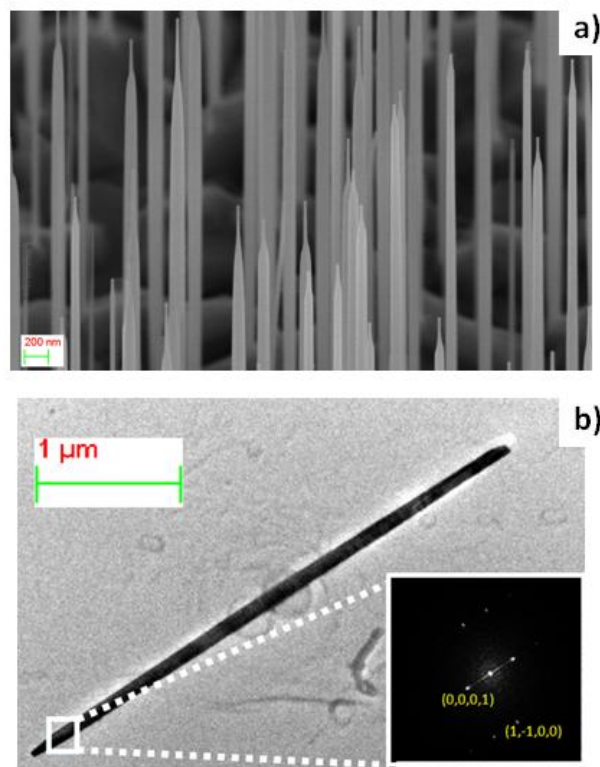


Figure 5.1-2 a) Detail of 45° tilted-SEM image of sample A2, showing the characteristic pencil-like tip. b) Low magnification TEM image of a representative GaAs NW (sample A2), imaged along the $[11\bar{2}0]$ direction; in the inset a diffractogram of the same wire in the tip region showing the WZ structure.

The NWs morphology and their bending/bundling have been studied by Scanning Electron Microscopy (SEM), using a Zeiss SUPRA 40 and a Zeiss LEO 1530 field emission SEMs (FE-SEMs). By SEM investigations the average length and diameter of the NWs result, respectively equal to 5,5 μm and in the order of 90 nm. The NWs morphology shows pencil-like tips (Figure 5.1-2 a), characteristic of the diffusion-induced VLS mechanism, the NW radial growth depending upon the limited diffusion of Ga adatoms on the sidewalls [5.11]. The NWs morphology and their bundling has been investigated also by Atomic Force Microscopy (AFM), by means of a Dimension-3100 AFM with a Nanoscope4 controller from Bruker (Veeco). Finally, structural information has been achieved by transmission electron microscopy (TEM) analyses using a JEOL 2200 with Scherzer resolution of 0.19 nm. For TEM experiments the wires were mechanically transferred from the original substrate onto a carbon-coated copper mesh. Figure 5.1-2 b) shows a representative low magnification TEM image of a NW imaged along the $[11\bar{2}0]$ direction, and a diffractogram of the same wire in the tip region. Except for a few ZB and stacking fault insertions, most of the NW remains WZ along its whole length.

5.2 Electron Beam Induced GaAs NWs Bending: Experimental Observations

The scanning electron microscopy investigation of the Au-catalyzed samples A1 and A2 has revealed that at the beginning of the observations most of the as-grown NWs are vertically aligned (Figure 5.2-1 a). At each raster scanning, the bending of a few GaAs NWs occurs (Figure 5.2-1 b). By increasing more and more the scanning time, the number of NW clusters increases (Figure 5.2-1 c). Figure 5.1-2 c) is a representative SEM micrograph of the sample A2, where NW bundles coexist with VA NWs.

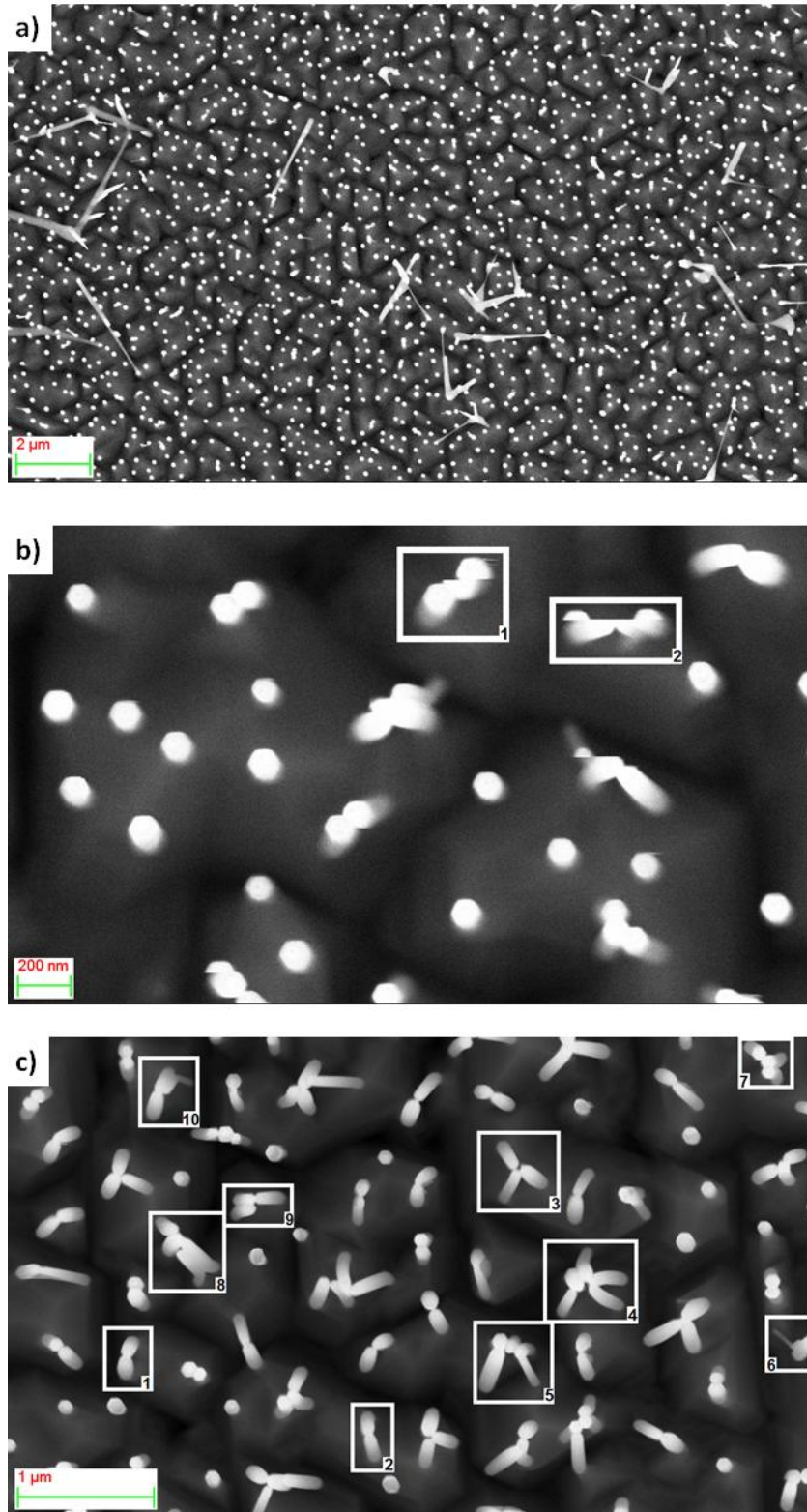


Figure 5.2-1 SEM Plain views of sample A1. a) Original VA NWs. b) The white squares labeled 1 and 2 show typical GaAs NWs bending induced by the electron beam scanning. c) The white squares labeled 1 and 2 show the lateral collapse of couples of GaAs NWs. The white square labeled 3 evidences the occurrence of a triangular configuration. More complex geometries also appear (white squares labeled 4-10). Beam Energy 10 KeV.

5.3 Review of Models for Semiconductor NWs Bending

In the following a brief survey of the existent literature on the topic of NW bending is given.

5.3.1 Self-Attraction Among Aligned Au/ZnO Nanorods Under Electron Beam

VA Au-catalyzed WZ ZnO nanorods [1.47] has been grown by the VLS process over a substrate of α -plane orientated sapphire. Subsequently the nanorods has been observed by SEM operated at 3 KeV. The average diameter has been found of 20 nm, with length ranging from 300 nm to 1 μ m, the largest distance between nanorods about 150 nm. After a short period of observation at SEM it has been reported [1.47] that some nanorods suddenly bent and made contact between each other (Figure 5.3-1 a), b).

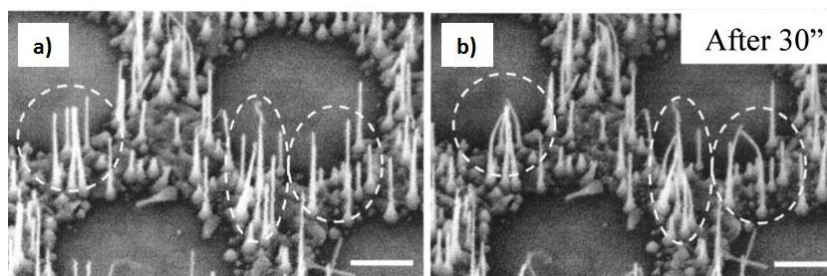


Figure 5.3-1 a) low-magnification SEM image of aligned ZnO nanorods. b), c) 30° side view of self-attraction phenomenon. After X. Wang, C. J. Summers, Z. L. Wang, *Applied Physics Letters*, 2005, **86**, 013111.

The distinguishing features of the phenomenon are:

1. the contact is between the gold tip of one nanorod and the body of another;
2. TEM investigation has revealed that the nanorods sidewalls are $\{01\bar{1}0\}$ facets, nonpolar surfaces in WZ structures;
3. the bunches of nanorods has been found stable upon SEM reexamination after 7 days.

Point 2 of above list excludes the possibility of local dipole moment induced by surface polarization of nanorods facets. A charge redistribution due to the Au-ZnO junction between the metal tip and the semiconductor body of each nanorod has been proposed as an explanation [1.47]. The gold workfunction is of 5.1 eV, while 1D ZnO nanostructures has showed a workfunction of 5.2-5.3 eV [5.12]. The ZnO Fermi energy level is lower than that of gold (Figure 5.3-2a), thus upon Au-ZnO junction formation the electrons flow from Au to ZnO, in order to establish a constant Fermi energy level (Figure 5.3-2b).

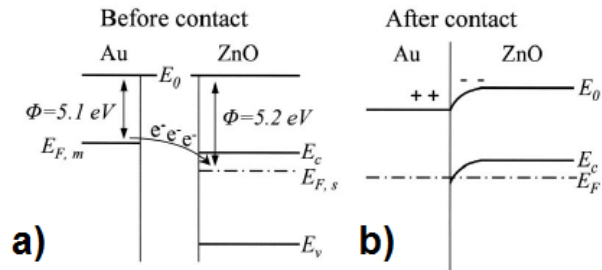


Figure 5.3-2 a), b) Au-ZnO junction band diagram. After X. Wang, C. J. Summers, Z. L. Wang, *Applied Physics Letters*, 2005, **86**, 013111.

The charge redistribution would result in a positively charged Au tip and in a negatively charged ZnO nanorod. The electrostatic forces induced by the Au-ZnO junction barrier would be usually insufficient to overcome the elastic deformation force. The presence of the electron beam has been deemed [1.47] responsible of enhancing the local charge density on both sides of the Au-ZnO junction, and increasing the dipole moment localized at the tip-neck region of the nanorods (Figure 5.3-3).

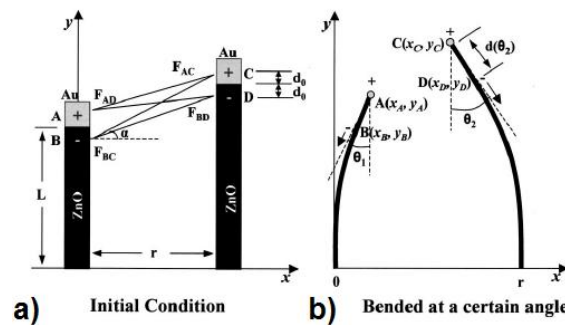


Figure 5.3-3 a), b) Schematic model of the interaction between two ZnO nanorods. After X. Wang, C. J. Summers, Z. L. Wang, *Applied Physics Letters*, 2005, **86**, 013111.

The proposed interpretation [1.47] was supported by point 1 of the above list, that is that all the self-attracting nanorods showed the gold tip (positively charged according to the interpretation) of one nanorods attached to the neck (negatively charged) of another, while no kind of head-to-head or body-to-body contact has been observed.

This model does not apply to GaAs NW samples, as there is experimental evidence of body-to-body contacts between GaAs NWs (see clusters labeled 7-10 in Figure 5.2-1 c), and white stripe labeled 1 in Figure 5.3-4 b). Additionally, the Au-capped heads of

bundled GaAs NWs do not touch any adjacent NW body (Figure 5.3-4 b), where the white arrows point to the Au nanoparticles).

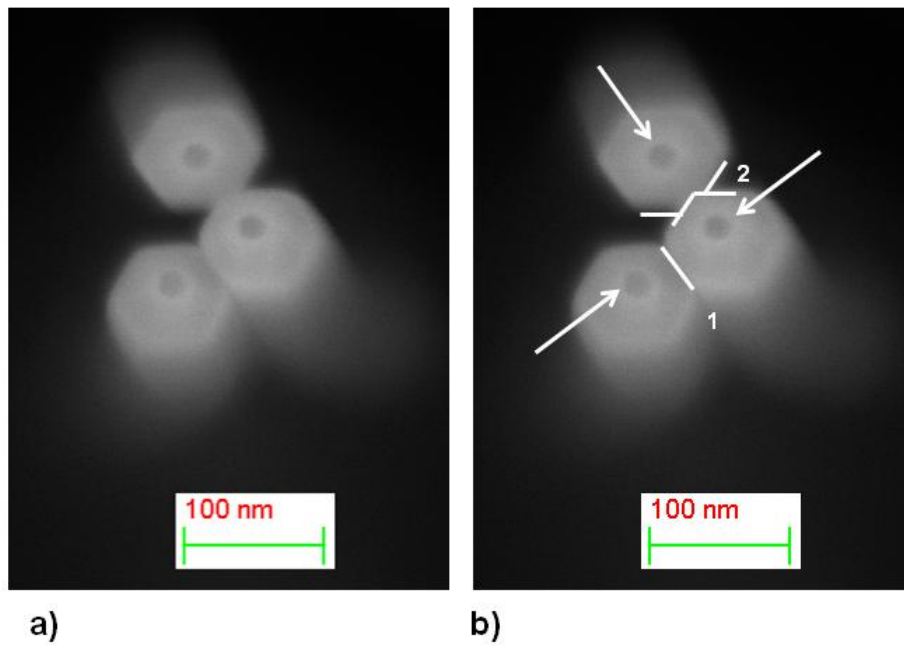


Figure 5.3-4 SEM plain view of a typical NW bundle in sample A1. The micrograph a) shows the SEM image as experimentally obtained, while b) evidences by the white arrows the unbent Au-capped tip of the NWs. White stripes highlight the contact regions between adjacent NWs, which is facet-to-facet (stripe 1) or, in a very unusual way, between the edges (stripes 2). Beam energy 10 KeV.

5.3.2 Bending and Bundling of Metal-Free Vertically Aligned ZnO NWs Due to Electrostatic Interaction

VA WZ ZnO NWs and nanorods [1.48] have been synthesized on silicon substrates without metal catalysts, via a carbothermal reduction process. Samples of different densities and diameters of ZnO nanostructures have been obtained depending on the thickness of the *c*-axis-oriented ZnO seeding layer. In Table 5-I the morphological details of the samples are reported. Also in Table 5-I have been listed the correspondent full range of observed [1.48] bundled configurations.

The distinguishing features of the phenomenon are:

1. no sudden bending and bundling during the electron beam scanning;
2. not only tip-neck contact between NWs;
3. possible indication of repulsive interaction beside than attractive interaction between NWs;
4. evidence for bundling occurring during growth.

Samples	Morphological Characteristics	Bending/Bundling Features
S1, S2	(sample S1) 5- μm long/diameters of size of about 110 nm, or (sample S2) 3,4- μm long and thinner	bundles of few NWs
S3	about 20 μm long and only a few tens of nm thick in their top sections; needle-like tips	no bending/bundling observed
T1	hierarchical 3.5 μm long thin NWs nanorods	most NWs bent and bundled; few isolated NWs; head-head, head-body or body-body contact
T2	hierarchical thin NWs on thick nanorods, but thinner (about 40 nm) and denser than in Sample T1	bundles of more than 10 NWs, no isolated NWs
T3	nanorods of size of about 160 nm	sheet-like materials bridging some of the nanorods as evidence for the occurrence of bundling during growth

Table 5-I Listing of morphological characteristics of the ZnO NWs samples, and correspondent bending and bundling features are reported. After J. Liu, S. Lee, K. Lee, Y. H. Ahn, J.-Y. Park, K. H. Koh, *Nanotechnology*, 2008, **19**, 185607.

Point 1. of the aforementioned list rules out that any electron beam induced charging was responsible for the NW bending, and suggest that the bending occurred during the growth of NWs.

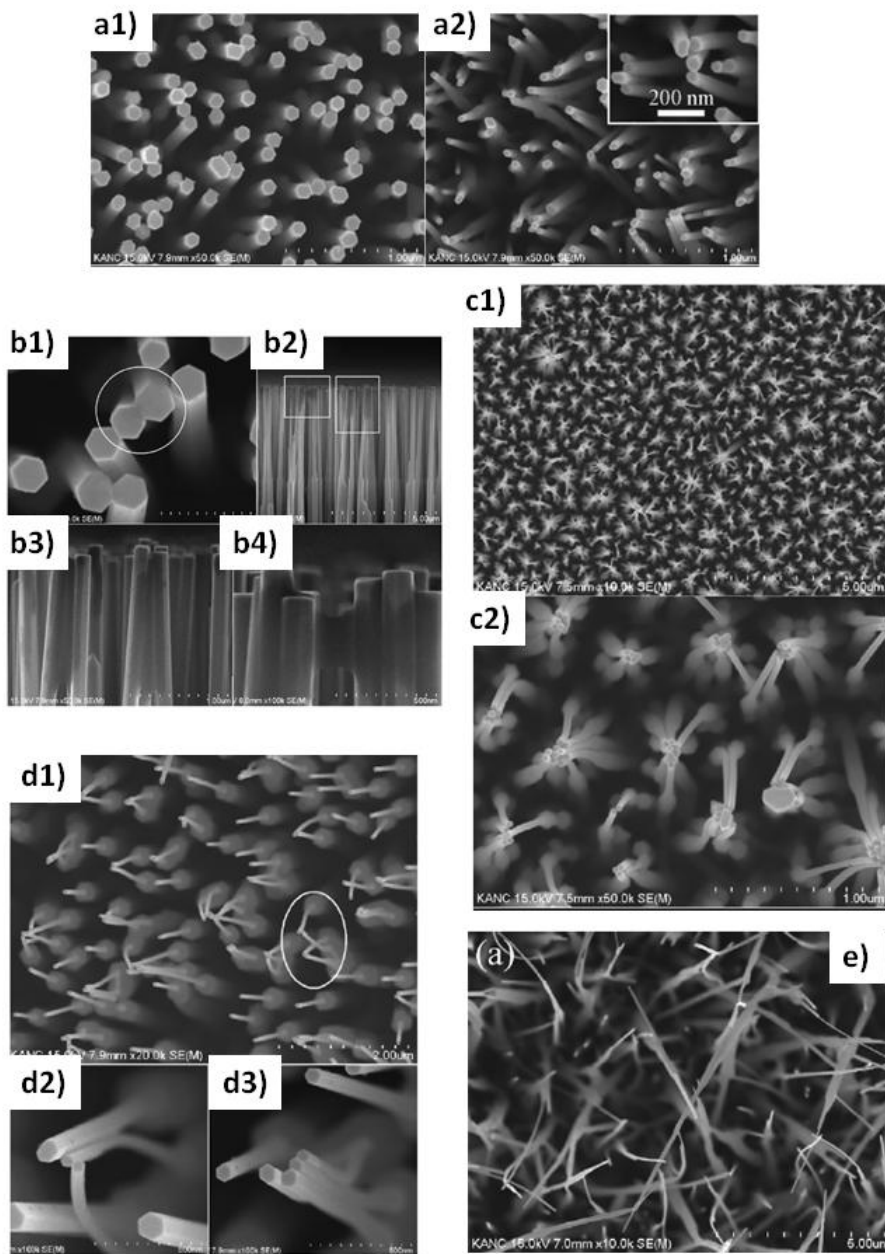


Figure 5.3-5 a1), a2) are plane view of samples S1, S2. b1) – b4) are FE-SEM images of sample T3. ZnO nanorods about 160 nm thick were bundled together. The circle in b1) emphasizes the boundary between two nanorods in contact, indication that the merging occurred during growth; b2) is a cross-sectional image showing that the tops of some bundled nanorods exhibited darker color as marked by rectangles. High-magnification images of such areas show sheet-like structures, either filling the gap among bent nanorods b3) or bridging two thick nanorods about 200 nm apart b4). Plane view images at low (c1) and high (c2) magnifications of sample T2, where it appears that all NWs are bundled together. Tilted view low-magnification image (d1) and high- magnification images (d2) and d3) of various bundling configurations of sample T1. e) is a plane view of sample T3, and no bundling is observed. After J. Liu, S. Lee, K. Lee, Y. H. Ahn, J.-Y. Park, K. H. Koh, *Nanotechnology*, 2008, **19**, 185607.

The proposed interpretation [1.48] has been that observed bundles have arisen due to a combination of effects. The electrostatic interactions between hexagonal top facets with opposite polarities ((0001)-Zn or (-)O) of the WZ ZnO NWs in the first instance. Then a piezoelectric field along and across the WZ NWs has been generated when they have departed from vertical alignment and stuck to each other. Charge redistribution from top polar surfaces to side surfaces should occur to reduce both the strain-induced internal electric field and the external electric field due to surface charges. Finally, the local charges at side surfaces would produce interspace electric fields between NWs and lead to their bending/bundling along their bodies. For the few unbent NWs (Figure 5.3-5 a1), b1), d1)-d3), the electrostatic interaction might have been not large enough to overcome the elastic strain force. Presumably this interspace electric field was responsible for the formation of sheet-like structures (Figure 5.3-5 b1)-b4).

This model does not apply to GaAs NW samples, as they are Au capped (Figure 4.3-4). Moreover there is undisputable evidence of the electron beam role in inducing the NW bending (Figure 5.3-6), while there is no evidence as yet of bending and bundling during growth (Figure 5.2-1 a).

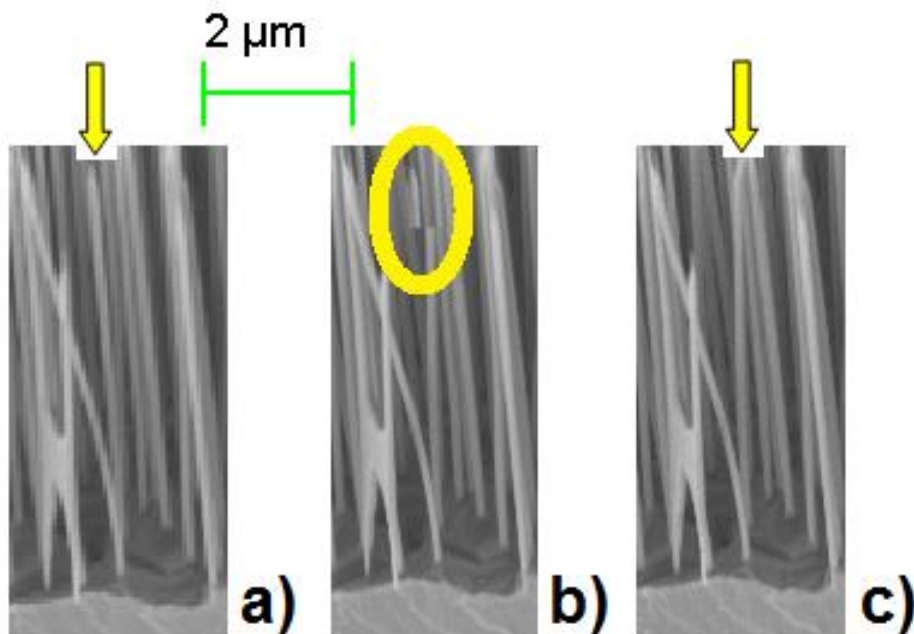


Figure 5.3-6 Sequential order of the micrographs a) → c) of details of SEM images of the zone probed in Figures d, e. They show an originally unbent NW (a), black arrow pointing to his tip) that during the electron-beam scanning snap to contact (see b), white ellipse). c) correspond to the final bundled configuration. Beam energy 3 KeV.

5.3.3 Tailoring the VLS Growth Toward the Self-Assembly of GaAs NW Junctions

Recently the bending and merging between ZB GaAs NWs has been observed, and named **NW kissing** [1.51]. Au catalyzed Metal-Organic Chemical Vapor Deposition (MOCVD) grown GaAs NWs have been fabricated over GaAs (111)B substrates from randomly dispersed Au nanoparticles, where they are expected to maintain the [111] epitaxial relationship with the (111)B GaAs substrate. Systematic observation [1.51] has showed, instead, how the NW kissing occurs in these arrays (Figures 5.3-7a-d), during (in situ) or after (ex situ) growth.

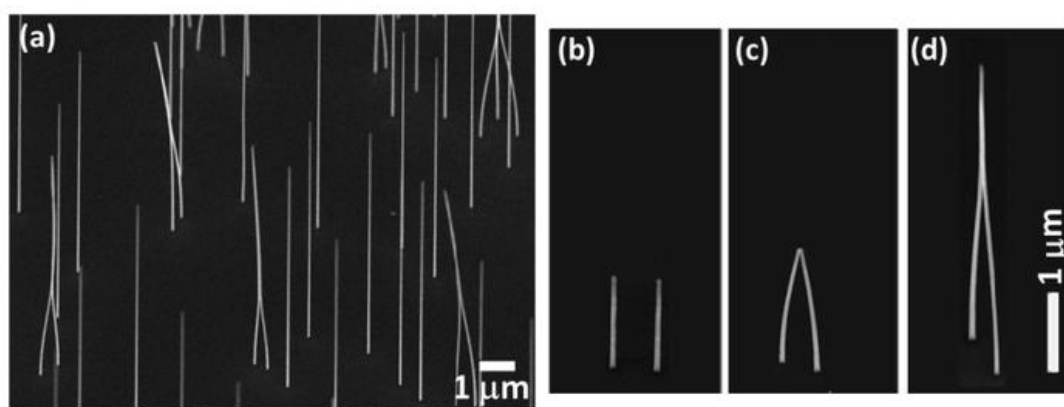


Figure 5.3-7 Nanowire kissing. a) VA GaAs NWs and merged NW bundles coexisting in the same substrate region. Evolution of GaAs NW kissing observed from three individual growth runs with increasingly longer growth times t_g (NW lengths): b) two vertical NWs grow parallel to each other ($t_g = 1$ min); c) NWs bend and kiss ($t_g = 2$ min); and d) NWs merge in a bundle ($t_g = 3$ min). Tilted SEM images obtained at 45° angle. After D. Xing, S. A. Dayeh, V. Veeramuthu, A. Larrue, J. Wang, H. Su, C. Soci, *Nano Letters*, **2011**, 11, 4947–4952.

The distinguishing features of the phenomenon are:

1. coexistence of merged and unmerged NWs in the same growth (Figure 5.3-7 a);
2. the NW bundle formation may happen at any time during or after growth, provided a critical length have been reached by the NWs;
3. the exposure to the electron beam during SEM characterization has also been found to induce the kissing, but not deemed to be the only operating mechanism driving to the bending/bundling;
4. kissing is favored for NWs with smaller diameters and for larger Au NP surface densities (closer NW proximity).

Possible effects related to the electron beam bombardment are electrostatic charging or ablation of the native oxide layer from the exposed NW surfaces, and they have not been ruled out as contributing to the NW kissing. Anyway it has been

deemed [1.51] more likely that the role of the electron beam in the phenomenon be that of forcing oscillations, creating instability that brings two NWs closer until their attraction is favored.

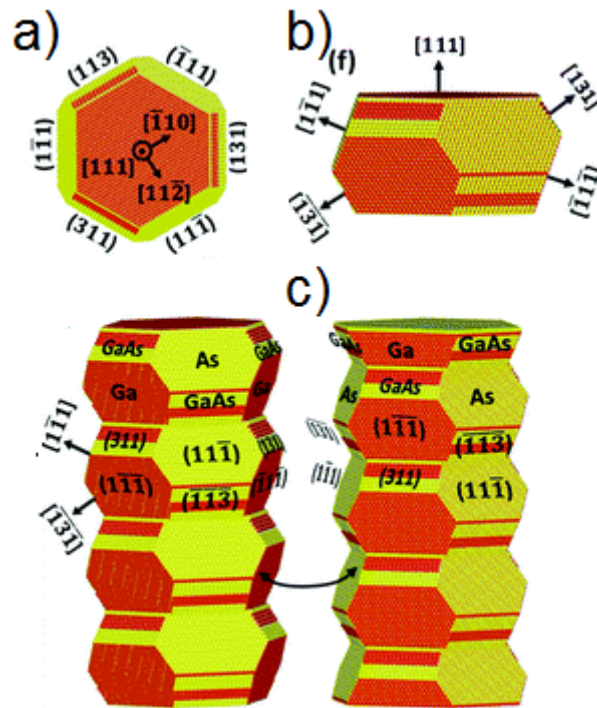


Figure 5.3-8 Atomic model of a GaAs NW grown in the $[111]$ orientation. a) Top and b) side views from a $\langle 110 \rangle$ orientation. c) Adjacent NWs with A and B facets attract each other electrostatically. After D. Xing, S. A. Dayeh, V. Veeramuthu, A. Larrue, J. Wang, H. Su, C. Soci, *Nano Letters*, **2011**, 11, 4947–4952.

High-resolution transmission electron microscopy (HRTEM) characterization has showed that NWs have a ZB crystal structure, with a few stacking fault. Their facets have been found to be oriented in the $\langle 112 \rangle$ direction, with a stepped structure of polar $\{111\}$ and $\{113\}$ planes (Figure 4.3-8). Electrostatic forces acting between these polar surfaces on the two NW facets (Figure 5.3-8 c) have been suggested [1.51] to be the candidates to overcome the NWs mechanical stiffness at the microscopic length scale, while short-range forces have been considered negligible.

This model does not apply to GaAs NW samples even if the bending and subsequent bundling between the sidewalls of neighbor NWs occur (Figure 5.3-4 b), white stripe 1). In fact, the TEM characterization has evidenced that the Au-catalyzed GaAs NWs have prevalent WZ structure, especially in the NW region close to the tip (Figure 5.1-2 b). That is the NWs are hexagonal prism shaped with six sides, these surfaces being non polar [5.13]. Therefore, the NW bending cannot be attributed to a local dipole moment generated by a possible surface polarization.

5.4 Mechanism of Nanostructure Movement Under an Electron Beam

Scanning electron beam microscopy is a common tool for material characterization. When using it, it may happen that injected charges yield undesirable effects, like locally altering the material properties or causing local changes of the sample features. Features displacement induced by the electron beam has been reported for decades and has been considered as a limiting factor both for obtaining high-resolution images [5.14] as well as for electron beam writing.

Some attempts have been made to explain this phenomenon. Pressures inside the structures generated by photolytically initiated solid-state chemical reactions [5.15], shrinkage of surfaces [5.16] and surface charging on thin films with one conducting layer [5.17] have been proposed as possible causes. Recently, an electrostatic model has been devised and experimentally tested [1.78].

5.4.1 Experimental Observations

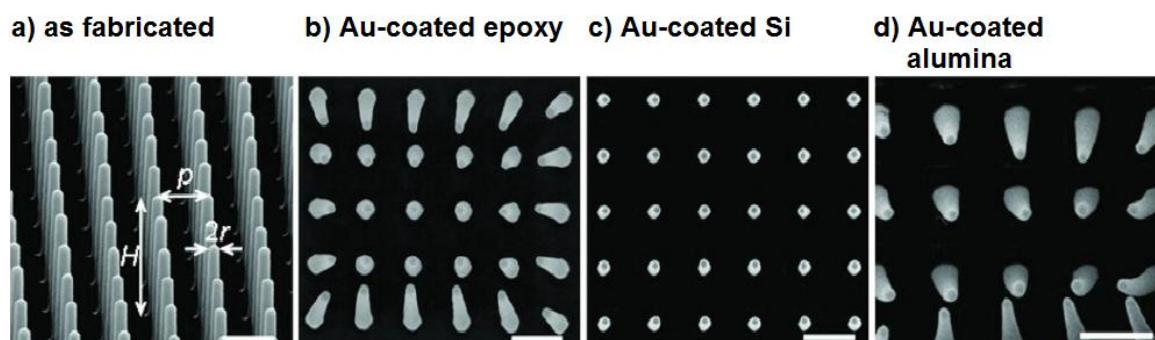


Figure 5.4-1 a) As fabricated epoxy nanopillar array b) gold-coated epoxy nanopillar array after about 1 to 5 s of scanning. c) gold-coated silicon nanopillar array after about 10 to 15 s of scanning. d) gold-coated alumina nanopillar array after about 10 to 15 s of scanning. Scale bars $2 \mu\text{m}$.

After A. Seminara, B. Pokroy, S. H. Kang, M. P. Brenner, J. Aizenberg, *Physical Review B*, 2011, **83**, 235438.

Arrays of cylindrical nanopillars protruding from substrates (Figures 5.4-1 a) of height H and radius r have been fabricated from various materials and coated with gold or carbon. Then the samples have been inserted into the SEM chamber, grounded, and characterized [1.78]. As regards Au-coated epoxy resin samples, after few seconds of scanning at high magnification the pillars have been seen to bend (Figure 5.4-1 b).

The distinguishing features of the phenomenon are [1.78] (Figure 5.4-1 b):

1. the bowing of the nanopillars is negligible near the center of the scanned region;
2. the maximum bending is located at the periphery of the scanned region;
3. the nanopillars are deflected towards the center of the scanned region.

The described pattern is reproducible and persists over several seconds before the nanopillars relaxing back to the original VA position, as shown by imaging a larger area. The scanning was repeated at different beam energies (1–30 KeV) and beam currents (10–150 pA), and it has been found [1.78]:

4. increasing bending with increasing current;
5. not monotonic dependence of bending with beam energy; maximum bending is recorded at 5 KeV.
6. The bending strongly depends on the material of which the nanopillars are made of: (keeping the same geometry of the array)
 - n-doped Si nanopillars have showed no bending (Figure 5.4-1 c);
 - alumina nanopillars have bowed (Figure 5.4-1 d).

This latter point (see also Table 5.II) rules out the possibility that the lack of bending of Si nanopillars be related to their mechanical stiffness, rather suggesting it is due to their not insulating electrical character. This leads to hypothesis of the electrostatic interaction being responsible of the electron beam induced deflection of the nanopillars.




Material	Relative Permittivity ϵ_r	Bending Modulus E (GPa)	Conductivity K ($\Omega^{-1}\text{m}^{-1}$)	Relaxation Time Scale τ (s)	Bending
epoxy	2.3	2	10^{-11}	≥ 2	
silicon	11.7	100	10^{-4}	10^{-8}	
alumina	9.6	300	10^{-12}	80	

Table 5-II – Material properties and experimental results for all the tested arrays.

5.4.2 Theoretical Model for Electron Charge Implantation

Let us consider a single nanopillar of height H and radius r , and an electron beam in spot mode impinging, with incoming current I , at a distance a from the nanopillar (Figure 5.4-2).

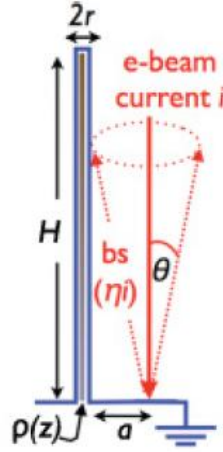


Figure 5.4-2 Schematic geometry of the electron beam impinging in the nearby of the nanopillar. After the electron beam (current I) impacts the specimen, electrons are backscattered, with backscattering coefficient η and backscattering angles θ . After A. Seminara, B. Pokroy, S. H. Kang, M. P. Brenner, J. Aizenberg, *Physical Review B*, 2011, **83**, 235438.

After hitting the nanopillar, electrons are back scattered, with backscattering coefficient at primary impact η , at an angle θ relative to the beam direction with probability $P(\theta) = \cos \theta$ [5.18]. The total current per unit height colliding on the nanopillar at distance z from the substrate surface is:

$$I_n(z) = \eta(1 - \eta_n) \frac{r}{\pi a} P(z) I \quad (5.1)$$

$$P(z) = P(\theta) \left| \frac{d\theta}{dz} \right| = \frac{az}{(a^2 + z^2)^{3/2}} \quad (5.2)$$

where $\frac{r}{\pi a}$ is the fraction of electrons impacting the nanopillar. $1 - \eta_n$ is the fraction of implanted electrons after further backscattering, with backscattering coefficient at impact with nanopillar $\eta_n = \eta_n(\theta)$. The charge builds up according to the following law:

$$\dot{\lambda} = I_n - \frac{\lambda}{\tau} \quad (5.3)$$

set that $\lambda(z, t)$ is the charge per unit height deposited at z , $\tau \sim \frac{\epsilon}{K}$ is the charge relaxation time, K is the conductivity, $\epsilon = \epsilon_0 \epsilon_r$ is the permittivity. Under steady state conditions, Equation (5.3) yields:

$$\lambda(z) = I_n(z)\tau \quad (5.4)$$

The magnitude of λ and the time scale over which this steady-state charge is accumulated strongly depends on the material properties (see Table 5.II). Monte Carlo simulations [1.78] (Figure 5.4-3) has allowed the estimation of the backscattering coefficients. The simulation has provided the probability of backscattering, that is the fraction of electrons that backscatter and penetrate. The same procedure has yielded η_n , where both the electrons that either backscatter at the impact with the nanopillar or cross the thin nanopillar and leave the sample from the other side have been included.

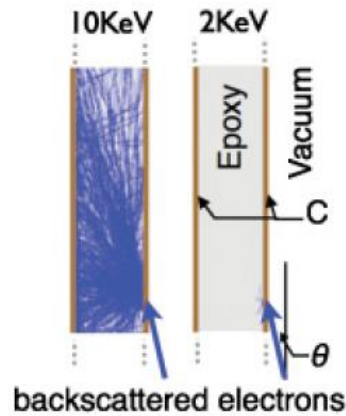


Figure 5.4-3 Monte Carlo simulation of trajectories of electrons impacting the nanopost at $\theta = 30^\circ$ for different energies (10 KeV on the left, 10 KeV on the right). The trajectories of 10 KeV-electrons are straight lines, meaning that they pass through the nanopillar. At 2 KeV they do not have enough energy to penetrate the nanopillar. After A. Seminara, B. Pokroy, S. H. Kang, M. P. Brenner, J. Aizenberg, *Physical Review B*, 2011, **83**, 235438.

The simulations have been repeated at different beam energies. Depending on their energies, electrons travel different depths in the nanopillar, spanning from energies ≤ 2 KeV, when the electrons don't even penetrate the nanopillar, till ≥ 10 KeV, when the electrons pass through the nanopillar. Maximum charge deposit in the nanopillars is reached when electrons have enough energy to penetrate it without escaping, and this explain the experimental evidence [1.78] of an intermediate optimal energy for the nanopillar bending.

Simple considerations suggest that the implanted charge distribution is not uniform in the nanopillar. The existence of an energy barrier $\Delta E \sim 2$ KeV associated with the interfaces means that electrons which reach the outer interface with energy ≤ 2 KeV are decelerated and do not leave the nanopillar. Then, charge distribution is expected to be biased toward the side of the nanopillar opposite to the electron impact.

5.4.3 Theoretical Model for Electrostatically Driven Bending

The detailed charge distribution cannot be found by current experiments or simulations. Let us assume that the non-uniform distribution of $\lambda(z)$ be centered at a distance x_c from the axis of the nanopillar, x_c allowed to assume both positive or negative values, corresponding to charge accumulating toward the inner or outer side of the nanopillar, that is the nanopillar side exposed to electrons flow or not. From the above argument, $x_c < 0$ is expected [1.78].

The electrostatic equilibrium problem coupled to the mechanical bending has to be solved in order to get the nanopillar deflections in the same range as the experiments. The equilibrium electrostatic potential is obtained by solving the Poisson equation:

$$\nabla^2 \phi = -\frac{\rho}{\epsilon} \quad (5.5)$$

on the domain showed in Figure 5.4-4. The implanted charge density $\rho(z)$ is distributed in a cylinder of cross section l^2 centered at a distance x_c from the nanopillar axis, so that $\rho(z) = \frac{\lambda(z)}{l^2}$.

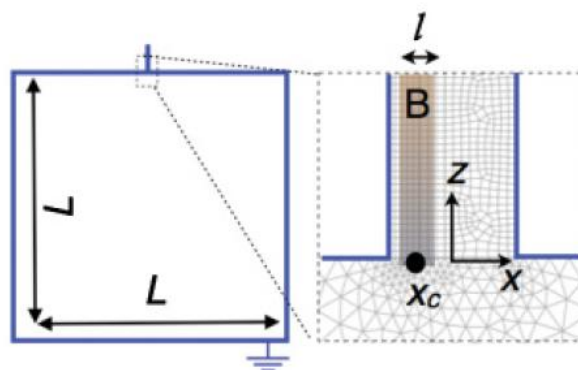


Figure 5.4-4 Domain of integration of Poisson equation and magnification of the base of the nanopillar, showing the mesh in the substrate and in the nanopillar. The shaded area is charged with $\rho(z) = \frac{\lambda(z)}{l^2}$. After A. Seminara, B. Pokroy, S. H. Kang, M. P. Brenner, J. Aizenberg, *Physical Review B*, 2011, **83**, 235438.

The electrostatic force per unit length

$$\vec{w} = \int_S \rho \vec{E} d^2x + r(\sigma^- \vec{E}^- + \sigma^+ \vec{E}^+) \quad (5.6)$$

and the torque per unit length

$$\vec{N} = \int_S \rho \vec{E} \times \vec{x} d^2x \quad (5.7)$$

of the nanopillar can be computed from the action of the electric field $\vec{E} = -\vec{\nabla}\varphi$ on the static charge ρ and the induced surface charge $\sigma = \epsilon \cdot \vec{E} \cdot \hat{n}$, \hat{n} being the unit vector orthogonal to the coated surface, S the nanopillar surface area, \vec{x} the distance from the center of the nanopillar, the superscripts +/- indicating the nanopillar exposed/unexposed side to the electron beam.

The nanopillar bending is obtained by the equation for small bending of thin rod [5.19]:

$$\frac{d\vec{F}}{dz} = -\vec{w} \quad (5.8)$$

$$\frac{d\vec{M}}{dz} \equiv -EI \frac{\partial^2 \vec{u}}{\partial z^2} = -\vec{N} - \hat{z} \times \vec{F} \quad (5.9)$$

\vec{F} being the shear force, \vec{M} the bending moment, set that $\vec{u} \equiv u\hat{x}$ is the displacement of the center axis, E is the Young's modulus, $I = \frac{\pi r^4}{4}$ is the area moment of inertia.

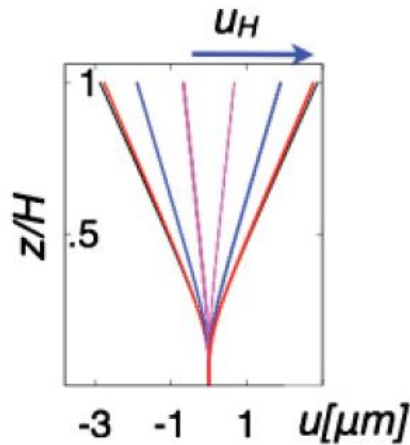


Figure 5.4-5 Simulation of carbon-coated nanopillar at maximum bending for different values of x_c between $-r$ (right) and r (left). After A. Seminara, B. Pokroy, S. H. Kang, M. P. Brenner, J. Aizenberg, *Physical Review B*, 2011, **83**, 235438.

The calculations predict that the nanopillars bend inward when $x_c < 0$, i.e. when the charge accumulates towards the outer side of the nanopillar. Given that the only observed bending is inward for grounded samples [1.78], the conclusion is that the charge accumulates towards the electron beam exposed side of the nanopillar, as already intuitively suggested. It is worth noting that to reach the steady-state charge (5.4), current must flow to the ground until the amount of charge that is implanted in each portion of the nanopillar I_n equals the amount of charge $\frac{\lambda}{\tau}$ that flows to the ground through the coating.

The theory on the bending of a single nanopillar is sufficient to explain the patterns observed in scanning mode [1.78] (Figure 5.4-1). Nanopillars on the edges are only exposed to the electron beam from the inside of the scanned area, and similarly to the case of an isolated nanopillar the electrons accumulate towards the opposite side of the nanopillar yielding maximum inward bending. For nanopillar located near the center of the scanned region, since they receive about the same number of backscattered electrons from all directions, then $x_c \sim 0$ and no bending is expected.

Since the implanted charge is proportional to τ , the model also explains why a gold-coated silicon nanopillar do not deflect under electron beam (Figure 5.4-1 c) while gold-coated alumina one does (Figure 5.4-1 d). The theory also shows that the nanopillar actuation does not require interaction between nanopillars. Thus an isolated nanopillar is expected to be deflected by the electron beam, and this fact has been experimentally verified [1.78] (Figure 1.3.4 a). Moreover if the electron beam is focused in the center of nanopillar this latter is left unmoved (Figure 1.3.4 b).

Finally, the direction of nanopillar deflection is expected to be reversible. If the samples are ungrounded, then the charge in the coating is determined not only by the electrostatic induction, but the magnitude and sign of the charge in the coating should also depend on secondary emission (SE) [5.20]. A switch in the sign of the charge in the coating may then reverse the electric field inside the nanopillar, thus yielding outward bending. Direct numerical simulations of the ungrounded case are not possible, anyway it is expected that materials with very different secondary yields may behave in opposite ways. Experimentally [1.78], upon removing the ground, the gold-coated samples (SE coefficient 0.7; Figure 1.3.4 c) show inward bending whereas carbon-coated samples (SE coefficient 0.05; Figure 1.3.4 d) show outward bending. These results rule out the possibility that thermal expansion or electromagnetic forces are the mechanism causing the bending.

This model does not apply to GaAs NW samples. First, the electron beam induced pattern are very different. We have experimental evidence that the electron beam induced NW bending may occur both to the periphery of the scanned area as well as to its center, and that NWs bend towards the center as well as far away from it (Figures 5.2-1 b), c). Second, the deflection in GaAs NWs has been induced by electron beams with energy ranging from 3 KeV to 10 KeV, and for both samples A1 and A2 (doped and undoped) with different conductivities, then different relaxation time scales. Last, the bending of a single GaAs NW has never been observed, as yet.

5.5 Proposed Mechanism Inducing GaA NWs Bending

To explain the GaAs NWs bending, we may start by considering the phenomena taking place in SEM-related experiments currently used in the investigation of semiconductor materials and microstructures [5.21], such as Electron-Beam-Induced Current (EBIC) [5.22, 5.23] and Surface Electron Beam Induced Voltage (SEBIV) [5.25–5.27]. Both EBIC and SEBIV methods rely on the generation of non-equilibrium charge carriers by the SEM electron probe, which are separated at electrical barriers occurring in the device under test such as $p-n$ junctions or near surface Space Charge Regions (surface-SCR). When the two sides of the electrical barrier are connected via an external load resistor, the electron beam induces a current in the circuit (EBIC mode). When the circuit is open, the electron-beam induces a voltage (SEBIV).

In the case under study, the device under test corresponding to each GaAs NW, connected to the grounded GaAs substrate, is open. During the SEM scanning of the NW array surface, when the electron beam impinges on a NW, it generates electron-hole pairs that may be separated at the NW surface-SCR. If the carrier generation is followed by the net charge redistribution [5.28], a potential drop across the surface-SCR occurs, hence the surface potential locally changes. Other effects that might affect the surface potential are the non-uniform generation or recombination within

the NW internal region, the presence of interfaces within the NW, the electron beam induced changes in NW surface or internal region.

The SEBIV effect may, then, induce a difference in the surface potential of two next-neighbor electron beam scanned NWs, if some of the factors listed above varies from one NW to another. This difference in surface potential leads to the rising of electrostatic forces between NWs that consequently bend. Besides, the bending of WZ NWs induces a spontaneous polarization. All these factors would, finally, cause the mechanical collapse of two or several NWs.

Something similar happens in the field of micro-/nano-electromechanical systems (MEMSs/NEMSs), in which micro-switches are an essential operational component. A typical microswitch is constructed from two conducting electrodes, one electrode usually clamped to one end and the other end able to move. By applying a voltage difference between the two electrodes, the mobile electrode moves towards the fixed electrode under electrostatic attraction. At a threshold voltage the mobile electrode becomes unstable and collapses, or pulls in, on the fixed electrode. This phenomenon is widely investigated for electrostatic micro-actuators, at micro- and sub-micron scale separations [5.29-5.32], from the fundamental physics point of view as well as for the technological implications.

BIBLIOGRAPHY

- [5-1] V. G. Dubrovskii, N. V. Sibirev, G. E. Cirlin, J. C. Harmand, V. M. Ustinov, *Physical Review E*, 2006, **73**, 021603.
- [5-2] W. S. Rees Jr. (Ed.), *CVD of Nonmetals*, VCH Publishers, Inc., New York, 1996.
- [5-3] R. S. Wagner, W. C. Ellis, *Applied Physics Letters*, 1964, **4**, 89.
- [5-4] E. I. Givargizov, *Journal of Crystal Growth*, 1975, **31**, 20.
- [5-5] E. I. Givargizov and A. A. Chernov, *Kristallografiya*, 1973, **18**, 147.
- [5-6] J. M. Blakely and K. A. Jackson, *Journal of Chemical Physics*, 1962, **37**, 428.
- [5-7] V. Ruth and J. R. Hirth, *Journal of Chemical Physics*, 1964, **41**, 31.
- [5-8] H. J. Joyce, Q. Gao, H. H. Tan, C. Jagadish, Y. Kim, J. Zou, L. M. Smith, H. E. Jackson, J. M. Yarrison-Rice, P. Parkinson, M. B. Johnston, *Progress in Quantum Electronics*, 2011, **35**, 23–75.
- [5-9] V. G. Dubrovskii, G. E. Cirlin, I. P. Soshnikov, A. A. Tonkikh, N. V. Sibirev, Yu. B. Samsonenko, V. M. Ustinov, *Physical Review B*, 2005, **71**, 205325.
- [5.10] M. Piccin, G. Bais, V. Grillo, F. Jabeen, S. De Franceschi, E. Carlino, M. Lazzarino, F. Romanato, L. Businaro, S. Rubini, F. Martelli, A. Franciosi, *Physica E*, 2007, **37**, 134–137.
- [5.11] V. G. Dubrovskii, N. V. Sibirev, G. E. Cirlin, M. Tchernycheva, J. C. Harmand, V. M. Ustinov, *Physical Review E*, 2008, **77**, 1–7.
- [5.12] H. J. Joyce, Q. Gao, H. Hoe Tana, C. Jagadish, Y. Kim, J. Zou, L. M. Smith, H. E. Jackson, J. M. Yarrison-Rice, P. Parkinson, M. B.ohnston, *Progress in Quantum Electronics*, 2011, **35**, 23–75.
- [5.13] X. D. Bai, E. G. Wang, P. X. Gao, Z. L. Wang, *Nano Letters*, 2003, **3**, 1147.
- [5.14] R. Henderson and R. M. Glaeser, *Ultramicroscopy*, 1985, **16**, 139.
- [5.15] R. M. Glaeser, *Journal of Structural Biology*, 2008, **163**, 271.
- [5.16] T. I. Kim, H. E. Jeong, K. Y. Suh, H. H. Lee, *Advanced Materials*, 2009, **21**, 2276.
- [5.17] R. M. Glaeser, K. H. Downing, *Microscopy and Microanalysis*, 2004, **10**, 790.
- [5.18] J. I. Goldstein, D. Newbury, D. C. Joy, C. E. Lyman, P. Echlin, E. Lifshin, L. Sawyer, J. R. Michael, *Scanning Electron Microscopy and X-ray Microanalysis 3rd Edition*, Plenum, New York, 1992.
- [5.19] L. Landau and L. Lifshitz, *Theory of Elasticity*, Addison-Wesley Reading, MA, 1959.
- [5.20] J. D. Jackson, *Classical Electrodynamics*, Wiley, New York, 1962.

- [5.21] D. B. Holt, D. C. Joy, *SEM Microcharacterization of Semiconductors*, Academic Press, New York, 1989.
- [5.22] H. J. Leamy, *Journal of Applied Physics*, 1982, **53**, 6, R51–R80.
- [5.23] E. B. Yakimov, *Izvestiya Rossijskoj Akademii Nauk, Seriya Fizicheskaya*, 1992, **56**, 3, 31–44.
- [5.24] V. I. Petrov, *Uspekhi Fizicheskikh Nauk*, 1996, **166**, 8, 859–871.
- [5.25] Gostev, A.V., Kleinfel'd, Yu.S., Rau, E.I., and Spivak, G.V., *Mikroelektronika*, 1987, **16**, 4, 311–319.
- [5.26] E. I. Rau,, N. N. Sedov,, H. Wenguo, Z. Shiqiu, *Poverkhnost'*, 2000, **2**, 4–9.
- [5.27] A. L. Obukhov, E. I. Rau, H. Rait, *Izvestiya Rossijskoj Akademii Nauk, Seriya Fizicheskaya*, 1992, **56**, 3, 170–175.
- [5.28] L. Kronik, Y. Shapira, *Surface Science Reports*, 1999, **37**, 1-206.
- [5.29] P. M. Osterberg, D. Senturia *Journal of Microelectromechanical Systems*, 1997, **6**, 107.
- [5.30] H. Sadeghian, G. Rezazadeh, P. Osterberg, *Journal of Microelectromechanical Systems*, 2007, **16**, 1334.
- [5.31] R. C. Batra, M. Porfiri, D. Spinello, *Smart Materials and Structures*, 2007, **16**, R23.
- [5.32] W. H. Lin, Y. P. Zhao, *International Journal of Nonlinear Sciences and Numerical Simulation*, 2008, **9**, 175.

CHAPTER 6

MBE Au-Catalyzed Wurtzite GaAs NWs Bundling as a Case of Adhesion-Driven Lateral Collapse

6.1 Physics and Mechanics of Contact and Adhesion of Fibrillar Interfaces

6.1.1 The Gecko Effect

Animals such as lizards and insects have evolved interfaces in order to meet the joint needs for locomotion and adhesion [1.52]. These requirements appear as imposing contradictory constraints over such surfaces, since they imply the ability to stick well-enough but also the easiness of removal. The answer to this complex issue has been answered during biological evolution with the development of a class of interfaces which share in common the hierarchical fibrillar design [6.1]. In Figure 6.1-1 it is showed the fibrillar structure of a Gecko feet skin.

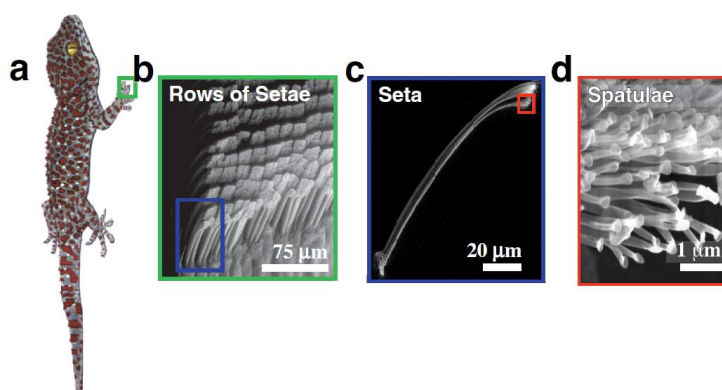


Figure 6.1-1 – Hierarchy of structure in the gecko toe attachment system. After K. Autumn, Y. A. Liang, S. Tonia Hsieh, W. Zesch, W. P. Chan, T. W. Kenny, R. Fearing, R. J. Full, *Nature*, 2000, **405**, 681–684.

The features composing the hierarchical architecture range in scale from nanometers to millimeters, and they are broadly grouped in two classes: the fibrils, termed setae, which typically end with a thin-plate-like contact surface, dubbed the spatula, and the continuous film. In lizards, as an example, the material composing the structure is keratinous, a stiff glassy polymer. In insects, the material is a chitin composite, likewise a stiff glassy polymer. The wonder of these natural structures is that they are capable of adhesion to a remarkable variety of surfaces, they are re-usable, anisotropic, self-cleaning, flaw-tolerant, and compliant at the contact interface. Given that they rely on non-specific inter-surface interactions, their functionality resides essentially in the basic (generic) materials and in the fibrillar structure geometry.

It seems natural to define as fastener any attachment mechanism based on macro-scale structures, that is with characteristic lengths ranging few hundred of microns or larger, while in adhesives the attachment is due to bonds or intermolecular interactions between surfaces at the molecular length scale. Then a natural fibrillar surface lies somewhere between adhesives and fasteners, since it is an interface that mediates interactions between a body and an external surface using a combination of intermolecular forces and structures neither at the molecular scale nor at the macro-scale.

The natural fibrillar architectures represent one proof-of-existence example of how useful surface properties may be achieved by appropriately structuring the surface. The field of bio-mimetic and bio-inspired structured surfaces has seen explosive interest recently. It encompasses biological studies of the natural surfaces, fabrication and testing of bio-mimetic and bio-inspired synthetic structures, and theory both to understand the natural systems and to model and design synthetic mimics. Because most of the work either derives or attempts to relate directly back to the fibrillar structures of the gecko, the entire field is now currently associated with the term of **gecko effect**.

6.1.2 Adhesion of Bio-Mimicked and Bio-Inspired Artificial Single-Level Fibrillar Structures: Some Theoretical Considerations

The most simple, idealized architecture which models both theoretically than experimentally a natural fibrillar surface is made of an array of micro-pillars (fibrils) protruding from a substrate (Figure 6.1-2). Each pillar is characterized by its Young's modulus E , moment of inertia I , length h and squared cross sections of side $2a$. The pillars are at a distance of $2w$ from each other. An approximate analytical model [1.55] for the adhesion of such a surface is developed by applying the basic principles of elastic beam theory, surface interaction forces, and contact mechanics.

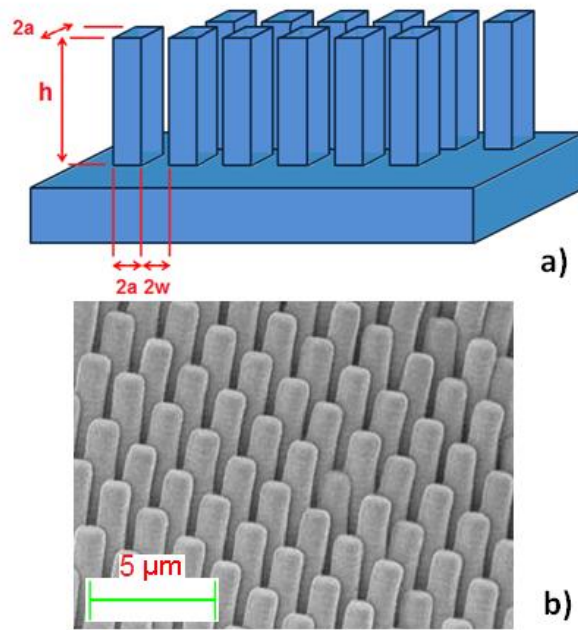


Figure 6.1-2 a) Schematic model of fibrillar structure. b) Fabricated fibrillar structure by molding PDMS into silicon master with ion-etched holes.

The ability of a surface to conform to other surfaces with increasing roughness, for the same given applied load, is raised by the lowering of its Young modulus, a well known part of the mechanism over which rely on pressure-sensitive adhesives. By contrast, fibrillar interfaces compliancy to surface contact may be good even when they are composed of stiff material, because of bending and micro-buckling of their fibrils. In fact, for such structures, the microbuckling makes them very compliant compared to the pre-buckled state.

Let us start with single fibril stress–strain analysis [1.55]. Based on classical Euler buckling [6.2, 6.3], for a uniform applied stress, micro-buckling occurs when the force normal to the fibril exceeds the critical value F_{cr} :

$$F_{cr} = b_c \frac{\pi^2 E^* I}{h^2} \quad (6.1)$$

where $E^* = E/(1 - \nu^2)$ is the plane strain fibril modulus, ν is Poisson's ratio and b_c is a factor of the order of unity that depends on boundary conditions, $b_c \sim 2$ and for pinned–clamped micro-beams. Equation (6.1) is valid only for a fibrils whose lateral surface is normal respect to its basis.

Let us now consider a fibrils that protrude from the substrate at an angle other than $\pi/2$. Assuming the contact force F is normal to the substrate, its components along

and tangential to the direction of the fibril, $F \cos \theta$ and $F \sin \theta$, give rise to bending and compressive deformations, δ_b and δ_c , whose values are [6.4]:

$$\delta_b = \frac{F \cos \theta h^3}{3EI}, \delta_c = \frac{F \sin \theta h}{AE} \quad (6.2)$$

where A and I are the cross-sectional area and moment of inertia of the fibril, respectively, then the net displacement normal to the substrate is

$$\delta_n = \delta_c \sin \theta + \delta_b \cos \theta = \frac{F \cos^2 \theta h^3}{3EI} + \frac{F \sin^2 \theta h}{AE} \quad (6.3)$$

Finally we get the remote applied stress normal to the substrate σ , the strain in the fibrillar region ε_n , yielding the stress-strain relationship for the mat (5.4a), and the critical compressive strain for buckling ε_{cr} (6.4 b), by applying the buckling condition (6.1):

$$\varepsilon_n = \frac{\delta_n}{h \sin \theta}, \frac{\sigma}{E} = \frac{fF \sin \theta}{EA} = \frac{f}{1 + \frac{Ah^2}{3I} \cot^2 \theta} \varepsilon_n \quad (6.4a)$$

$$\varepsilon_{cr} = -\frac{b_c \pi^2}{3 \left(\frac{Ah^2}{3I} \right)} \left(1 + \frac{Ah^2}{3I} \cot^2 \theta \right) \quad (6.4b)$$

set that $f = \frac{NA}{\sin \theta}$ is the area fraction of the top of the fibrillar surface that makes contact, where N is the number of fibrils per unit area of the substrate.

For fibrils having a square cross section with side of length $2a$ and b , $I = \frac{ba^3}{3}$ and $A = 2ba$, the above equations may be rewritten:

$$\frac{\sigma}{E} = \frac{f}{1 + \frac{h^2}{a^2} \cot^2 \theta} \varepsilon_n \quad (6.5a)$$

$$\varepsilon_{cr} = -\frac{b_c \pi^2 a^2}{3h^2} \left(1 + \frac{h^2}{a^2} \cot^2 \theta \right) \quad (6.5b)$$

In case $b \gg a$, then deformation along the b direction can be assumed to be constrained by the substrate. As a consequence, plane strain deformation is inferred by replacing $E \rightarrow E^*$ and setting $b = 1$.

We will analyze in the following the case of the buckling stress for many fibrils indented by a rigid sphere. From now on, the contact mechanics convention that positive forces are compressive will be used. The relationship that links the effective work of adhesion W_{ad} to the maximum tensile load $-F_{max}$ is:

$$W_{ad} = \frac{-2F_{max}}{3\pi R} \quad (6.6)$$

From Equation (6.1), the theoretical buckling load for an individual plate-like fibril is found [6.2] to be:

$$P_c = 1.36 \frac{\pi^2 E^* a^3}{8h^2} \quad (6.7)$$

The load-displacement-data from spherical indentation of a flat PDMS sample (indentation data from fibrillar samples are similar), at sufficiently large displacements δ (i.e. when the force is non-tensile so that adhesion plays a negligible role in the deformation), may be fitted by the Hertz contact theory [6.5]:

$$F = \frac{4E^* \sqrt{R} \delta^{3/2}}{3} \quad (6.8)$$

where R is the sphere radius. In this way is possible to determine experimentally E^* , and then the buckling load by Equation (6.7).

Lateral Collapse of Adjacent Plate-Like Fibrils

Slender fibrillar structures, with large aspect ratio, give enhanced energy dissipation (i.e. enhanced adhesion) and increased interfacial compliance (see above and [1.55], for instance). However, if fibrils have sub-micrometer cross-sectional dimensions then the adhesiveness of the fibrillar architecture decorated with them is reduced after first contact with an external surface, given their tendency to collapse laterally under the influence of surface forces [6.2].

In order to study the lateral collapse phenomenon of surfaces decorated by fibrils, we will begin by considering plate-like fibrils (Figure 6.1-3). We will assume that:

$$\frac{H}{D}, \frac{h}{H}, \frac{a}{H}, \frac{w}{H} \gg 1 \quad (6.9)$$

set that D, H are the lateral dimension and the thickness of the substrate, $2a, 2b$ are the width and the length of each plate-like fibril, $2w$ is the distance between two adjacent fibrils along the x axis (Figure 6.1-3).

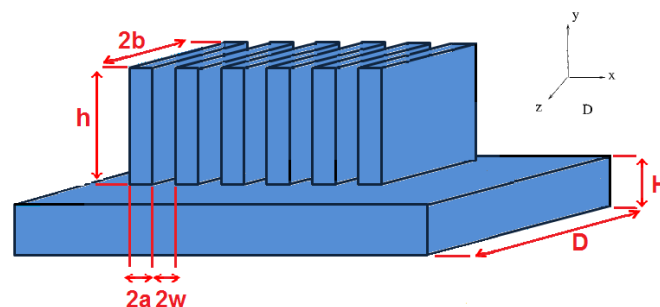


Figure 6.1-3 Schematic model of plate-like fibrillar structure. The sizes of the lateral dimension D and the thickness H of the substrate are depicted under-scaled respect to those of the plate-like fibrils.

Let us observe that the number of fibrils per unit length in the x axis is $N = 1/(2a + 2w)$. The model has been theoretically studied [6.2], and it has been also probed experimentally [6.6], by means of test structures fabricated with elastomer material. Various technique may be employed to realize them. For instance, the elastomer may be molded using negative image masters patterned by photolithography. Often, a stiff (e.g., glass) layer is glued to the elastomer structure backside to provide stability (not depicted in Figure 6.1-3). Let it be H_g the thickness of the stiff layer; it will be assumed that $H_g \ll D$. We will denote the Young's modulus and the Poisson ratio of the glass layer E_g, ν_g , respectively. The elastomer is assumed to be homogeneous and isotropic with Young's modulus E and Poisson's ratio ν .

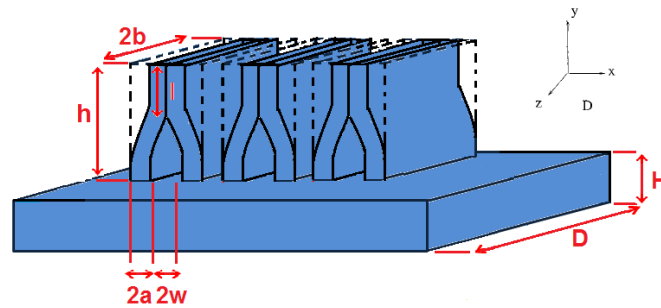


Figure 6.1-4 Schematic model of lateral collapsing in plate-like fibrillar structure. l represent the length of the contact region between two next neighboring plate-like fibrils.

The geometry of this structure allows us to consider 2D deformations, independent of the out-of-plane, that is z , direction. Since the load does not vary along the z axis, then from now on, unless otherwise specified, it will be meant per unit length. Furthermore, the model theory illustrated here below relies on the plane strain theory of elasticity [6.7] since the strain along z is zero.

Let us establish a criterion for lateral stability, consider the situation of Figure 6.1-4, where next-neighboring plate-like fibrils adhere to each other. Let l be the length of the noncontact region. In the contact region, the plates are virtually undeformed, while all the elastic strain energy is stored in the noncontact region, where bending deformation occurs. The total strain energy U of the system can be computed using elementary plate theory, assuming that the plate-like fibrils are plates clamped at one end:

$$U = \frac{16E^*a^3w^2}{l^3} \quad (6.9)$$

that shows, as expected, that for fixed w the elastic strain energy decreases with increasing l . If the straight edge between the contact and the noncontact region is shifted by an amount dl , that is $l \rightarrow l + dl$, then the resulting decrease in strain energy is:

$$dU = -\frac{48E^* a^3 w^2}{l^4} dl \quad (6.10)$$

Under equilibrium conditions, this energy variation dU will be equal to the amount of work dW needed to decrease the contact area by dl . Let us denote the surface energy by γ_s , then $dW = 2\gamma_s dl$, therefore:

$$l_{crit} = 2 \left(\frac{3E^* a^3 w^2}{2\gamma_s} \right)^{1/4} \quad (6.11)$$

From previous discussion is evident how plate-like fibrils such that their height h is smaller than the value l_{crit} , termed the **critical length**, will not undergo the lateral collapse, in such a way we get a **condition for lateral stability**:

$$\frac{2}{h} \left(\frac{3E^* a^3 w^2}{2\gamma_s} \right)^{1/4} < 1 \leftrightarrow \frac{h}{2a} \left(\frac{2\gamma_s}{3E^* a} \right)^{1/4} < \sqrt{\frac{w}{a}} \quad (6.12)$$

As already stated, validity of Equation (6.11) has been experimentally checked in contact experiments performed over poly(dimethylsiloxane) (PDMS) plate-like fibrillar structures (Figure 6.1-5b) by means of an experimental apparatus whose diagram is illustrated in Figure 6.1-5a.

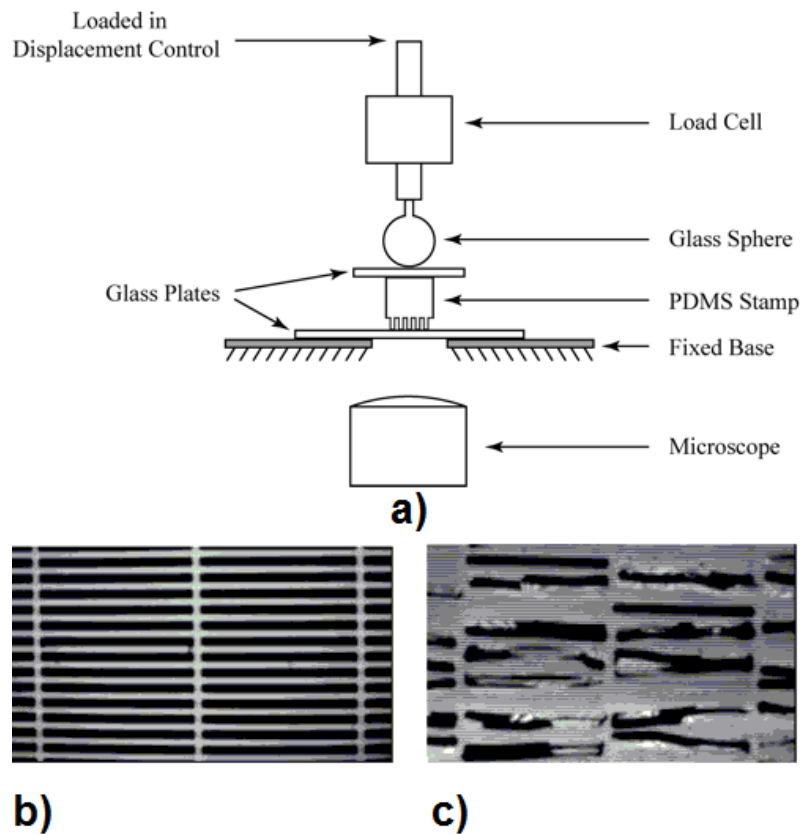


Figure 6.1-5 a) Schematic drawing of the instrument used to perform contact experiment over PDMS plate-like fibrillar structures. Optical micrographs showing b) no lateral collapse for fibrils with $a = w = 5\mu\text{m}$, $h = 30\mu\text{m}$ (such that the condition of lateral stability is fulfilled), and c) lateral collapse for fibrils with $a = w = 2.5\mu\text{m}$, $h = 30\mu\text{m}$ (such that the condition of lateral stability is violated). After K. G. Sharp, G. S. Blackman, N. J. Glassmaker, A. Jagota, C. Y. Hui, *Langmuir* **2004**, *20*, 6430-6438.

The PDMS sample was placed pattern-side down on a glass slide, that is with the surface decorated by fibrils in contact with the glass, and viewed with an inverted microscope. Under coaxial illumination the regions of the sample making contact with the glass were viewed as dark regions. Then a second piece of glass, slightly larger than the sample, was set on top of it, and a glass sphere was used to apply the load. Displacement was monitored via a linear variable differential transformer sensor, and a load cell connected in series with the glass sphere measured the total applied force. Load-displacement curves were acquired at various strain rates with visual information captured by a video recorder and, at fixed intervals, a three megapixel digital camera.

In Figures 6.1-5 b), c) is showed the results of contact experiments of similar PDMS plate-like fibrillar structures, with geometrical parameters such that the condition for lateral stability (6.12) is violated, so that the result of lateral collapsing showed in Figure 6.1-5 c) is expected under the model developed.

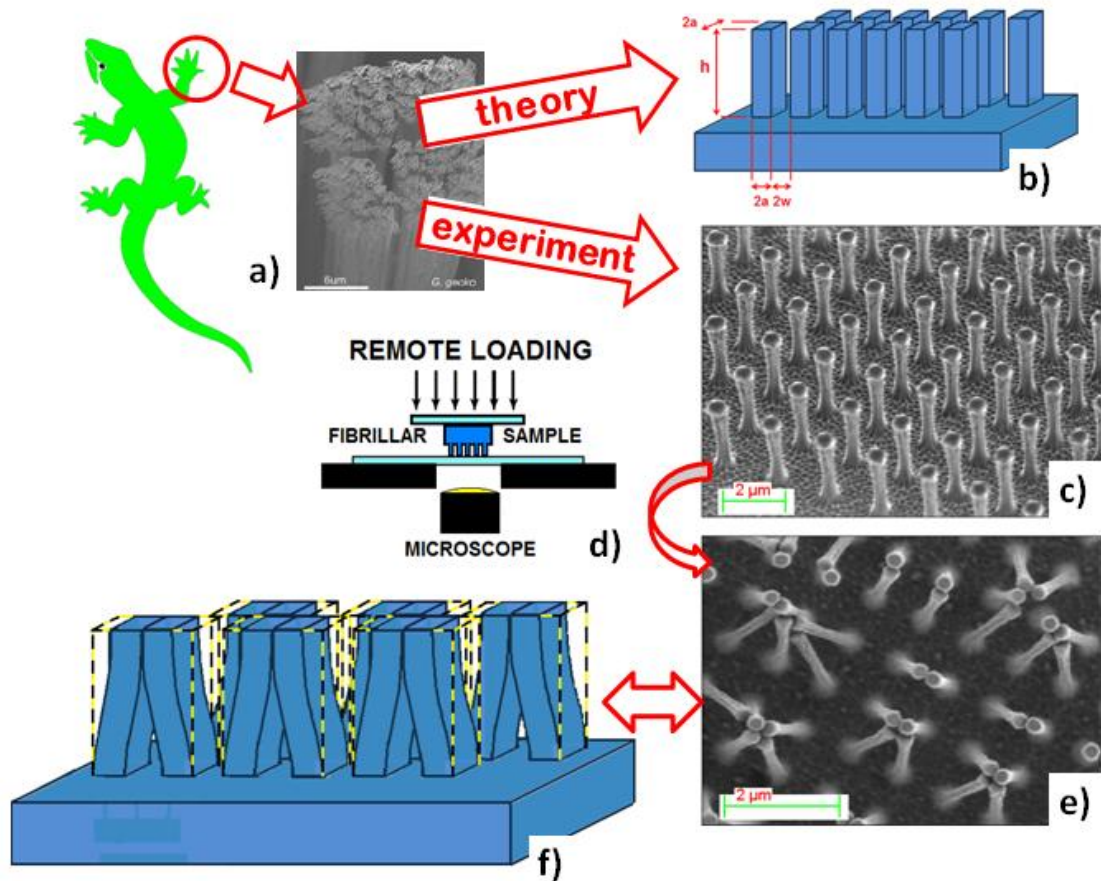


Figure 6.1-6 Survey of lateral collapse of fibrils.

- a) Contacting surface architecture in *G. gecko*. After A. Jagota, C.-Y. Hui, N. J. Glassmaker, T. Tang, *MRS Bull.* **32** (2007) 492–495.
- b) Model schematic of plate-like fibrillar structure. After C. Y. Hui, N. J. Glassmaker, T. Tang, A. Jagota, *J. R. Soc. Interface*, 2004, **1**, 23-33.
- c) SEM micrograph of polyimide fibrils microfabricated by electron-beam lithography and dry etching in oxygen plasma. After A. K. Geim, S. V. Dubonos, I. V. Grigorieva, K. S. Novoselov, A. A. Zhukov, and S. Y. Shapoval, *Nature Materials*, 2003, **2**, 7, 461–463.
- d) Schematics of the set-up for contact experiments. After C. Y. Hui, N. J. Glassmaker, T. Tang, A. Jagota, *J. R. Soc. Interface*, 2004, **1**, 23-33.
- e) SEM micrograph of bundled c) after having performed a contact experiment. After A. K. Geim, S. V. Dubonos, I. V. Grigorieva, K. S. Novoselov, A. A. Zhukov, and S. Y. Shapoval, *Nature Materials*, 2003, **2**, 7, 461–463.

6.2 Lateral Collapse of Nanowires

Equations (6.11) and (6.12) hold for adjacent fibrils of rectangular cross section, with sides of length $2a$ and $2b$, contacting along the side of length $2b$ (Figure 6.1-2 a). The length of the contacting side $2b$ doesn't affect the lateral collapsing occurrence, only E^* should be substituted by E if b is not much larger than a [1.55], leading finally to

$$\frac{h}{2a} \left(\frac{4\gamma_s}{3E^*a} \right)^{1/4} < \sqrt{\frac{w}{a}} \quad (6.13)$$

expressing the condition such that two neighboring pillars recover their initial straight alignment after contact. Conversely, the lateral collapse of two adjacent pillars occurs when the pillar height h satisfies the following inequality:

$$h > l_{crit} \equiv \left(\frac{12Ea^3w^2}{2\gamma_s} \right)^{1/4} \quad (6.14)$$

From the mechanical point of view, semiconductor NWs arrays are actually arrays of nanopillars. Since the self-adhesion of neighboring pillars wholly depends on the material properties and the array geometry, the above cited theory [1.55, 6.2] may well be applied also to explain the bundling phenomenon observed in NW arrays if the criterion for lateral collapsing (Equation (6.14)) is fulfilled. To this end is necessary to evaluate the critical length l_{crit} for the GaAs NW array, and compare it to the average GaAs NW height h .

6.2.1 Estimation of Parameter $2w$ for Randomly Located NWs

In the ideal fibrillar architecture used as a model in the previous subsection, all the pillars are located in a regular pattern, and they lie at equal distance $2w$ among each other (Figure 6.1-2 a). For GaAs NWs arrays of sample A1, A2 this is not anymore true (Figure 5.2-1 a), and then in order to apply Equation (6.14) the issue arises of how to deal with the parameter $2w$.

Extraction of 2-Dimensional Coordinate Systems Maps of the Spatial Location of NWs in the Arrays from SEM Images

The first step is to study the spatial locations of the NWs in the arrays. This can be performed by means of computer assisted analysis of the SEM plane view images of VA NWs at the earliest stage of SEM observation, that is when the electron beam scanning has mostly left unbent the NWS (Figure 5.2-1 a). The image analysis has been carried out by means of the ImageJ software, following this operative procedure:

1. conversion of original RGB color SEM images to 8-bit grayscale kind;

2. segmentation to binary and inversion (Figure 6.2-1 b), c);
3. determination of spatial location of each NW as (x, y) coordinate relative to the local maximum of luminance (Figure 6.2-1d).

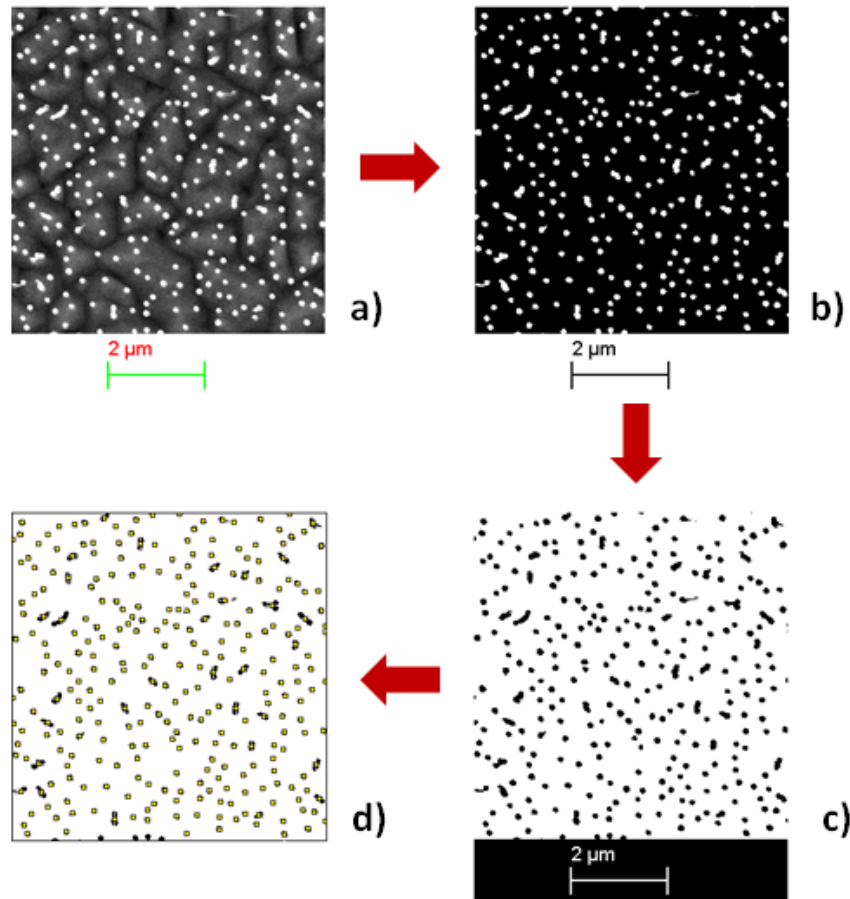


Figure 6.2-1 a) Plane view RGB color SEM image of VA GaAs NWs; b) correspondent 8-bit grayscale, segmented to binary converted image; c) image inversion; d) extracted 2-dimensional coordinate system map of local maxima of luminance.

Statistical Analysis of Spatial Point Patterns

The extracted 2-dimensional map of the NWs locations constitute a spatial point pattern that can be statistically analyzed. Spatial point processes are mathematical models describing the irregular or random spatial distribution of objects in the plane or in space [6.8]. To the simplest level the data simply consist of point coordinates describing the objects locations, even if additional characteristics of the objects can also be included in the analysis. The spatial patterns of a great variety of objects may be studied, such as atoms, molecules, biological cells, animals, plants, trees, particles, pores, or stars and galaxies. The classical fields of application then range from archaeology to astronomy, particle physics and forestry, but presently other fields such as ecology, biology, medicine and materials science extensively apply point process methods.

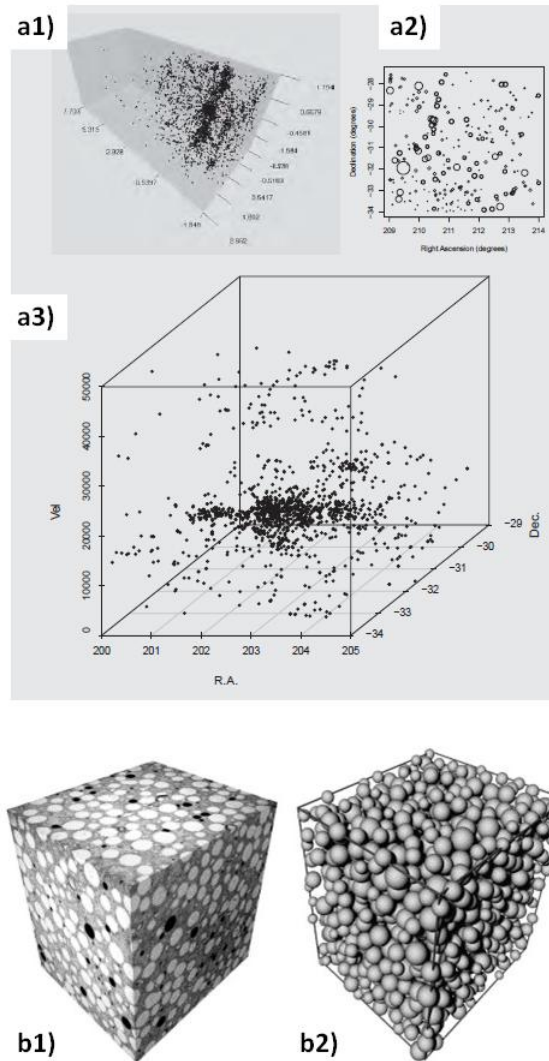


Figure 6.2-2 a1) – a3) Three-dimensional views of the Shapley Supercluster galaxy redshift survey: a1) full survey produced with *R*'s *rgl* package; a2) low-density region produced with *R*'s *plot* function with symbol sizes scaled to galaxy distance; a3) high-density region produced with *CRAN*'s *scatterplot3d* package. After E. D. Feigelson, G. J. Babu, *Modern Statistical Methods for Astronomy With R Applications*, Cambridge University Press, New York, USA, 2012. b1) A sample of concrete (self-flowing refractory castables) of size 10×10×10mm, obtained by computerized tomography. The white circles are cut corundum grains, the black ones air pores. b2) Result of 3D image analysis: the grains are approximated by spheres of variable radii. After Ballani, F., Daley, D.J., and Stoyan, D. (2005) Modelling the microstructure of concrete with spherical grains. *Comput. Materials Sci.* 35, 399–407.

The main classical techniques for investigating the spatial point maps are **distance methods**, based on measuring the distances between points. Specifically:

- **pairwise distances** $s_{ij} = \|x_i - x_j\|$ between all distinct pairs of points x_i and x_j ($i \neq j$) in the pattern,
- **nearest neighbor distances** $t_i = \min_{i \neq j} s_{ij}$ the distance from each point x_i to its nearest neighbor,
- **empty space distances** $d(u) = \min_i \|u - x_i\|$, the distance from a fixed reference location u in the window to the nearest data point.

The natural generalization of the distance between pillars $2w$ in case of not regularly spatial located NWs is the **distribution of nearest neighbor distances** (Figure 6.2-3). The statistical analysis of the spatial point maps extracted from the plane view SEM images of VA NWs (Figure 5.2-1) in order to determine this distribution has been performed by means of the *R*'s *spatstat* package. *Spatstat* [6.11] is a contributed package to the statistical language *R* [6.12] for the analysis of spatial point pattern data. It contains facilities for data manipulation, tools for exploratory data analysis, convenient graphical facilities, tools to simulate a wide range of point pattern models, versatile model-fitting capabilities, and model diagnostics. Both *spatstat* and *R* are freely available from the *R* website [6.13].

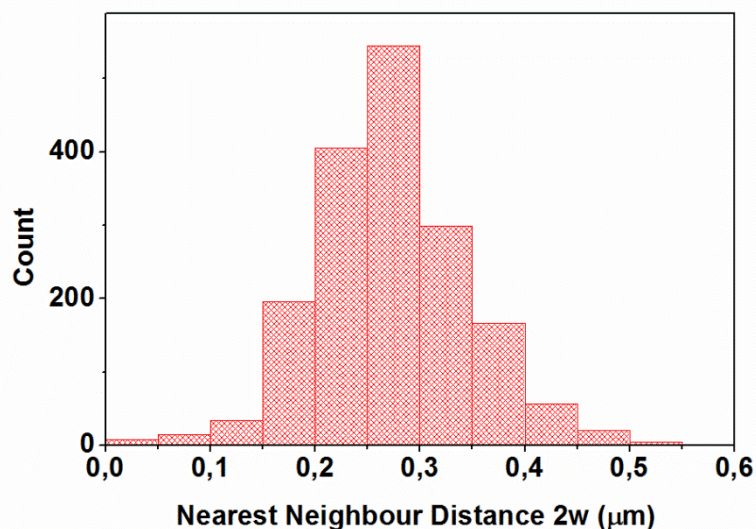


Figure 6.2-3 Plot of the distribution of the Nearest Neighbor Distance $2w$ between the GaAs NW in the arrays of sample A1, A2.

6.2.2 Theoretical Calculation of Surface Energy of III-V NWs

Except for nitride semiconductor compounds, all the III–V semiconductors in the solid phase have a stable cubic crystal lattice of the ZB type, the growth of the hexagonal WZ phase under normal conditions being hardly practicable. In fact, WZ

bulk GaAs is only occasionally reported [6.14] and most of its physical parameters are unknown. Then, another issue arises in order to apply Equation (6.14), that is what values to use for the surface energy γ_s and the Young modulus E of WZ GaAs NWs of samples A1, A2.

The construction of theoretical models of the surface energy for different facets of III–V semiconductors is an important topic in the context of growth of III–V NWs, because the surface energy of the lateral facets of the NWs in the cubic and hexagonal phases is a necessary parameter for the determination of the critical radius of the transition between the polytypes in the III–V NWs and for the corresponding optimization of the epitaxial growth conditions for controlling the crystal structure. On the other hand, as already explained, experimental data on these energies relevant to the hexagonal phase are actually not available.

The specific surface energy for a given face of a crystal is equal to the ratio of the energy expended for the separation into two parts of the crystal by the plane cross section parallel to the crystal face, to the surface area thus formed [6.15]:

$$\gamma_{hkl} = \frac{\varphi_{hkl}}{S_{hkl}} \quad (6.15)$$

for φ_{hkl} being the energy of separation for the cross section lying in the plane with the (hkl) crystallographic indices, and S_{hkl} the area of the surface formed.

In order to evaluate φ_{hkl} we may avail of the **nearest neighbor approximation** [6.16]: the energy spent for the detachment of atoms is equal to the energy of the dangling bonds on the newly formed surface, without taking into account the reconstruction of the surface. Only the bonds with the nearest and next nearest neighbors in the first and second coordination shells are essential (Figure 6.2-4). Then, the expression for the energy of breaking the bonds passing through the given plane of the surface can be written as:

$$\varphi_{hkl} = n_1\varphi_1 + n_2\varphi_2 \quad (6.16)$$

for n_i the numbers of the nearest and next nearest neighbors, and φ_i the corresponding energies of interaction between the nearest and next nearest neighbors.

From Equations (6.15) and (6.16) the surface energy of the face may be calculated [6.17], if the number of dangling bonds between the nearest and next nearest neighbors per unit area of the face is known.

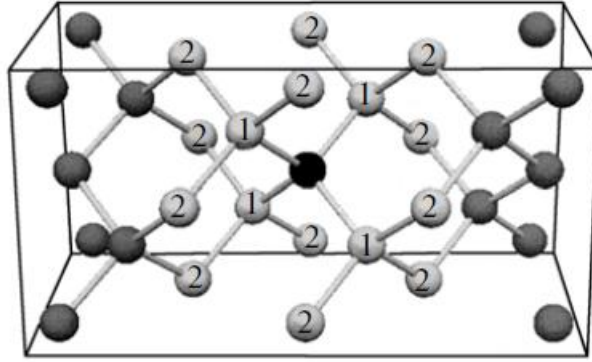


Figure 6.2-4 Face_centered cubic lattice: the nearest and next nearest neighbors of the central atom (shown as the black ball) are denoted by numbers 1 and 2, respectively; the other atoms are shown in gray. After N.V. Sibirev, M.A. Timofeeva, A.D. Bol'shakov, M.V. Nazarenko, V.G. Dubrovskii, *Physics of the Solid State*, **2010**, 52, 7.

All the atoms of a given face are obtained by the translation of the unit cell. The surface atoms can occupy different positions in the unit cell. For the atoms with identical positions relative to the unit cell, the number of dangling bonds is identical. Therefore it is possible to use the cleaving of the crystal lattice in two parts, one of which represents the atoms remaining in the crystal and the other part represents the atoms cut out as a result of the formation of the (hkl) or $(hklz)$ face. In this way the calculation of the number of dangling bonds for an atom belonging to a surface of a given orientation is carried out.

Crystal Lattice	Crystal Face	Number of dangling bonds		Surface Energy γ_s (J/m ²)	
		Nearest neighbors	Next-nearest neighbors	Experimental [6.18], [6.19]	Calculated Value
CUB	(100)	0.75	1	2.2	2.11
	(110)	0.53	3.18	1.5	1.543
	(111)	0.43	2.6	1.3	1.27
	(211)	0.61	3.06		1.79
HEX	(11 $\bar{2}$ 0)	0.53	3.18		1.543
	(1 $\bar{1}$ 00)	0.46	2.76		1.3

Table 6.I Surface energies for GaAs NWs. After N.V. Sibirev, M.A. Timofeeva, A.D. Bol'shakov, M.V. Nazarenko, V.G. Dubrovskii, *Physics of the Solid State*, **2010**, 52, 7.

Table 5.I reports the surface energies of GaAs NWs, both experimental and theoretical, for different crystal facets. It shows how the (11 $\bar{2}$ 0) surface for hexagonal phase is similar to the (110) surface for cubic phase. This fact allows for availing of the experimental values of γ_s of cubic GaAs (110) surface (listed in Table 5.II) for hexagonal GaAs (11 $\bar{2}$ 0) surface. Let us remember that the TEM

characterization of WZ GaAs NWs of sample A1, A2 has revealed that their sidewalls are six $\{11\bar{2}0\}$ faces.

Reference	γ_s (J/m ²)
[6.20]	0.69
[6.21]	0.86
[6.22]	1.23
[6.23]	2.24

Table 6.II – Experimental values of γ_s of the cubic GaAs (110) surface.

6.2.3 Adhesion-Driven GaAs NW Bundles

The last parameter to be determined in order to apply Equation (6.14) is the Young modulus E of WZ GaAs NWs. Since theoretical calculations has showed that the difference in the bulk modulus should not be larger than 1% [43], then E has been set equal to 85.5GPa, that is the value for bulk ZB GaAs as reported in literature [41].

In Figure 6.2-5 a) – e) the critical length l_{crit} has been plotted against the full intervals of possible values that $2w$, $2a$ may assume, as determined by their distributions, for each of the possible values of the surface energy γ_s as reported in Table 5.I and in Table 5.II. The maximum value reached by l_{crit} is of 2.5 μm , well below the average measured GaAs NW height of 5.5 μm . This means that the GaAs NWs of samples A1, A2 met the condition for the occurring of lateral collapse expressed by Equation (6.14). Once they are brought to contact, the adhesion forces overcome the elastic forces which would restore their original vertical alignment, and then they bundle together.

The conclusion is that the NW bundles formation, whose occurrence has been observed after the electron beam induced bending of NWs, Figure 5.2-1 for instance, has been successfully interpreted in the framework of the lateral collapse model for fibrillar structure.

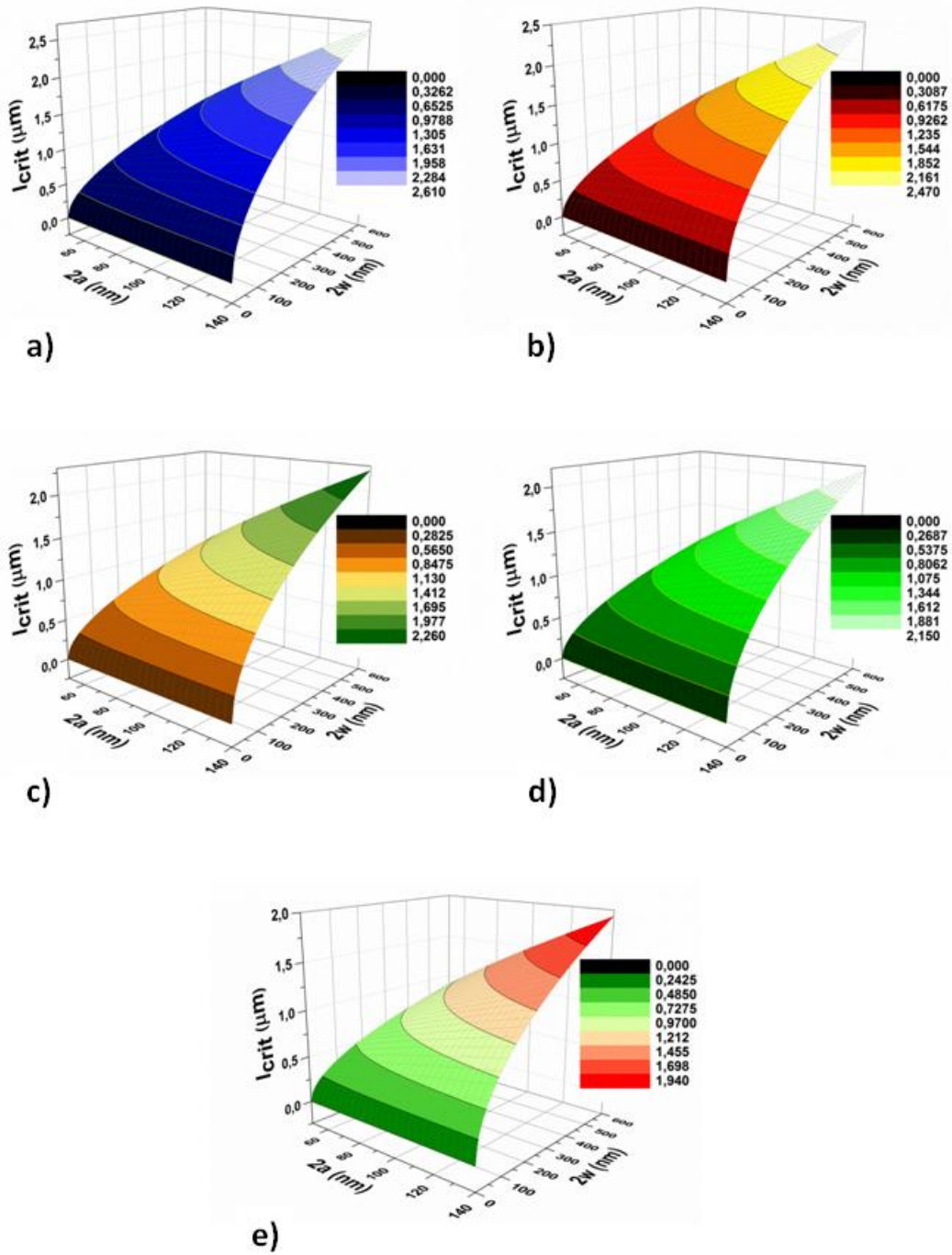


Figure 6.2-5 Plots of the critical length l_{crit} versus the cross-sectional dimension $2a$ (range from 50 nm to 140 nm) and the distance $2w$ between the NWs (range from 0 to 600 nm), for a) $\gamma_s = 0.69 \text{ J/m}^2$, b) $\gamma_s = 0.86 \text{ J/m}^2$, c) $\gamma_s = 1.23 \text{ J/m}^2$, d) $\gamma_s = 1.5 \text{ J/m}^2$, e) $\gamma_s = 2.24 \text{ J/m}^2$.

Finally, in order to check the stability of the NW bundles, two months after the SEM characterization, the AFM was employed to take topographic images of the samples cross sections. Probing the NW arrays by AFM had the goal to use a method alternative to SEM, in order to exclude any further perturbation from the electron beam over the array configuration. Figure 5.2-6 a) shows the AFM set-up used, while Figures 5.2-6 b) – d) are typical AFM topographic images that show the persistence of the bundles.

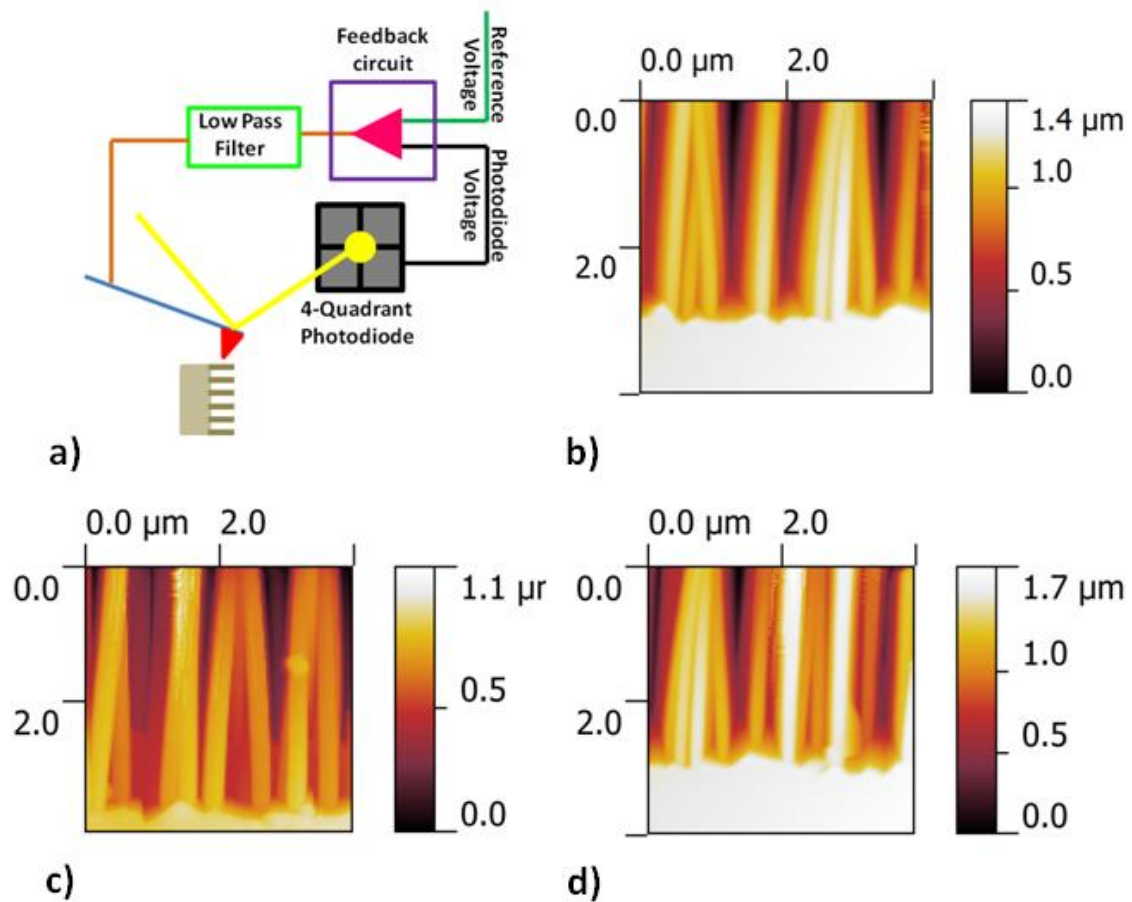


Figure 6.2-6 a) Schematic of the experimental set-up used for the AFM characterization. b) –d) AFM micrographs of a NW array in cross section (semi-contact mode) obtained two months after the SEM characterization.

BIBLIOGRAPHY

- [6.1] M. Scherge, S.N. Gorb, *Biological Micro- and Nanotribology: Nature's Solutions*, Springer, Berlin, 2001.
- [6.2] C. Y. Hui, A. Jagota, Y. Y. Lin, E. J. Kramer, *Langmuir*, 2002, **18**, 1394–1407.
- [6.3] S. P. Timoshenko, J. M. Gere, *Theory of elastic stability*, New York, McGraw-Hill, 1961.
- [6.4] S. H. Crandall, N. C. Dahl, T. J. Lardner, *An introduction to the mechanics of solids*, Kogakusha, McGraw-Hill, 1978.
- [6.5] K. L. Johnson, *Contact mechanics*, Cambridge, Cambridge University Press, 1985.
- [6.6] K. G. Sharp, G. S. Blackman, N. J. Glassmaker, A. Jagota, C. Y. Hui, *Langmuir* 2004, **20**, 6430-6438
- [6.7] N. I. Muskhelishvili, *Some Basic Problems of the theory of Elasticity*; Nordhoff: Groningen, The Netherlands, 1951; translated from Russian by J. R. M. Radok.
- [6.8] A. Penttinen, H. Stoyan, D. Stoyan, *Statistical analysis and modelling of spatial point patterns*, 2008, John Wiley & Sons Ltd, Chichester, England.
- [6.9] E. D. Feigelson, G. J. Babu, *Modern Statistical Methods for Astronomy With R Applications*, 2012, Cambridge University Press, New York, USA.
- [6.10] F. Ballani, D. J. Daley, D. Stoyan, *Computational Materials Science*, 2005, **35**, 399–407.
- [6.11] A. J. Baddeley and R. Turner. *Journal of Statistical Software*, 2005, **12**, 6, 1–42. URL: <http://www.jstatsoft.org>.
- [6.12] P. Dalgaard, *Introductory Statistics with R*, Springer, 2002.
- [6.13] The Comprehensive R Archive Network. URL <http://www.cran.r-project.org>.
- [6.14] M. I. McMahon, R. J. Nelmes, *Physical Review Letters*, 2005, **95**, 215505.
- [6.15] V. N. Portnov, E. V. Chuprunov, *Nucleation and Growth of Crystals*, Fizmatlit, Moscow, 2006.
- [6.16] V. G. Dubrovskii, N. V. Sibirev, *Physical Review B: Condensed Matter*, 2008, **77**, 035414.
- [6.17] N.V. Sibirev, M.A. Timofeeva, A.D. Bol'shakov, M.V. Nazarenko, V.G. Dubrovskii, *Physics of the Solid State*, 2010, **52**, 7.
- [6.18] J. W. Cahn, R. E. Hanneman, *Surface Science*, 1964, **1**, 387.
- [6.19] A. A. Stekolnikov, F. Bechstedt, *Physical Review B: Condensed Matter*, 2005, **72**, 125326.

[6.20] K. Wasmer, C. Ballif, R. Gassilloud, C. Pouvreau, R. Rabe, J. Michler, J.-M. Breguet, J.-M. Solletti, A. Karimi, D. Schulz, *Advanced Engineering Materials*, 2005, 7, 309–317, 2005.

[6.21] C. Messmer, J.C. Bilello. *Journal of Applied Physics*, 1981, 52, 7, 4623–4629.

[6.22] J. J. Gilman, *Fracture*, edited by B. L. Averbach, D. K. Felback, G. T. Hahn, and D. A. Thomas, Wiley, New York, 1959, p. 193.

[6.23] J. E. Sinclair, B. R. Lawn, *Proceeding of the Royal Society A*, 1972, **329**, 83.

CHAPTER 7

Conclusions and Future Directions

7.1 Si Grass SBDs

The main purpose has been to set-up a general procedure for probing electrically active defects in semiconductor NWs. DLTS is a well established method in the field of defect characterization as regards bulk semiconductors. However, technical limitations inherent to it together with intrinsic electrical properties of semiconductor NWs have prevented up to now its application to the study of defects in single semiconductor NWs.

The realization of NW array-based SBDs (illustrated in Chapter 2) has been then pivotal under many points of view.

1. It has permitted to investigate technological solutions for the challenging task of deposit front contacts over NW tops.
2. It has allowed to analyze the current transport in the Si Grass-based SBDs (Chapter 3). The fabricated devices have been electrically characterized. Then, different current transport models have fitted the experimental data. The statistical comparison of these fits has made it possible to single out the SCL current transport as the most probable conduction mechanism in these physical systems.
3. The filling of the NW array by an insulating material avoids shunting paths from front electrodes on NW tops to the substrate. This is advantageous both for the electrical conduction of the NW array-based devices as well as for ruling out any possible substrate contribution to the subsequent DLTS characterization.

DLTS measurements have been performed over Si Grass-based SBDs (Chapter 4). Devices based on unprocessed and RIE etched Si substrates have been characterized, too, to identify the deep levels associated to the RIE process. While the unprocessed Si substrate has showed to possess no defect-related peak in its DLTS spectra, those

of the RIE processed substrate have demonstrated that the RIE etching has introduced defects into the bulk Si. Interestingly, the defects in the RIE etched Si substrate and in the Si Grass appear to be different. This has been related to differences in damage mechanisms between horizontal surface and sidewalls inherent to the RIE etching process.

7.2 Electron Beam Mediated Bending and Bundling of GaAs NWs

In the second part of this thesis we have studied the bowing induced by electron beam and the subsequent clustering of GaAs NWs. The topic has led us to cross many fields, and is a good example of the fundamental interdisciplinary nature of the nanoworld. After motivated rejection of the few previously proposed mechanisms known in literature, we have advanced an original interpretation of the electron beam induced bending.

When the electron beam impinges a NW, it generates electron-hole pairs that may be separated at the NW surface-SCR. If the carrier generation is followed by the net charge redistribution, a potential drop across the surface-SCR occurs. This leads to a local change in the surface potential. The surface potential may be affected also by the non-uniform generation or recombination within the NW internal region, the presence of interfaces within the NW, the electron beam induced changes in NW surface or internal region. If some of the factors listed above varies among next-neighbor electron beam scanned NW, a difference in the surface potential is induced, which results in the rising of electrostatic forces between NWs that consequently bend. Besides, the bowing of WZ NWs induces a spontaneous polarization, and all these factors would finally cause the mechanical collapse of two or several NWs.

We have related this phenomenon to what happens in the field of micro-/nanoelectromechanical systems (MEMSs/NEMSs). A typical microswitch is constructed from two conducting electrodes, one electrode usually clamped to one end and the other end able to move. By applying a voltage difference between the two electrodes, the mobile electrode moves towards the fixed electrode under electrostatic attraction. At a threshold voltage the mobile electrode becomes unstable and collapses, or pulls in, on the fixed electrode. This phenomenon is widely investigated for electrostatic micro-actuators, at micro- and sub-micron scale separations, from the fundamental physics point of view as well as for the technological implications.

After the NWs are brought to contact, a second phenomenon occurs, that is their bundling together. We have successfully interpreted the formation of NW clusters in

the framework of lateral collapse of fibrillar structures. These latter are both idealized models and actual artificial structures that are used to study and to mimic the Gecko effect, that is the adhesion properties of natural surfaces in lizards and insects. Many the consequences we have drawn.

First, the engineering of NW orientation may be accomplished not only by growth conditions. The mechanical and surface properties of the NWs together with the geometrical design of the NW arrays play a key role for the post-growth control of their alignment. These parameters also matter in order to avoid the NWs bundling when departure from verticality is detrimental for the realization of NW array-based devices. But the same parameters open to the benign possibility of locally engineering NW arrays in micro- and macro-templates.

In recent years, there has been a large body of work towards explaining, controlling, exploiting the elastocapillary self-assembly of vertical nanofilaments. Aside to avoid its detrimental effects, its potentiality for solving the scalability issues of nanostructures has been recognized, like enhancing their packing density, forming periodic superstructures, to reorient thin films into horizontal sheets and multidirectional circuits, and to fabricate intricate 3D microarchitectures.

Semiconductor NW arrays are at the crossroads of many different pathways. The importance of being semiconductor is that a natural outcome for these systems is in the realization of nanodevices. Differently from the quantum dots or quantum wells, they possess a three-dimensional geometry. This gives them possibilities of integration and superstructuring which cannot be reached by other nanostructures. The geometry itself may affect the property of the system, as we have demonstrated and it represents an additional degree of freedom which is worthwhile to be much more explored in the future.

LIST OF TABLES

Table 2-I – List of post-spincoating temperature treatments details (softbaking and hardbaking) and mechanical stability filling media for four different organic polymer. [1.16]	32
Table 3-I Electrical parameters of the PtSi/p-SiNWs SBDs.	51
Table 3-II Main parasitic effects that may occur in diodes. <i>After</i> E. Fred Schubert, <i>Light Emitting Diodes, Second Edition</i> , Cambridge University Press, New York, 2006.	52
Table 3-III Adjusted r-Square Values for the fitted models.	56
Table 3-IV Difference in AIC values for the different pair of models.	57
Table 4-I Thermodynamic parameters of the Deep Levels detected in samples I, II, III.	81
Table 5-I Listing of morphological characteristics of the ZnO NWs samples, and correspondent bending and bundling features are reported. <i>After</i> J. Liu, S. Lee, K. Lee, Y. H. Ahn, J.-Y. Park, K. H. Koh, <i>Nanotechnology</i> , 2008, 19 , 185607.	93
Table 5-II Material properties and experimental results for all the tested arrays.	99
Table 6.I Surface energies for GaAs NWs. <i>After</i> N.V. Sibirev, M.A. Timofeeva, A.D. Bol'shakov, M.V. Nazarenko, V.G. Dubrovskii, <i>Physics of the Solid State</i> , 2010 , 52, 7.	123
Table 6.II – Experimental values of γ_s of the cubic GaAs (110) surface.	124

LIST OF FIGURES

Figure 1.2-1 Applications of Si Grass.

a) chinese hamster ovaric cells on Si Grass. After V. Cimalla, M. Stubenrauch, F. Weise, M. Fischer, K. Tonisch, M. Hoffmann, O. Ambacher, *Applied Physics Letters*, 2007, **90** 2007, 10, 3. b) Si Grass as Nano-Velcro. After M. Stubenrauch, M. Fischer, C. Kremin, S. Stoebenau, A. Albrecht, O. Nagel, *Journal of Micromechanics and Microengineering*, 2006, **16**, 6, S82-S87. 2

Figure 1.2-2 Semiconductor NW array-based Schottky diodes.

a1) – a8) Schematic illustration of the fabrication of Pt/p-Metal-Assisted wet Chemical Etched SiNWs devices. a1) – a3) NW wet etching process. a4) Photoresist spin coating over the Si NWs; the spin coating speed has been calibrated in order to get a polymer layer thickness less than the NWs height. a5) O₂ plasma dry etching of the remnants of photoresist from the exposed tips of Si NWs. SEM images of a5.I) cross section and a5.II) plane view of p-Si NWs after photoresist spin coating. a6) Pt contact deposition on the tips of p-SiNWs by electron beam evaporation. a7) Acetone removing of photoresist on wafer backside. a8) Current-Voltage measurement setup. After Z. Wang, M. Zhu, X. Chen, Q. Yan, J. Zhang, *Microelectronic Engineering*, 2013, **103**, 36–41.

b1) – b6) 3D radial heterojunction photodiode. b1, b2) Ag nanoparticle mask over p-Si substrate by annealing for different time durations. b3) – b4) Cross-sectional images after RIE etching of samples b1), b2) respectively, showing b3) an higher density, b4) a lower density of Si NWs. b5) – b6) AZO film was deposition on top of b3), b4) Si NWs, respectively. After S.-W. Jee, S.-J. Park, J. Kim, Y. C. Park, J.-H. Choi, J.-H. Jeong, J.-H. Lee, *Applied Physics Letters*, 2011, **99**, 053118.

c1) SEM image of as grown ZnO Nanorods, and in the inset after spin coating the insulating layer and subsequent soft backing. C2) Schematic illustration of Au/ZnO Nanorods Schottky diode. After I. Hussain, M. Y. Soomro, N. Bano, O. Nur, M. Willander, *Journal of Applied Physics*, 2013, **113**, 234509. 4

Figure 1.2-3 Defect level formation and characterization in Au-catalyzed VLS grown Si NWs.

a) Schematics of Growth of Au-catalyzed Si NWs by VLS mechanism. After A. Cavallini, S. Carapezzi, A. Castaldini, A. Irrera, *Physica B*, 10.106/j.physb.2013.11.021
b1), b2) Experimental proof of surface diffusion of Au from the NWs tip. EDX spectra and STEM images of a Si NW grown at 575 °C with 0.077 mbar silane partial pressure. The arrow show the location where the EDX spectrum has been taken. The brighter particles are unambiguously gold rich clusters, as three typical gold lines appear in

the EDX spectrum about 2200 eV. After M. I. Hertog, J.-L. Rouviere, F. Dhalluin, P. J. Desré; P. Gentile, P. Ferret, F. Oehler, T. Baron, *Nano Letters*, **2008**, *8*, 1544–1550.

c) Typical PICTS spectrum of P-doped VLS grown Si NWs, obtained with an emission rate $e_p = 512 \text{ s}^{-1}$ and a pulse width of 10 ms. The labels identify the four traps emitting at the peaked positions. The E2B level has the emission characteristics of the donor level E(0/+) peculiar of the phosphorus-vacancy (PV) pairs of the E-center. The E3 level has the thermodynamic characteristics of the donor (0/+) level of the Au–H complex. After K. Sato, A. Castaldini, N. Fukata, A. Cavallini, *Nano Letters*, **2012**, *12* (6) 3012. 6

Figure 1.3-1 Effect of pressure and temperature on the epitaxial growth direction.

a) Array of 60-nm-diameter SiNWs grown at $p\text{SiH}_4=80 \text{ mTorr}$. Most of NWs grow in the vertical $\langle 111 \rangle$ direction, epitaxial to the substrate. b) 60-nm-diameter wires grown at $p\text{SiH}_4=400 \text{ mTorr}$. At this pressure all wires have kinks, but all are still epitaxial. After H. Schmid, M. T. Bjork, J. Knoch, H. Riel, W. Riess, P. Rice, T. Topuria, *Journal of Applied Physics* 2008, **103**, 024304–7. 8

Figure 1.3-2 NW nanolasers.

a) Schematic of an optically pumped nanowire laser cavity. b) A multi-quantum-well (MQW) NW and magnified cross-sectional view of a NW facet showing the InGaN/GaN MQW structure. The InGaN layer is indicated in yellow. c) Lasing spectrum from an individual ZnO NW; in the inset a far-field optical image of a lasing GaN nanowire. d) Normalized lasing spectra collected from four representative MQW nanowire structures with different indium composition. After R. Yan, D. Gargas, P. Yang, *Nature Photonics*, 2009, **3**, 569 - 576. 9

Figure 1.3-3 Examples of capillary self-assembly of top-gathering pillars.

a) Photoresist pillars fabricated by multibeam lithography. After D. Wu, Q.-D. Chen, B.-B. Xu, J. Jiao, Y. Xu, H. Xia, H. B. Sun, *Applied Physics Letters*, 2009, **95**, 091902.

b) SU8-epoxy pillars after capillary self-assembly and subsequent pyrolysis. After M. F. L. De Volder, R. Vansweevelt, P. Wagner, D. Reynaerts, C. Van Hoof, A. J. Hart, *Acs Nano*, 2011, *5*, 6593 – 6600.

c,d) Arrays of polymer nanopillars fabricated by electron-beam lithography, then clustered by capillary self-assembly. After H. Duan, K. K. Berggren, *Nano Letters*, 2010, **10**, 3710 – 3716.

e,f) CNT forest micropillars that aggregate by capillary self-assembly. After M. F. L. De Volder, S. J. Park, S. H. Tawfick, D. O. Vidaud, A. J. Hart, *J. Micromechanical Microengineering*, 2011, **21**, 045033. 11

Figure 1.3-4 Arrays composed of grounded gold-coated epoxy nanopillars.

a) Position of a single nanopillar before (top) and after (bottom) electron beam exposure in spot mode; the white cross indicates the position of the electron beam. Scheme for the edge-on view is on the right. b) Image of a sample before (left) and after (right) 60 s exposure to the electron beam in spot mode, focused on the center of a single nanopillar. The white cross indicates the position of the electron beam. c) Inward bending and cluster formation upon focusing the electron beam in the center of four gold-coated nanopillar, disconnected from the ground. d) Outward bending of four carbon-coated nanopillar, disconnected from the ground. Scale bars are 1 μm for a), 2 μm for c) and d). e) Applications for patterning. Writing of letters in nanopost arrays through repeated exposure to the e-beam in spot mode.

After A. Seminara, B. Pokroy, S. H. Kang, M. P. Brenner, J. Aizenberg, *Physical Review B*, 2011, **83**, 235438. 12

Figure 2.1-1 CCP RIE schematic chamber design. 22

Figure 2.1-2 ICP RIE schematic chamber design. 23

Figure 2.1-3 Basic Processes in Plasma Etching. 1: etchant flow. 2: ionization. 3: diffusion. 4: adsorption. 5: reaction. 6: desorption. 7: diffusion. 8: pump out. After S. Franssila, *Introduction to Microfabrication, Second Edition*, John Wiley & Sons 2010. 24

Figure 2.1-4 a) Isotropic profile by thermally activated etching, and b) ion-induced etched anisotropic profile. 25

Figure 2.1-5 Methods for anisotropic etching: a) suppression of the spontaneous chemical component relative to the ion-induced component, b) surface passivation. 26

Figure 2.1-6 Bosch process steps. a) Deposition of a masking layer over Si substrate. b) STEP 0: Si etching, c) STEP 1: passivation, d) STEP 2.I: polymer etching, e) STEP 2.II: Si etching. f) – h) one cycle repetition. i) final removing of polymer. 27

Figure 2.1-7 a) RIE and b) BOSCH processed Si grass. 28

Figure 2.1-8 SEM cross section views of Si grass samples. 30

Figure 2.1-9 Si grass NW a) height distribution and b) base section distribution. 30

Figure 2.2-1 Scheme of spin coating of photoresist over Si Grass sample. 33

Figure 2.2-2 Si grass NW array sample after the filling step. a) Lower and b) higher magnification tilted view of the embedded NW array. c) Determination of the thickness of the filler layer. d) High magnification of details of the Si grass NWs tops above the filler surface; unwanted residuals of the filler material appears to cover them. e) SEM plane view of the embedded NW array; the filling of the sample

appears to be complete. No observations of regions that are depleted of the filler due to bubbles formation during the deposition step. 34

Figure 2.2-3 a), b) Results of RIE etching of SU8 for exposition of NW tips. 35

Figure 3.1-1 Band bending diagram before and after metal–semiconductor contact for a) metal and n-type semiconductor, $\phi_M > \phi_S$ b) metal and n-type semiconductor, $\phi_M < \phi_S$ c) metal and p-type semiconductor, $\phi_M > \phi_S$ and d) metal and p-type semiconductor, $\phi_M < \phi_S$. After L. J. Brillson, *Surfaces and Interfaces of Electronic Materials*, WILEY-VCH Verlag GmbH & Co. KGaA, Weinheim, 2010. 40

Figure 3.1-2 Band bending diagram a) before and after b) metal–semiconductor junction formation in case of a high density of surface states; c) band diagram after contact in the ideal case. After L. J. Brillson, *Surfaces and Interfaces of Electronic Materials*, WILEY-VCH Verlag GmbH & Co. KGaA, Weinheim, 2010. 41

Figure 3.2-1 Basic transport processes in forward biased Schottky junction. 1) Thermionic emission. 2) Tunneling. 3) Recombination. 4) Diffusion of Electrons. 5) Diffusion of Holes. After S. M. Sze, *Physics of semiconductor devices*, Wiley, 1981. 42

Figure 3.2-2 Image force lowering of a Schottky barrier. After E. H. Roderick, R. H. Williams, *Metal-Semiconductor Contacts, Second Edition*. Oxford, Clarendon Press, 1988. 43

Figure 3.2-3 Image force lowering of a Schottky barrier under forward ($\Delta\phi_F$) and reverse ($\Delta\phi_R$) bias. After S. M. Sze, *Physics of semiconductor devices*, Wiley, 1981. 45

Figure 3.3-1 Schematic of the fabrication process of Si Grass-based Schottky diodes. a) As grown NW array. b) Filling step for NW integration with inactive layer. c) Dry etching step for cleaning of NW tips from unwanted residuals of filling step. d) Deposition of Schottky contact and of backside Ohmic contact; typical current-voltage characteristics of the realized devices is shown. 49

Figure 3.3-2 RT forward $\ln(I)$ -V of Si Grass-based SBDs. The red line corresponds to the linear region. 50

Figure 3.3-3 Log-Log plot of RT forward I-V curve in case of one-carrier SCLC injection controlled by a single set of traps. After M. A. Lampert, P. Mark, *Current Injection in Solids*, Academic Press, New York, 1970. 53

Figure 3.3-4 RT forward I-V of Si Grass-based SBDs, high bias region ($V \geq 2$), fitted a) linearly, b) with power-law $I \propto V^m$, c) by Poole-Frenkel model. 55

Figure 3.3-5 Relationship between the difference in AIC scores and the probability that each model is true. After H. J. Motulsky, A. Christopoulos, *Fitting Models to*

Biological Data Using Linear and Nonlinear Regression. A Practical Guide to Curve Fitting. GraphPad Software Inc., San Diego CA, 2003. 57

Figure 4.1-1 Emission and capture processes at a deep level: (a) hole emission to the valence band, (b) electron capture from the conduction band, (c) hole capture from the valence band, (d) electron emission to the valence band. 61

Figure 4.1-2 Electron and hole capture and emission processes for an electron trap in a n-type semiconductor. After P. Blood, J. W. Orton, *The electrical characterization of semiconductors: majority carriers and electron states*, London: Academic Press, 1990. 62

Figure 4.1-3 Majority carrier traps. After P. Blood, J. W. Orton, *The electrical characterization of semiconductors: majority carriers and electron states*, London: Academic Press, 1990. 66

Figure 4.1-4 Minority carrier traps. After P. Blood, J. W. Orton, *The electrical characterization of semiconductors: majority carriers and electron states*, London: Academic Press, 1990. 67

Figure 4.1-5 Conduction band diagram at zero bias applied. After P. Blood, J. W. Orton, *The electrical characterization of semiconductors: majority carriers and electron states*, London: Academic Press, 1990. 67

Figure 4.1-6 Conduction band diagram at reverse bias applied. After P. Blood, J. W. Orton, *The electrical characterization of semiconductors: majority carriers and electron states*, London: Academic Press, 1990. 68

Figure 4.1-7 Principle of C₁-DLTS operation by reduced reverse bias pulse for majority carrier injection.

a) Charge state of defects, b) bias pulsing, c) time dependence of the capacitance during the measurement. After P. Blood, J. W. Orton, *The electrical characterization of semiconductors: majority carriers and electron states*, London: Academic Press, 1990 70

Figure 4.1-8 Schematics of the principle of the two-point subtraction rate window: a) the capacitance transient sampled at times t₁, t₂, b) the weighting function w(t). After P. Blood, J. W. Orton, *The electrical characterization of semiconductors: majority carriers and electron states*, London: Academic Press, 1990. 72

Figure 4.1-9 a) Capacitance transients at various temperatures, b) corresponding double box-car DLTS signal. 72

Figure 4.3-1 Schematic of the ideal equivalent circuit of a NW array-based SBD. 76

Figure 4.3-2 Optical images of the substrate surface of a) sample I, b) sample II.	76
Figure 4.3-3 DLTS spectrum at emission rate $e_p = 512.8 \text{ s}^{-1}$; the peak labeled BB has activation energy $E_a = 0.06 \text{ eV}$ and apparent capture cross section $\sigma_a = 1 \cdot 10^{-17} \text{ cm}^2$, correspondent to those of the shallow level due to B dopant in substitutional position in bulk Si.	78
Figure 4.3-4 DLTS spectrum at emission rate $e_p = 46.5 \text{ s}^{-1}$	79
Figure 4.3-5 Arrhenius Plot reporting the signatures of the deep levels W and Z.	79
Figure 4.3-6 DLTS spectrum at emission rate $e_p = 46.5 \text{ s}^{-1}$	80
Figure 4.3-7 Arrhenius Plot reporting the signatures of the deep levels A, B, C.	80
Figure 5.1-1 MBE model of NW growth [4-1]. NW is assumed as being a cylinder of diameter $D=2R$ and length L , the contact angle of drop to be of 90° . The processes on the substrate surface are adsorption, desorption, diffusion, and nucleation; the processes on the NW sidewalls are desorption and diffusion (NW axial growth) and adsorption (NW radial growth); the processes on the NW top are adsorption and desorption on the liquid surface and the vertical growth of the top facet.	86
Figure 5.1-2 a) Detail of 45° tilted-SEM image of sample A2, showing the characteristic pencil-like tip. b) Low magnification TEM image of a representative GaAs NW (sample A2), imaged along the $[11\bar{2}0]$ direction; in the inset a diffractogram of the same wire in the tip region showing the WZ structure.	87
Figure 5.2-1 SEM Plain views of sample A1. a) Original VA NWs. b) The white squares labeled 1 and 2 show typical GaAs NWs bending induced by the electron beam scanning. c) The white squares labeled 1 and 2 show the lateral collapse of couples of GaAs NWs. The white square labeled 3 evidences the occurrence of a triangular configuration. More complex geometries also appear (white squares labeled 4-10). Beam Energy 10 KeV.	89
Figure 5.3-1 a) low-magnification SEM image of aligned ZnO nanorods. b), c) 30° side view of self-attraction phenomenon. After X. Wang, C. J. Summers, Z. L. Wang, <i>Applied Physics Letters</i> , 2005, 86 , 013111.	90
Figure 5.3-2 a), b) Au-ZnO junction band diagram. After X. Wang, C. J. Summers, Z. L. Wang, <i>Applied Physics Letters</i> , 2005, 86 , 013111.	91
Figure 5.3-3 a), b) Schematic model of the interaction between two ZnO nanorods. After X. Wang, C. J. Summers, Z. L. Wang, <i>Applied Physics Letters</i> , 2005, 86 , 013111.	91
Figure 5.3-4 SEM plain view of a typical NW bundle in sample A1. The micrograph a) shows the SEM image as experimentally obtained, while b) evidences by the white	

arrows the unbent Au-capped tip of the NWs. White stripes highlight the contact regions between adjacent NWs, which is facet-to-facet (stripe 1) or, in a very unusual way, between the edges (stripes 2). Beam energy 10 KeV.92

Figure 5.3-5 a1), a2) are plane view of samples S1, S2. b1) – b4) are FE-SEM images of sample T3. ZnO nanorods about 160 nm thick were bundled together. The circle in b1) emphasizes the boundary between two nanorods in contact, indication that the merging occurred during growth; b2) is a cross-sectional image showing that the tops of some bundled nanorods exhibited darker color as marked by rectangles. High-magnification images of such areas show sheet-like structures, either filling the gap among bent nanorods b3) or bridging two thick nanorods about 200 nm apart b4). Plane view images at low (c1) and high (c2) magnifications of sample T2, where it appears that all NWs are bundled together. Tilted view low-magnification image (d1) and high- magnification images (d2) and d3) of various bundling configurations of sample T1. e) is a plane view of sample T3, and no bundling is observed. After J. Liu, S. Lee, K. Lee, Y. H. Ahn, J.-Y. Park, K. H. Koh, *Nanotechnology*, 2008, **19**, 185607.94

Figure 5.3-6 Sequential order of the micrographs a) → c) of details of SEM images of the zone probed in Figures d, e. They show an originally unbent NW (a), black arrow pointing to his tip) that during the electron-beam scanning snap to contact (see b), white ellipse). c) correspond to the final bundled configuration. Beam energy 3 KeV.95

Figure 5.3-7 Nanowire kissing. a) VA GaAs NWs and merged NW bundles coexisting in the same substrate region. Evolution of GaAs NW kissing observed from three individual growth runs with increasingly longer growth times t_g (NW lengths): b) two vertical NWs grow parallel to each other ($t_g = 1$ min); c) NWs bend and kiss ($t_g = 2$ min); and d) NWs merge in a bundle ($t_g = 3$ min). Tilted SEM images obtained at 45° angle. After D. Xing, S. A. Dayeh, V. Veeramuthu, A. Larrue, J. Wang, H. Su, C. Soci, *Nano Letters*, **2011**, 11, 4947–4952.96

Figure 5.3-8 Atomic model of a GaAs NW grown in the [111] orientation. a) Top and b) side views from a <110> orientation. c) Adjacent NWs with A and B facets attract each other electrostatically. After D. Xing, S. A. Dayeh, V. Veeramuthu, A. Larrue, J. Wang, H. Su, C. Soci, *Nano Letters*, **2011**, 11, 4947–4952.97

Figure 5.4-1 Sequential order of the micrographs a) → c) of details of SEM images of the zone probed in Figures d, e. They show an originally unbent NW (a), black arrow pointing to his tip) that during the electron-beam scanning snap to contact (see b), white ellipse). c) correspond to the final bundled configuration. After A. Seminara, B. Pokroy, S. H. Kang, M. P. Brenner, J. Aizenberg, *Physical Review B*, 2011, **83**, 235438. ...98

Figure 5.4-2 Schematic geometry of the electron beam impinging in the nearby of the nanopillar: after the electron beam (current I) impacts the specimen, electrons

are backscattered, with backscattering coefficient η and backscattering angles θ . After A. Seminara, B. Pokroy, S. H. Kang, M. P. Brenner, J. Aizenberg, *Physical Review B*, 2011, **83**, 235438. 100

Figure 5.4-3 Monte Carlo simulation of trajectories of electrons impacting the nanopost at $\theta = 30^\circ$ for different energies (10 KeV on the left, 10 KeV on the right). The trajectories of 10 KeV-electrons are straight lines, meaning that they pass through the nanopillar. 2 KeV-electrons at 2 KeV do not have enough energy to penetrate the nanopillar. After A. Seminara, B. Pokroy, S. H. Kang, M. P. Brenner, J. Aizenberg, *Physical Review B*, 2011, **83**, 235438. 101

Figure 5.4-4 Domain of integration of Poisson equation and magnification of the base of the nanopillar, showing the variable triangular mesh in the substrate and square mesh on the nanopillar. The shaded area is charged with $\rho(z) = \frac{\lambda(z)}{l^2}$. After A. Seminara, B. Pokroy, S. H. Kang, M. P. Brenner, J. Aizenberg, *Physical Review B*, 2011, **83**, 235438. 102

Figure 5.4-5 Simulation of carbon-coated nanopillar at maximum bending for different values of x_c between $-r$ (right) and r (left). After A. Seminara, B. Pokroy, S. H. Kang, M. P. Brenner, J. Aizenberg, *Physical Review B*, 2011, **83**, 235438. 103

Figure 6.1-1 – Hierarchy of structure in the gecko toe attachment system. After K. Autumn, Y. A. Liang, S. Tonia Hsieh, W. Zesch, W. P. Chan, T. W. Kenny, R. Fearing, R. J. Full, *Nature*, 2000, **405**, 681–684. 109

Figure 6.1-2 a) Schematic model of fibrillar structure. b) Fabricated fibrillar structure by molding PDMS into silicon master with ion-etched holes. 111

Figure 6.1-3 Schematic model of plate-like fibrillar structure. The sizes of the lateral dimension D and the thickness H of the substrate are depicted under-scaled respect to those of the plate-like fibrils. 113

Figure 6.1-4 – Schematic model of lateral collapsing in plate-like fibrillar structure. l represent the length of the contact region between two next neighboring plate-like fibrils. 114

Figure 6.1-5 – a) Schematic drawing of the instrument used to perform contact experiment over PDMS plate-like fibrillar structures. Optical micrographs showing b) no lateral collapse for fibrils with $a = w = 5\mu\text{m}$, $h = 30\mu\text{m}$ (such that the condition of lateral stability is fulfilled), and c) lateral collapse for fibrils with $a = w = 2.5\mu\text{m}$, $h = 30\mu\text{m}$ (such that the condition of lateral stability is violated). After K. G. Sharp, G. S. Blackman, N. J. Glassmaker, A. Jagota, C. Y. Hui, *Langmuir* **2004**, *20*, 6430-6438. 116

Figure 6.1-6 Survey of lateral collapse of fibrils.

- a) Contacting surface architecture in G. gecko. After A. Jagota, C.-Y. Hui, N. J. Glassmaker, T. Tang, *MRS Bull.* **32** (2007) 492–495.
- b) Model schematic of plate-like fibrillar structure. After N. J. Glassmaker, A. Jagota, C.-Y. Hui, J. Kim, , *Journal of the Royal Society Interface*, **2004**, 1, 23–33.
- c) SEM micrograph of polyimide fibrils microfabricated by electron-beam lithography and dry etching in oxygen plasma. After A. K. Geim, S. V. Dubonos, I. V. Grigorieva, K. S. Novoselov, A. A. Zhukov, and S. Y. Shapoval, *Nature Materials*, 2003, **2**, 7, 461–463.
- d) Schematics of the set-up for contact experiments. After N. J. Glassmaker, A. Jagota, C.-Y. Hui, J. Kim, , *Journal of the Royal Society Interface*, **2004**, 1, 23–33.
- e) SEM micrograph of bundled c) after having performed a contact experiment. After A. K. Geim, S. V. Dubonos, I. V. Grigorieva, K. S. Novoselov, A. A. Zhukov, and S. Y. Shapoval, *Nature Materials*, 2003, 2, 7, 461–463. 117

Figure 6.2-1 a) Plane view RGB color SEM image of VA GaAs NWs; b) correspondent 8-bit grayscale, segmented to binary converted image; c) image inversion; d) extracted 2-dimensional coordinate system map of local maxima of luminance. 119

Figure 6.2-2

- a1) – a3) Three-dimensional views of the Shapley Supercluster galaxy redshift survey: a1) full survey produced with *R*'s *rgl* package; a2) low-density region produced with *R*'s *plot* function with symbol sizes scaled to galaxy distance; a3) high-density region produced with *CRAN*'s *scatterplot3d* package. After E. D. Feigelson, G. J. Babu, *Modern Statistical Methods for Astronomy With R Applications*, Cambridge University Press, New York, USA, 2012. b1) A sample of concrete (self-flowing refractory castables) of size 10×10×10mm, obtained by computerized tomography. The white circles are cut corundum grains, the black ones air pores. b2) Result of 3D image analysis: the grains are approximated by spheres of variable radii. After Ballani, F., Daley, D.J., and Stoyan, D. (2005) Modelling the microstructure of concrete with spherical grains. *Comput. Materials Sci.* 35, 399–407. 120

Figure 6.2-3 Plot of the distribution of the Nearest Neighbor Distance $2w$ between the GaAs NW in the arrays of sample A1, A2. 121

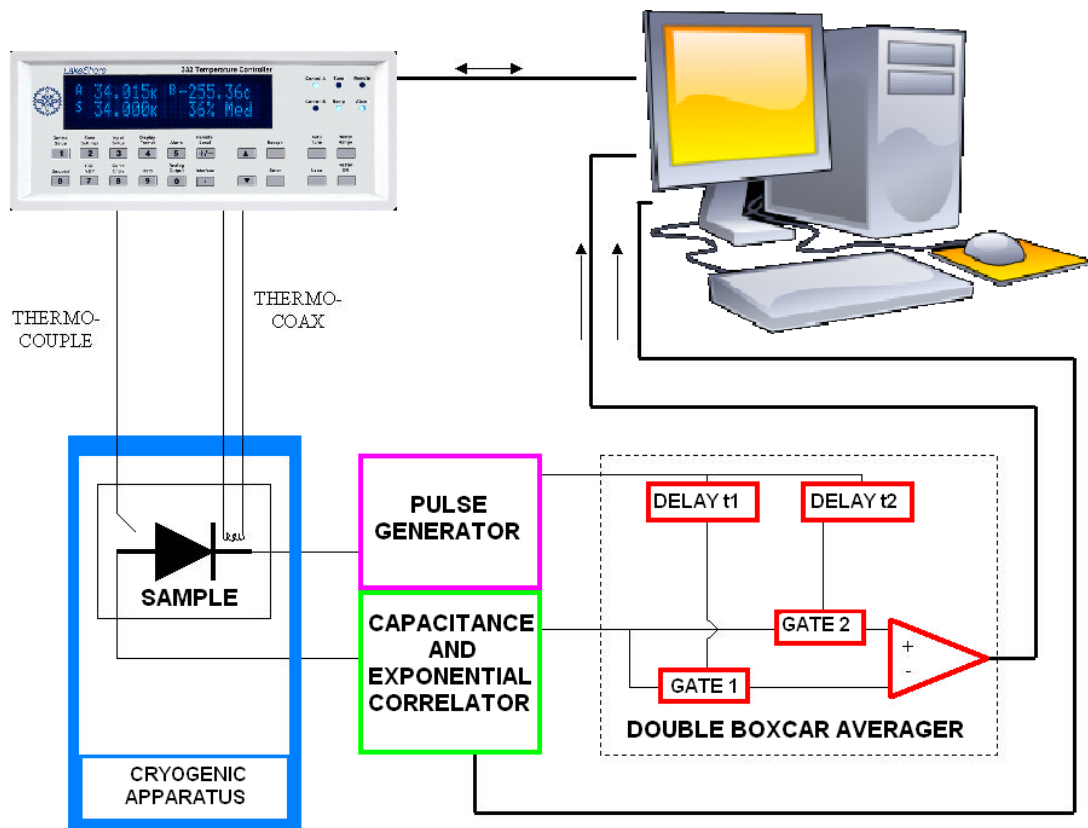
Figure 6.2-4 Face_centered cubic lattice: the nearest and next nearest neighbors of the central atom (shown as the black ball) are denoted by numbers 1 and 2, respectively; the other atoms are shown in gray. After N.V. Sibirev, M.A. Timofeeva, A.D. Bol'shakov, M.V. Nazarenko, V.G. Dubrovskii, *Physics of the Solid State*, **2010**, 52, 7. 123

Figure 6.2-5 Plots of the critical length l_{crit} versus the cross-sectional dimension $2a$ (range from 50 nm to 140 nm) and the distance $2w$ between the NWs (range from 0 to 600 nm), for a) $\gamma_s = 0.69 \text{ J/m}^2$, b) $\gamma_s = 0.86 \text{ J/m}^2$, c) $\gamma_s = 1.23 \text{ J/m}^2$, d) $\gamma_s = 1.5 \text{ J/m}^2$, e) $\gamma_s = 2.24 \text{ J/m}^2$125

Figure 6.2-6 a) Schematic of the experimental set-up used for the AFM characterization. b) –d) AFM micrographs of a NW array in cross section (semi-contact mode) obtained two months after the SEM characterization.126

Appendix A

Block Diagram of DLTS Set-Up



LIST OF PUBLICATIONS

Cavallini, S. Carapezzi, A. Castaldini, A. Irrera, Properties of Si nanowires as a Function of their Growth Conditions, *Physica B*, 10.106/j.physb.2013.11.021; <http://www.sciencedirect.com/science/article/pii/S0921452613007345>

S. Carapezzi, A. Castaldini, A. Irrera, A. Cavallini, Defect Level Characterization of Silicon Nanowire Arrays: Towards Novel Experimental Paradigms, *AIP Conference Proceedings* (accepted)

S. Carapezzi, G. Priante, R. Hinchet, L. Montes, V. Grillo, S. Rubini, A. Cavallini, Bending and Bundling of GaAs Nanowires. A Case of Adhesion Induced Self-Assembly Nanowires (submitted)